

**III-VI METAL CHALCOGENIDE  
SEMICONDUCTOR NANOSHEETS AND  
HETEROSTRUCTURES**

Garry William Mudd, MSci (Hons)

Thesis submitted to the University of Nottingham  
for the degree of Doctor of Philosophy

May 2016

## Abstract

This thesis presents an investigation into the properties of III-VI metal chalcogenide semiconductor nanosheets and demonstrates their capability to enhance graphene-based optoelectronics. Strong quantization effects and tunable near-infrared-to-visible (NIR-to-VIS) photoluminescence emission are reported in mechanically exfoliated crystals of  $\gamma$ -rhombohedral semiconducting InSe at room temperature. The optical properties of InSe nanosheets differ qualitatively from those reported for transition metal dichalcogenides and indicate a crossover from a direct-to-indirect band gap semiconductor when the InSe nanosheet thickness,  $L$ , is reduced to a few nanometres, corresponding to the emergence of a 'Mexican hat' energy dispersion for the valence band.

At low temperature, radiative recombination of photoexcited carriers bound at native donors and acceptors in nominally undoped InSe nanosheets is observed. A two-dimensional hydrogenic model for impurities is used to describe the increase in binding energy with decreasing  $L$  and reveals a strong sensitivity of the binding energy on the position of the impurities within the nanolayer.

The application of a magnetic field,  $B$ , perpendicular to the plane of InSe nanosheets induces a marked change of the observed optical spectrum. A transfer of intensity from a low-to-high energy component at high  $B$  corresponds to an indirect-to-direct band gap crossover, which arises from the Landau quantisation of the in-plane carrier motion and crossover between hole cyclotron orbits centred on closed edges of the valence band.

High broad-band (NIR-to-VIS) photoresponsivity is achieved in mechanically formed InSe-graphene van der Waals heterostructures, which exploit the broad-band transparency of graphene, the direct bandgap of InSe, and the favourable band line up of  $n$ -InSe with graphene. The photoresponse is dependent on the electron transit time through the InSe layer, as evaluated by a semiclassical model.

## Acknowledgments

Firstly, I would like to express my sincere gratitude to my supervisor, Prof. Amalia Patanè, for the continuous support and encouragement throughout the course of my PhD. I am particularly grateful for the time and patience that Amalia has invested in guiding me throughout my research, and also for enabling me to undertake new experiences, which will prove invaluable in the years to come.

Secondly, I wish to thank my co-supervisors, Prof. Peter H. Beton and Prof. Laurence Eaves for their provision of limitless counsel, expertise and direction.

I would like to give my thanks to Dr. Lyudmila Turyanska, Dr. Oleg Makarovsky and Simon A. Svatek for their valuable collaboration and assistance with research and many technical tasks, both within and outside of the laboratory. Furthermore, I would like to thank the many inhabitants and visitors of the Wendy house, Dr. Nilanthy Balakrishnan, Andrew Knott, Dr. Ateeq Nasir, Tian-hang “Ken” Ren, Dr. Anton Velychko, Dr. Fabrizio Moro, Dr. Zakhar R. Kudrynski, Dr. Natalia Alexeeva, Dr. Mazliana A. Kamarudin, Dr. Evgenii Vdovin, Dr. Oliver Larkin, Jake Greener, Davide Di Paola, Mahabub Bhuiyan, Masahiro Matsuura, James Wrigley, Craig Wyres and James Thomas for all the good times shared carrying out projects, during coffee breaks, lunches and celebrations over the years.

I would also like to acknowledge the support of our collaborators throughout the course of several research projects, Prof. Marek Potemski, Dr. Maciej Molas and Dr. Karol Nogajewski (Laboratoire National des Champs Magnétiques Intenses Grenoble); Dr. Viktor Zolyomi, Prof. Vladimir Falko, Dr. Lee Hague and Prof. Kostya S. Novoselov (University of Manchester); Alex J. Marsden and Dr. Neil R. Wilson (University of Warwick); Dr. Tillman Godde and Prof. Sasha Tartakovskii (University of Sheffield); and Prof. Zakhar D. Kovalyuk

(Institute for Problems of Materials Science at the National Academy of Sciences of Ukraine, Chernivtsi).

I would like to extend my gratitude to the staff at The University of Nottingham that have given their time to support my research, Dr. Chris Mellor, Jas Chauhan and Dave Taylor for their expertise in semiconductor device fabrication; Chris Pallender, David Holt, Bob Chettle, Pete Smith, Ian Taylor, Steve Tabreham, Paul Munday, Mike Fay, Jonathan Pearson, Sanjeev Taak, Dr. Philip Hawker and Michael Parker for their technical wizardry and Helen Smith, Wendy Brennan, Maria Hall, Melanie Stretton, Julie Kenney, Deborah Bonnar, Mark Thomas, Sue Warburton, Shaun Beebe, Prof. Richard Bowtell and Prof. Mike Merrifield for administrative and financial support.

I acknowledge the support of The University of Nottingham and the Graduate School Travel Prize, the Institute of Physics (Research Student Conference Fund Bursary and C R Barber Trust Fund Travel Prize), the Engineering and Physical Sciences Research Council (EPSRC, EP/M012700/1), the National Academy of Sciences of Ukraine, and the EU Graphene Flagship Programme.

Finally, I thank my family, close friends and fantastic teachers at Appleby Grammar School (Cumbria) and Chatsworth International School (Singapore) for enabling me to pursue higher education.

## List of publications

1. Mudd, G. W., Svatek, S. A., Ren, T., Patanè, A., Makarovskiy, O., Eaves, L., Beton, P. H., Kovalyuk, Z. D., Lashkarev, G. V., Kudrynskiy, Z. R. and Dmitriev, A. I., Tuning the band gap of exfoliated InSe nanosheets by quantum confinement. *Advanced Materials*, **25**, 5714 (2013).
2. Mudd, G. W., Patanè, A., Kudrynskiy, Z. R., Fay, M. W., Makarovskiy, O., Eaves, L., Kovalyuk, Z. D., Zólyomi, V. and Falko, V., Quantum confined acceptors and donors in InSe nanosheets. *Applied Physics Letters*, **105**, 221909 (2014).
3. Balakrishnan, N., Kudrynskiy, Z. R., Fay, M. W., Mudd, G. W., Svatek, S. A., Makarovskiy, O., Kovalyuk, Z. D., Eaves, L., Beton, P. H. and Patanè, A., Room Temperature Electroluminescence from Mechanically Formed van der Waals III–VI Homojunctions and Heterojunctions. *Advanced Optical Materials*, **2**, 1064 (2014).
4. Mudd, G. W., Svatek, S. A., Hague, L., Makarovskiy, O., Kudrynskiy, Z. R., Mellor, C. J., Beton, P. H., Eaves, L., Novoselov, K. S., Kovalyuk, Z. D., Vdovin, E. E., Marsden, A. J., Wilson, N. R. and Patanè, A., High Broad-Band Photoresponsivity of Mechanically Formed InSe–Graphene van der Waals Heterostructures. *Advanced Materials*, **27**, 3760 (2015).
5. Svatek, S. A., Mudd, G. W., Kudrynskiy, Z. R., Makarovskiy, O., Kovalyuk, Z. D., Mellor, C. J., Eaves, L., Beton, P. H., Patanè, A., Graphene-InSe-graphene van der Waals heterostructures. *Journal of Physics: Conference Series*, **647**, 012001 (2015).

## List of conference presentations

### Poster presentations

1. Mudd, G. W., Svatek, S. A., Ren, T., Patanè, A., Makarovskiy, O., Eaves, L., Beton, P. H., Kovalyuk, Z. D., Lashkarev, G. V., Kudrynskiy, Z. R. and Dmitriev, A. I., Tuning the band gap of exfoliated InSe nanosheets by quantum confinement. *Joint 20<sup>th</sup> International Conference on Electronic Properties of Two-Dimensional Systems and 16<sup>th</sup> International Conference on Modulated Semiconductor Structures*, Wroclaw, Poland, July 1-5, (2013).

### Contributed talks

1. Mudd, G. W., Svatek, S. A., Ren, T., Patanè, A., Makarovskiy, O., Eaves, L., Beton, P. H., Kovalyuk, Z. D., Lashkarev, G. V., Kudrynskiy, Z. R. and Dmitriev, A. I., Tuning the band gap of exfoliated InSe nanosheets by quantum confinement. *UK Semiconductors*, Sheffield, United Kingdom, July 9-10, (2014).
2. Mudd, G. W., Svatek, S. A., Ren, T., Patanè, A., Makarovskiy, O., Eaves, L., Beton, P. H., Kovalyuk, Z. D., Lashkarev, G. V., Kudrynskiy, Z. R. and Dmitriev, A. I., Tuning the band gap of exfoliated InSe nanosheets by quantum confinement: *Rank Prize Symposium on 2D Materials for Optoelectronics, Plasmonics and Photonics*, Cumbria, United Kingdom, September 22-25, (2014).
3. Mudd, G. W., Svatek, S. A., Hague, L., Makarovskiy, O., Kudrynskiy, Z. R., Mellor, C. J., Beton, P. H., Eaves, L., Novoselov, K. S., Kovalyuk, Z. D., Vdovin, E. E., Marsden, A. J., Wilson, N. R. and Patanè, A., Physics and applications of van der Waals InSe nanosheets and heterostructures. *UK Semiconductors*, Sheffield, United Kingdom, July 1-2, (2015).

4. Mudd, G. W., Svatek, S. A., Hague, L., Makarovskiy, O., Kudrynskiy, Z. R., Mellor, C. J., Beton, P. H., Eaves, L., Novoselov, K. S., Kovalyuk, Z. D., Vdovin, E. E., Marsden, A. J., Wilson, N. R. and Patanè, A., Physics and applications of van der Waals InSe nanosheets and heterostructures. *Joint 21<sup>st</sup> International Conference on Electronic Properties of Two-Dimensional Systems and 17<sup>th</sup> International Conference on Modulated Semiconductor Structures*, Sendai, Japan, July 26-31, (2015).

## Physical constants

Quantity	Symbol	Value	Units
Boltzmann constant	$k_B$	$1.3807 \times 10^{-23}$	$\text{JK}^{-1}$
Electron charge	$e$	$1.6022 \times 10^{-19}$	C
Electron rest mass	$m_0$	$9.1094 \times 10^{-31}$	kg
Permittivity constant	$\epsilon_0$	$8.8542 \times 10^{-12}$	$\text{Fm}^{-1}$
Planck constant	$h$	$6.6261 \times 10^{-34}$	Js
Reduced Planck constant	$\hbar$	$1.0546 \times 10^{-34}$	Js
Speed of light	$c$	$2.9979 \times 10^8$	$\text{ms}^{-1}$

# List of Contents

<b>Abstract</b>	i
<b>Acknowledgments</b>	ii
<b>List of publications</b>	iv
<b>List of conference presentations</b>	v
<b>Physical constants</b>	vii
<b>1 Introduction</b>	1
1.1 Motivation	3
1.2 Thesis overview	5
<b>2 Van der Waals semiconductors</b>	7
2.1 Tuning material properties by dimensionality	7
2.2 Properties of III-VI compounds	11
2.2.1 Rhombohedral $\gamma$ -InSe	13
2.3 Probing the electronic and vibrational properties of semiconductor nanosheets	15
2.3.1 Spatially-resolved optical spectroscopy	15
2.3.2 Electronic transport and photoresponsivity	19
2.4 Van der Waals heterostructures	27
<b>3 Experimental methods</b>	33
3.1 Exfoliation and transfer methods of vdW crystals	33
3.1.1 Mechanical exfoliation	33

3.1.2 Deterministic transfer	34
3.2 Microfabrication techniques	35
3.2.1 Planar metal-InSe junctions	36
3.2.3 Planar graphene-InSe-graphene heterostructures	38
3.2.4 Vertical graphene-InSe-graphene heterostructures	40
3.2.4.1 Method A: Exfoliated graphene	40
3.2.4.2 Method B: CVD-graphene	41
3.3 Experimental techniques: Optical characterisation	42
3.3.1 Room temperature micro-photoluminescence and Raman spectroscopy	42
3.3.2 Low temperature micro-photoluminescence spectroscopy	43
3.3.3 Magneto-photoluminescence spectroscopy	44
3.4 Experimental techniques: Atomic force microscopy	45
3.5 Experimental techniques: Transport studies	45
3.5.1 Current-Voltage (I-V) characteristics	45
3.5.2 Photocurrent Spectroscopy	47
<b>4 Tuning the band gap of InSe nanosheets by quantum confinement</b>	<b>49</b>
4.1 Introduction	49
4.2 Tunable photoluminescence emission	50
4.3 Effects of nanosheet interface roughness	53
4.4 A direct-to-indirect band gap crossover	55
4.5 Room temperature Raman spectroscopy	58

4.6 Tunable optical absorption	60
4.7 Summary	61
<b>5 Acceptor and donor states within InSe nanosheets</b>	<b>63</b>
5.1 Introduction	63
5.2 Photoluminescence at $T = 8$ K and $T = 300$ K	64
5.3 Temperature-dependent photoluminescence	66
5.4 Donor and acceptor binding energies	69
5.5 Thermal quenching of luminescence intensity	71
5.6 Summary	73
<b>6 Magneto-photoluminescence studies of exfoliated InSe</b>	<b>75</b>
6.1 Introduction	75
6.2 Valence band of InSe nanosheets	76
6.3 Magneto-photoluminescence studies on exfoliated InSe	78
6.4 Summary	86
<b>7 InSe van der Waals heterostructures and devices</b>	<b>87</b>
7.1 Introduction	87
7.2 Metal-InSe junctions	88
7.3 A planar graphene-InSe-graphene heterostructure	91
7.4 Vertical graphene-InSe-graphene heterostructures	100
7.5 Summary	106
<b>8 Conclusions and future directions</b>	<b>108</b>
8.1 Tuning the band gap of InSe nanosheets by quantum confinement	109

8.2 Acceptor and donor states within InSe nanosheets	110
8.3 Magneto-photoluminescence studies of exfoliated InSe	111
8.4 InSe van der Waals heterostructures and devices	111
8.5 Future directions	112
8.5.1 Towards state-of-the-art III-VI compound devices	112
8.5.2 Novel 2D functionality	114
8.5.3 Advanced III-VI compound van der Waals heterostructures	116
8.5.4 Phonon transport in III-VI compounds	118
8.5.5 Enabling 2D Dirac materials	119
<b>Bibliography</b>	<b>122</b>

# Chapter 1

## Introduction

The successful isolation of free-standing two-dimensional (2D) crystals and the development of van der Waals (vdW) heterostructures, have unearthed a new platform for the study of condensed matter phenomena and for the development of next-generation technologies.<sup>1–3</sup> Many layered crystals have now been characterised and each offer a distinct set of material properties; prototypical examples include insulators (hexagonal-boron nitride),<sup>4–6</sup> semi-metals (graphene),<sup>1</sup> semiconductors (MoS<sub>2</sub> and black phosphorus),<sup>7–11</sup> and the more exotic, topological insulators (Bi<sub>2</sub>Se<sub>3</sub>)<sup>12</sup> and superconductors (NbSe<sub>2</sub>).<sup>2,13,14</sup> There is a great interest in exploiting these properties with a view to the development of nanoscale functional devices. In particular, 2D vdW semiconductors have demonstrated promise in prototype optoelectronic applications as they exhibit strong light-matter interactions,<sup>15,16</sup> a high carrier mobility,<sup>17</sup> robust flexibility<sup>18,19</sup> and inherent transparency.<sup>20</sup> Furthermore, 2D materials may be combined to form unique vdW heterostructures with tailorable characteristics.<sup>15,21–29</sup> The degrees of parametrisation in vdW heterostructures is vast; for example, properties of the final structures can be customised through control over the careful selection of neighbouring layer materials, built-in strain and the adjacent crystallographic alignment, offering innovative device architectures for precise nanoelectronic and optoelectronic applications.<sup>3</sup>

This thesis presents an investigation into the properties and applications of an emerging class of 2D vdW layered semiconductors, namely, the III-VI compound metal chalcogenides (InX and GaX where X = S, Se and Te). In particular, we investigate exfoliated InSe nanosheets by spatially-resolved optical spectroscopy (micro-photoluminescence and Raman), atomic force microscopy and as

photoactive components in a series of nanoscale devices and vdW heterostructures.

Tunable radiative recombination is observed at room temperature from exfoliated InSe nanosheets, as probed by micro-photoluminescence spectroscopy ( $\mu$ PL). The emission is tuned from the near-infrared (NIR) to the visible (VIS) spectral range with decreasing nanosheet thickness, as measured by atomic force microscopy (AFM), revealing that InSe can form optically efficient quantum well nanostructures, in which charge carriers are confined in the axis perpendicular to the plane of the layers. In ultrathin exfoliated nanosheets, we observe a greater than expected decay of the photoluminescence intensity with decreasing nanosheet thickness, which we attribute to a direct-to-indirect band gap crossover as the nanosheets approach the monolayer limit. Supporting band structure calculations suggest the emergence of a 'Mexican hat'-shaped energy dispersion for the valence band (VB), which gradually shifts the valence band maximum (VBM) from a direct-to-indirect alignment with respect to the conduction band minimum (CBM).

At low temperatures ( $T = 4.2$  K), we observe radiative recombination of photoexcited carriers bound to impurity and defect states in InSe nanosheets. The binding energy of the photoexcited carriers is generally found to increase with decreasing nanosheet thickness and also exhibits a strong sensitivity to the dopant position within the nanolayer. We further probe the optical emission at low temperature and under high magnetic fields ( $B \leq 30$  T) by magneto-photoluminescence spectroscopy. Bright and sharp luminescence is observed from bulk-like exfoliated InSe layers, suggestive of spatial localization of photoexcited charge carriers and zero-dimensional quantum dot emission from carriers bound to unintentional impurity and/or defect states. In a thin InSe nanosheet ( $\sim 7$  layers), we observe the transfer of optical intensity from a low-to-high energy component

under an increasing magnetic field, suggestive of an indirect-to-direct band gap transition, controllably induced by the magnetic field.

To investigate the potential applications of InSe, we have developed and characterised a series of prototype nanoscale optoelectronic devices. In metal-InSe junctions we infer a spectrally tunable absorption of photons in InSe nanosheets, dependent upon the nanosheet thickness. From photocurrent spectroscopy measurements, we find that the photoresponsivity is limited by the band alignment at the metal-semiconductor interface. Furthermore, of importance to the enhancement of graphene-based optoelectronics, we demonstrate a favourable band alignment between InSe and single-layer graphene through realisation of several planar and vertical InSe-graphene vdW heterostructures. Two fabrication methods are compared, utilising both exfoliated and chemically grown graphene, the latter of which provides a route to large area scalability. The optoelectronic properties of the InSe-graphene heterojunctions are evaluated and suggest the formation of Ohmic contacts at the interface. Subsequently, the efficient extraction of photogenerated charge carriers, from the InSe photoactive layer to the transparent graphene electrodes, enables the realisation of one of the most photosensitive vdW photodetectors reported to date.

## **1.1 Motivation**

The observation and understanding of scientific phenomena facilitates the development of technology. New discoveries can promote revolutionary leaps by offering innovative functionalities, while in-depth research provides the incremental evolutionary steps required to integrate advancements within society. The discovery of free-standing 2D materials has provided a new framework for the investigation of elusive phenomena, strengthens the understanding of modern science and has inspired technological progress. Despite the relative youth of the field, the potential technological applications now

span across a multitude of sectors. The most obvious are in electronics, where a high performance in the ultimately thin layer limit, has promising implications in an industry which requires continuous miniaturisation. Lightweight, ultrathin and mechanically robust layers could be used to realise flexible and wearable technologies and the large surface-area-to-volume ratios could prove beneficial to novel energy storage and composite materials. Furthermore, the unique band structure phenomena discovered in 2D materials may give rise to, yet to be discovered, novel technologies. Whether implemented at the nano-, micro- or macroscale, the functionality afforded by 2D material systems is ultimately driven by quantum mechanical effects which require analysis at a fundamental level.

The objectives of my PhD are to experimentally characterise the properties of InSe nanolayers with a view to investigate their potential integration and enhancement of graphene-based optoelectronics. The project is motivated by the advent of van der Waals heterostructures, which represent a promising class of materials for the realisation of nanoscale devices, in addition to novel physical systems. Graphene-boron nitride composites can exhibit large charge carrier mobility at room temperature, with applications for high speed electronics.<sup>30,31</sup> Additionally, the hybrid-multilayer system reveals a unique band structure under an external magnetic field, as compared to the isolated individual components, demonstrating a powerful method of device customisability.<sup>3</sup> Despite such outstanding properties, the absence of a band gap in graphene has continuously been highlighted as a potential weakness for optoelectronics applications.<sup>20</sup> Single-layer transition metal dichalcogenides (TMDC), employed as a semiconducting element in vdW heterostructures, show strong light-matter interactions and demonstrate functionality in tunnelling transistors, photosensitive junctions and light emitting diodes.<sup>23,32-34</sup> Unfortunately, although the band gaps in the TMDCs lie within technologically relevant spectral

windows,<sup>35</sup> they offer limited optically efficient spectral tuning, with a direct band gap only in monolayer form. In contrast, direct-gap layered semiconductors, such as black phosphorus (bP), which has a tunable band gap covering much of the near-infrared spectrum, can be used to enhance the spectral selectivity of efficient graphene-based optoelectronics. Thus, the direct-gap metal chalcogenides of the III-VI compound group, which exhibit tunable and efficient optical transitions in the near infrared-to-visible (NIR-to-VIS) spectral range, present an important class of layered semiconductor crystal that enriches the capability and spectral selectivity of vdW heterostructure technologies.

## 1.2 Thesis overview

The thesis is structured as follows.

Chapter 2 provides a review of the literature, highlighting the key findings of investigations into nanosheet III-VI layered compounds, discussed with respect to popular vdW layered semiconductors and 2D crystals.

Chapter 3 details the sample preparation and experimental methods used in the presented investigations.

Chapter 4 presents a micro-photoluminescence and Raman study of InSe nanosheets at room temperature. Thickness-dependent optical properties are observed and are discussed alongside the supporting band structure calculations of 2D and quasi-2D InSe layers.

Chapter 5 discusses the effects of temperature on the photoluminescence emission from InSe nanosheets. The dopant-associated emission observed at low temperatures is evaluated by considering a model of quantum-confined hydrogenic acceptors and donor states.

Chapter 6 presents the findings of magneto-photoluminescence studies of exfoliated InSe at  $B \leq 30$  T. Subtle and marked changes to the optical spectrum of bulk-like and nanoscale sheets are discussed.

Chapter 7 investigates the optoelectronic properties of InSe-graphene vdW heterostructures. Two fabrication methods are compared and both demonstrate a favourable band alignment between InSe and graphene, which facilitate highly photosensitive vdW photodetectors.

Chapter 8 concludes the thesis with a summary of the key results and considers future investigations with respect to ongoing developments and recent literature.

## Chapter 2

### Van der Waals semiconductors

This chapter reviews the literature on the investigations into the physical properties of III-VI compound nanosheets and those of popular metal chalcogenide (MoS<sub>2</sub>) and elemental black phosphorus (bP) vdW semiconductors, highlighting the key characteristics suitable for the development of nanoscale functional devices.

#### 2.1 Tuning material properties by dimensionality

The interaction of electrons with the periodic potential of the two-dimensional (2D) honeycomb lattice of carbon atoms in single-layer graphene generates quasiparticles with zero effective mass. By mimicking relativistic particles, electrons in graphene are governed by the Dirac equation (Dirac fermions), in place of the Schrödinger equation, and reveal a linear electronic band dispersion, markedly different from the parabolic dispersion of three-dimensional (3D) graphite.<sup>36</sup> Accordingly, graphene exhibits distinguished electronic qualities suitable for technological exploitation, such as an ambipolar field-effect, where charge carriers can be tuned between electrons and holes, as well as ballistic transport on micrometre length scales.<sup>1,2,36-39</sup> Presently, graphene holds the record for carrier mobility ( $\mu$ ) at room temperature ( $\mu \sim 2.5 \times 10^5 \text{ cm}^2\text{V}^{-1}\text{s}^{-1}$ )<sup>31</sup> and at 4 K ( $\mu \sim 6 \times 10^6 \text{ cm}^2\text{V}^{-1}\text{s}^{-1}$ ),<sup>40</sup> in addition to several further outstanding properties, such as a high thermal conductivity ( $\kappa \sim 2 - 5.3 \text{ kW m}^{-1}\text{K}^{-1}$ )<sup>41</sup> and intrinsic strength of 130 GPa with a Young's modulus of 1 TPa.<sup>42</sup> Even as an ultimately thin material (with thickness  $L \sim 0.345 \text{ nm}$ ), the single hexagonal layer of  $sp^2$  hybridized carbon atoms can support currents of milliamperes over square-micron sized devices (a factor  $10^6$  greater than copper),<sup>43,44</sup> has an opacity of  $\pi\alpha \sim 2.3\%$ ,<sup>45</sup> and exhibits impermeability to many gases.<sup>46</sup> Such an amalgamation of remarkable

properties – in a 2D system realised by a relatively facile, yet effective, exfoliation methodology – has prompted interest in a variety of layered systems beyond graphene. Of particular interest are the vdW semiconductors, identified as 2D materials with the potential to enhance graphene-based electronics and optoelectronics.

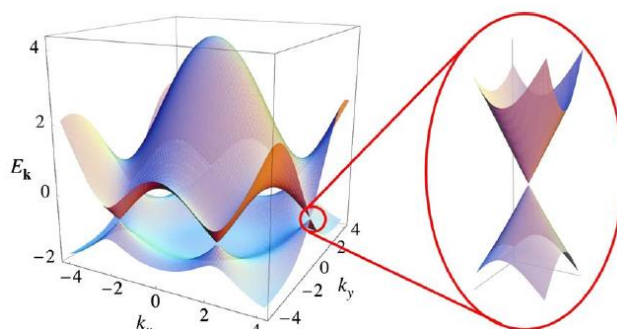


**Figure 2.1.** Energy ( $E_k$ ) – momentum ( $k_{x,y}$ ) dispersion of graphene and representation of the band structure around the Dirac point in the Brillouin zone. Figure reproduced with permission from ref. [36], © (2009), American Physical Society.

A rich variety of crystals populate the class of 2D vdW layered semiconductors. The most intensively studied materials are typically binary compounds made of metals (M) from the d block (transition metals) or p block (groups 13, 14 and 15) with the S, Se and Te chalcogens (X) of group 16, and can take various stoichiometric compositions, *i.e.*, monochalcogenides (MX), sesquichalcogenides ( $M_2X_3$ ), dichalcogenides ( $MX_2$ ) and trichalcogenides ( $MX_3$ ). The transition metal dichalcogenides of  $MoS_2$ ,  $WS_2$ ,  $MoSe_2$  and  $WSe_2$ ,<sup>10,23,47–53</sup> represent a popular class of layered vdW semiconductors which have been investigated in quasi-2D and 2D forms. Beyond the metal monochalcogenides, black phosphorus (bP) – an elemental layered material akin to graphite – can also be exfoliated to single-layer form, phosphorene, and is a semiconducting analogue of graphene.

Both  $MoS_2$  and bP offer prime examples of the changes induced in layered systems as their dimensionality is reduced toward a 2D nanosheet and exhibit properties applicable to the development of

nanoscale technologies. The calculated electronic band structures of MoS<sub>2</sub> and bP are shown in Figure 2.2 and exemplify how the properties of layered semiconductors can be tuned through the control of the crystal thickness ( $L$ ), which can induce both gradual and abrupt modifications of the band structure. In both systems, as the thickness of the crystals is reduced, an increase in the band gap energy is observed, which scales as  $1/L^2$ , consistent with the effects of the quantum confinement of electron-hole pairs along the out-of-plane axis ( $c$ -axis).<sup>54</sup>

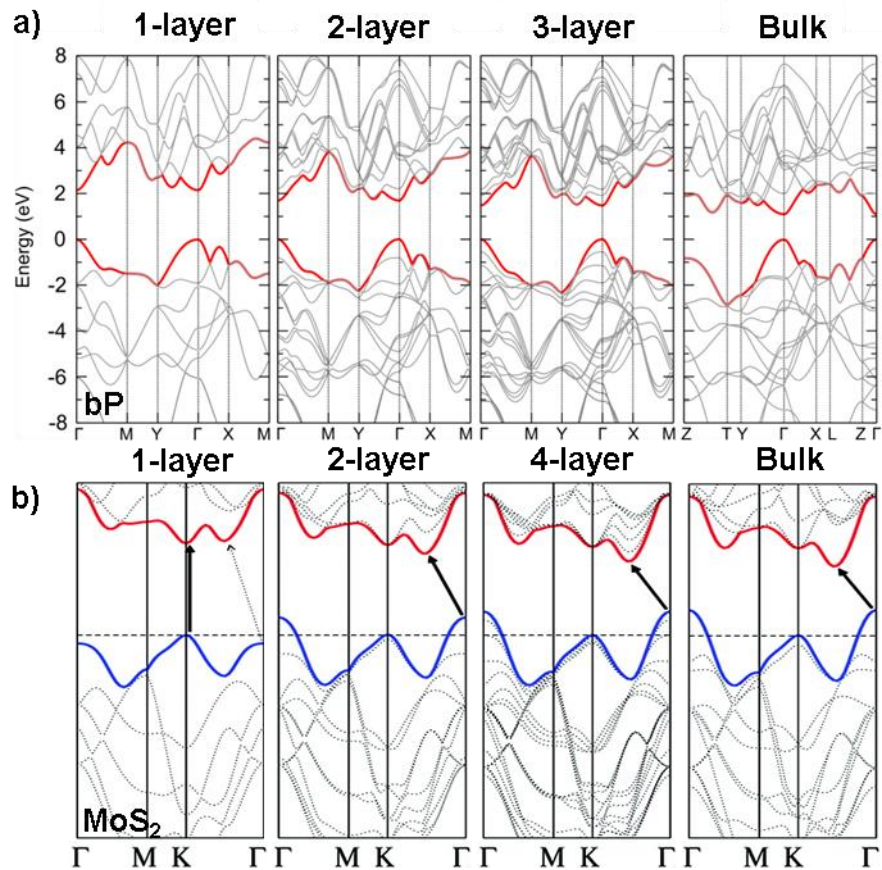


**Figure 2.2.** Calculated band structures of **a)** black phosphorus and **b)** MoS<sub>2</sub>. Figures reproduced and adapted with permission from: ref. [55], © (2015), IOP Publishing and ref. [56], © (2010), American Chemical Society.

Depending on the approach used, band structure calculations can provide a realistic description of the curvature of the energy-momentum dispersion and can predict the relative band alignments (*i.e.*, direct or indirect). However, in some cases, they can struggle to provide the

correct estimate of the energy separation between the conduction and valence bands. For example, the calculations for bP in Figure 2.2 give the energy gap for monolayer phosphorene as  $E_g \sim 2$  eV, which is corroborated with other theoretical predictions, however the bulk band gap is estimated as  $E_g \sim 1$  eV, far greater than the experimentally determined value of  $E_g \sim 0.3$  eV.<sup>55</sup> On the other hand, the relative band alignments and quantum energy shifts associated with a change to the crystal thickness can be accurately determined and are reflected in optical studies.<sup>11,55,57–60</sup> In bP, the band gap covers a considerably large spectral range, measured from  $h\nu \sim 0.3$  eV in bulk bP, to  $h\nu \sim 1.75$  eV in phosphorene and is found to be direct, offering an impressive degree of band gap energy tunability. The conduction band minimum (CBM) and valence band maximum (VBM) in bP remain aligned at the  $\Gamma$ -point in the Brillouin zone (BZ), independent of the number of layers (Figure 2.2a).<sup>55, 61</sup> This is not the case for the metal dichalcogenide MoS<sub>2</sub>, which in bulk form has an indirect band gap ( $h\nu \sim 1.29$  eV) but develops a direct-gap in monolayer form ( $h\nu \sim 1.9$  eV).<sup>62</sup> With decreasing layer number, the energy gap between the indirect transition, with the CBM mid-way between the  $\Gamma$ - and K-points and the VBM at  $\Gamma$ , becomes larger in energy relative to the direct transition located at the K-point, resulting in an abrupt shift of both the CBM and VBM to the K-point for single-layer MoS<sub>2</sub> (Figure 2.2b). Consequently, this indirect to direct-crossover results in a striking increase in photoluminescence emission at the single layer limit. The energy scale for the MoS<sub>2</sub> band structure calculations in Figure 2.2 is omitted in the original paper as,<sup>60</sup> while the direct-to-indirect transition agrees with the observed thickness-dependent luminescence behaviour, the absolute energy separations are less reliable compared to the experimentally measured values.<sup>7,62</sup> Such calculations can also provide an estimate of the carrier effective mass in few layer crystals, which prove useful in determining the electronic properties at the ultrathin limit. The curvature

of the electronic band dispersion governs the carrier effective mass ( $m_{e,h}$ ):

$$\frac{1}{m_{e,h}} = \frac{1}{\hbar^2} \left( \frac{d^2 E}{dk^2} \right), \quad (2.1)$$

which is proportional to the carrier mobility

$$\mu_{e,h} = \frac{e\tau_s}{m_{e,h}}, \quad (2.2)$$

where  $e$  is the charge of an electron and  $\tau_s$  is the carrier scattering time. Thus, a change in the curvature of the energy dispersion suggests a modification of the carrier mobility. As reported for MoS<sub>2</sub>, the effective mass is expected to decrease with a reduction in crystal thickness and therefore could facilitate a higher carrier mobility.<sup>17,63</sup> Additionally, the successive removal of MoS<sub>2</sub> layers should eventually change the electrostatic landscape of the remaining nanolayers and offers a method of tuning the dielectric properties of the crystal. In practice, for the case of MoS<sub>2</sub>, reports aiming to verify the thickness-dependent electronic properties have produced conflicting results,<sup>17</sup> most likely due to a number of extrinsic factors that affect the electronic performance of prototype field-effect transistors, such as scattering from interfacial Coulomb impurities.<sup>64</sup>

Nevertheless, control over the optical and electronic properties of low-dimensional materials by thickness-controlled band engineering, enabled by a straightforward exfoliation procedure, presents an effective method for the identification of advanced materials for the development of next-generation technologies. The following section introduces the III-VI compounds, an emerging class of layered semiconductors, which have the potential to contribute significantly to the development of van der Waals technologies, and reviews recent literature regarding investigations into their layer-dependent properties.

## 2.2 Properties of III-VI compounds

The most prominent members of the III-VI semiconducting crystals are the chalcogenide compounds of gallium and indium. They cover a rich system of stoichiometric ratios, for example indium selenides can take  $\text{InSe}$ ,  $\text{In}_2\text{Se}_3$ ,  $\text{In}_3\text{Se}_4$ ,  $\text{In}_4\text{Se}_3$  and  $\text{In}_6\text{Se}_7$  compositions,<sup>65</sup> in addition to a variety of crystal symmetries, for example,  $\beta$ ,  $\gamma$  and  $\varepsilon$  for  $\text{InSe}$  and  $\alpha$ ,  $\beta$ ,  $\gamma$ ,  $\delta$  and  $\kappa$  for  $\text{In}_2\text{Se}_3$ .<sup>65–67</sup> First studies of III-VI compounds date back to the 1930s and their anisotropic mechanical, optical and electronic characteristics were the subject of investigation later in the 20<sup>th</sup> century, with key interest being taken in their non-linear optical properties,<sup>68–74</sup> photovoltaic applications<sup>75–81</sup> and terahertz generation capabilities.<sup>82–84</sup>

Since the discovery of stable 2D crystals, research on III-VI compound nanosheets has thus far focussed mainly on the metal monochalcogenide (*i.e.*,  $\text{GaS}$ ,  $\text{GaSe}$ ,  $\text{GaTe}$  and  $\text{InSe}$ ) and sesquichalcogenide semiconducting compositions (*i.e.*,  $\text{In}_2\text{Se}_3$ ). Table 2.1 summarises the bulk band gaps of the most prevalent III-VI metal chalcogenide materials.<sup>85</sup> In contrast to the intensely studied TMDCs group, the III-VI semiconducting crystals of  $\text{InSe}$ ,  $\alpha\text{-In}_2\text{Se}_3$  and  $\text{GaTe}$  are reported to hold a direct band gap in bulk and few-layer form, a promising feature for the development of efficient optoelectronic miniaturised devices. Many reports state  $\text{GaSe}$  and  $\text{GaS}$  are indirect semiconductors;<sup>85–93</sup> however, a recent report on exfoliated  $\text{GaSe}$  on  $sp^2$  carbon reports  $\varepsilon\text{-GaSe}$  to have a direct band gap with photoluminescence centred around  $h\nu \sim 2 \text{ eV}$ .<sup>94</sup>

Nanosheet layers of III-VI compounds are produced by a range of top-down and bottom-up nanomaterial processing techniques. High-quality crystals are grown by the Bridgman method and can be mechanically exfoliated using adhesive tape or by liquid phase exfoliation, the latter of which can successfully produce large-area single-layer sheets of a variety of different layered materials.<sup>95,96</sup>

Bottom-up approaches, such as chemical vapour deposition (CVD), physical vapour deposition (PVD) or vapour phase mass transport, can also yield a range of III-VI compound nanosheets.<sup>97–101</sup> Such bottom-up approaches provide promising routes to scalability and parallel efforts to produce large area graphene<sup>102</sup> and TMDCs.<sup>98,103</sup> MBE growth of III-VI compounds has also been demonstrated.<sup>104,105</sup>

**Table 2.1.** Bulk band gaps of III-VI metal chalcogenides. Reproduced and modified with permission from ref. [85], © (2015), Royal Society of Chemistry.

	<b>Direct Band gap (eV)</b>	<b>Indirect Band gap (eV)</b>	<b>Nature of the band gap</b>	<b>Ref.</b>
<b>InSe</b>	1.26	-	Direct	[95]
<b><math>\alpha</math>-In<sub>2</sub>Se<sub>3</sub></b>	1.3	-	Direct	[96]
<b>GaSe</b>	2.13	2.11	Indirect	[90]
<b>GaS</b>	3.05	2.59	Indirect	[97]
<b>GaTe</b>	1.7	-	Direct	[98]

### 2.2.1 Rhombohedral $\gamma$ -InSe

The InSe nanosheets investigated in these works are prepared from the mechanical exfoliation of a Bridgman-grown InSe ingot, synthesised from a polycrystalline melt of In<sub>1.03</sub>Se<sub>0.97</sub>, which crystallises in a  $\gamma$ -rhombohedral single-crystal structure (shown in Figure 2.3). Investigations into the  $\beta$ - and  $\varepsilon$ - phase nanosheets have also been reported in the literature.<sup>110,111</sup> The primitive unit cell of the  $\gamma$ -phase has an out-of-plane lattice parameter of  $c = 2.4961$  nm (along the  $c$ -axis) and contains three layers, each consisting of four covalently bonded atoms in the sequence Se-In-In-Se.<sup>106</sup> In-plane atoms form a hexagonal lattice with parameters  $a = b = 0.4002$  nm. Neighbouring covalently bonded planes interact through van der Waals (vdW) forces and the layer stacking alignment defines the phase of the crystal; the  $\gamma$ -

polytype is classified with ABC stacking, where all three layers in the unit cell are offset relative to one another along the  $a$ - $b$  plane.<sup>112–114</sup>

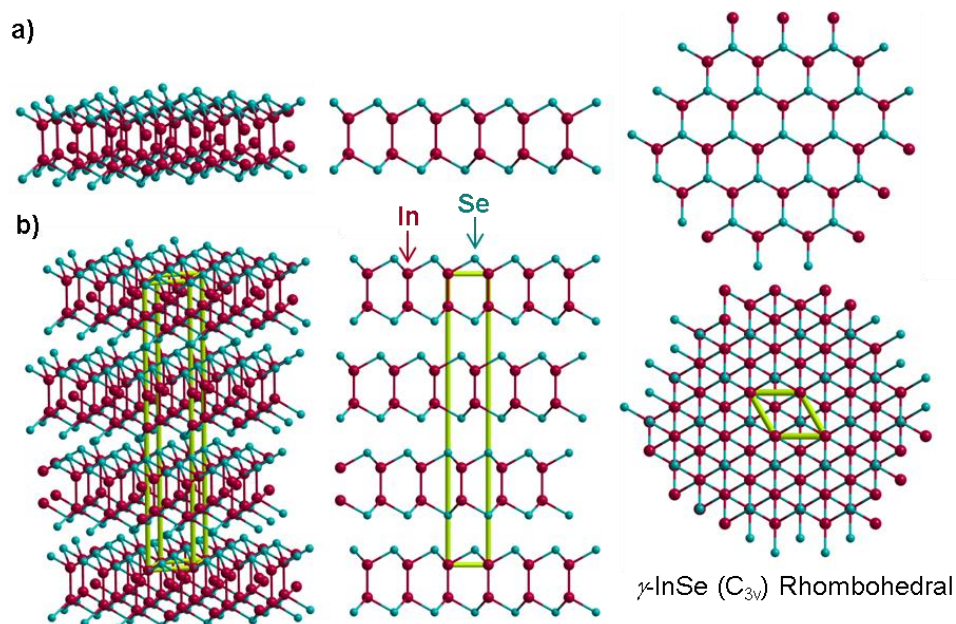


**Figure 2.3.** Crystal structure of **a)** monolayer and **b)** few-layer  $\gamma$ -InSe in three-dimensions, along the  $b$ -axis and along the  $c$ -axis, respectively. The red spheres refer to Se-atoms and the green spheres refer to In-atoms. The unit cell is highlighted in the few-layer structure and extends across three monolayers, encompassing a total of 12 atoms.

Cleaved surfaces of  $\gamma$ -InSe are easy to obtain by mechanical exfoliation methods, have a low density ( $< 10^{10} \text{ cm}^{-2}$ ) of dangling bonds<sup>115–117</sup> and have a high chemical stability under ambient conditions,<sup>118</sup> due to the non-metallic nature of the Se atoms, which form the surface of the InSe crystal and hinder oxidation.<sup>119</sup> Such properties are favourable for the formation of high quality interfaces *i.e.*, when combining with vdW crystals in the creation of artificially stacked heterostructures.<sup>3</sup> The crystal bonding anisotropy is reflected in observed anisotropies in the mechanical and electronic properties (Table 2.2).<sup>120,121</sup> Also, interruptions in the stacking sequence act as sinks for unintentional doping impurities, leading to the formation of energy barriers between the layers.<sup>120,122</sup>

**Table 2.2.** Electron ( $m_e^*$ ), hole ( $m_h^*$ ) and exciton ( $\mu$ ) effective masses and the static and dynamic dielectric permittivity values along the  $c$ -axis ( $\parallel_c$ ) and along

the in-plane axis of  $\gamma$ -InSe ( $\perp_c$ ). Reproduced with permission from ref. [121], © (2010), American Physical Society.

	$m_e^*$ ( $m_0$ )	$m_h^*$ ( $m_0$ )	$\mu$ ( $m_0$ )	$\varepsilon(\infty)$	$\varepsilon(0)$
$\parallel_c$	0.081	0.17	0.055	7.0	7.6
$\perp_c$	0.138	0.73	0.116	7.34	10.3

Bridgman growth of nominally undoped  $\gamma$ -InSe produces an  $n$ -doped material ( $n$ -InSe) due to the presence of excess interstitial In throughout the crystal.<sup>123</sup> The introduction of small amounts of Zn or Cd into the growth process can form stable hole-doped  $\gamma$ -InSe crystals ( $p$ -InSe). The electron ( $n$ ) and hole ( $p$ ) concentrations of nominally undoped and  $p$ -doped InSe are  $n = 10^{15} \text{ cm}^{-3}$  and  $p = 10^{13} \text{ cm}^{-3}$ , respectively.<sup>124</sup>

## 2.3 Probing the electronic and vibrational properties of semiconductor nanosheets

### 2.3.1 Spatially-resolved optical spectroscopy

A range of experimental techniques are employed to probe the electronic and vibrational properties of layered materials. Of particular interest for optoelectronic applications is the evaluation of the optical efficiency, structural rigidity, carrier mobility, and photoresponsivity. Spatially-resolved optical spectroscopy, such as micro-photoluminescence and Raman spectroscopy, in addition to the fabrication of prototype nanoscale field-effect transistors (FETs), represent popular methods of investigating the thickness-dependent electronic and vibrational properties of layered vdW semiconductor nanosheets.

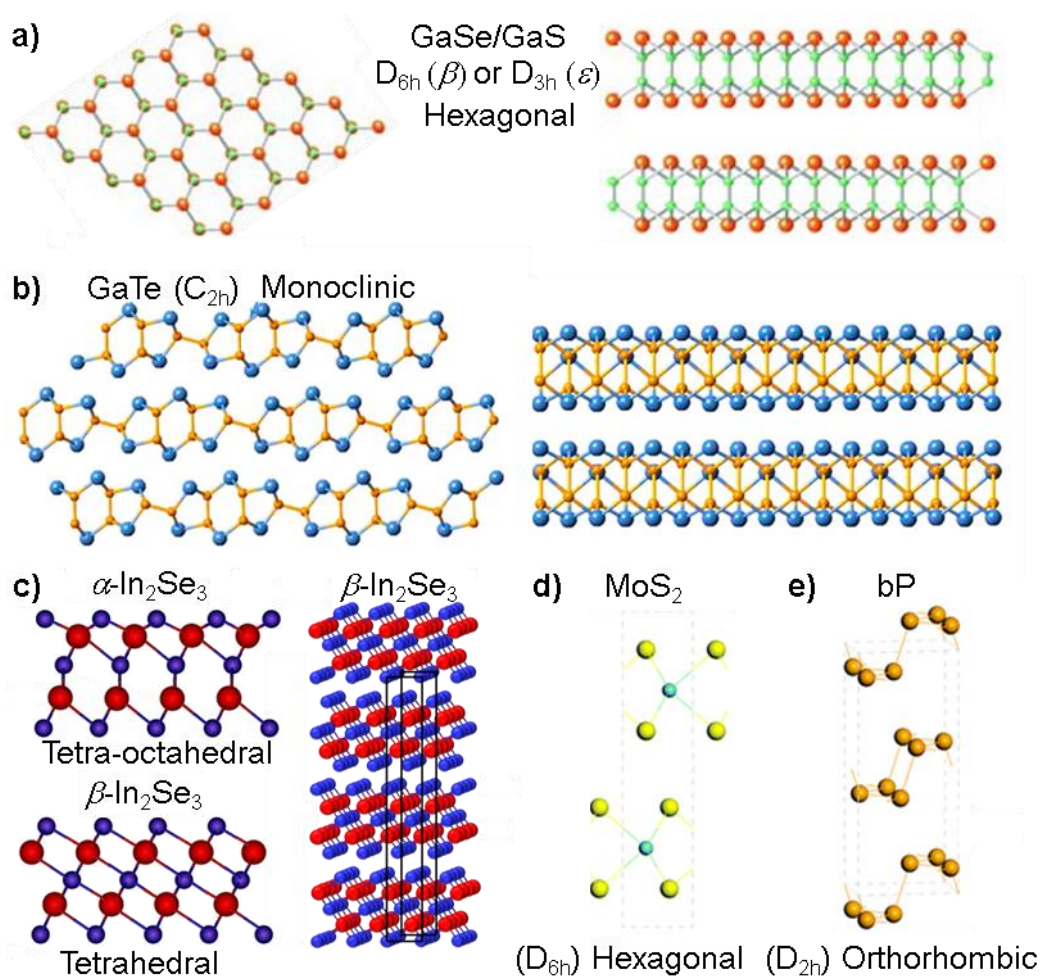


**Figure 2.4.** Crystal structures of **a)** GaSe and GaS, **b)** GaTe, **c)**  $\alpha$ - $\text{In}_2\text{Se}_3$  and  $\beta$ - $\text{In}_2\text{Se}_3$ , **d)**  $\text{MoS}_2$  and **e)** black phosphorus. Figures reproduced and adapted with permission from: (a) ref. [92], © (2012), John Wiley and Sons; (b) ref. [125], © (2014), American Chemical Society; (c) the authors of ref. [105]; (d-e) ref. [133] © (2016), Royal Society of Chemistry.

Representative crystal structures of the III-VI compounds,  $\text{MoS}_2$  and bP are shown in Figure 2.4 and demonstrate the rich variety of crystal symmetries taken by layered materials. GaSe and GaS share a similar repeating monolayer unit to InSe (X-Ga-Ga-X) and are most commonly found in the  $\beta$ - or  $\epsilon$ -phase with a hexagonal honeycomb lattice (Figure 2.4a). In contrast, GaTe has a more complicated monoclinic crystal structure; two-thirds of the Ga-Ga bonds lie perpendicular to the in-plane axis with the remaining one-third orientated parallel to the in-plane axis (Figure 2.4b).<sup>125,127</sup>  $\text{In}_2\text{Se}_3$  represents one of the many stoichiometric ratios taken by III-VI

compounds (Se-In-Se-In-Se) and has several phases, of which the  $\alpha$ - and  $\beta$ - phases are the most common and differ by the bonding symmetry within one monolayer.  $\alpha$ - $\text{In}_2\text{Se}_3$  has a mixture of tetrahedral and octahedral Se-In-Se bonds, while  $\beta$ - $\text{In}_2\text{Se}_3$  is fully tetrahedral (Figure 2.4c).<sup>128</sup> A distinctive feature of  $\text{In}_2\text{Se}_3$  is the ability to change crystalline phase with variations in temperature.<sup>129-133</sup>

Raman spectra of several III-VI compounds and  $\text{MoS}_2$  are shown in Figure 2.5a. Each material has a unique vibrational fingerprint, as determined from the inelastic scatter of photons through interaction with the oscillating polarisation, induced by illumination, in the molecular orbitals. Upon illumination, a photon may excite a vibrational state to a higher energy level, losing the equivalent energy and subsequently shifting to a lower frequency (Stokes shift, as shown in Figure 2.5). Alternatively, a photon may gain energy upon interacting with excited vibrational states, which afterwards make a transition to a lower vibrational energy level (anti-Stokes shift).

If there are  $N$  atoms within the unit cell, then there are a total of  $3N$  possible phonon modes.<sup>134</sup> For example, in  $\text{MoS}_2$ , there are 6 atoms in the unit cell and a total of 18 phonon modes (represented in Figure 2.5). Modes can be labelled by a set of Mulliken symbols ('irreducible representations') derived from group theory, which correspond to the translational and/or rotational symmetry of the vibrational mode. The Mulliken symbols 'A' and 'B' refer to modes in which the polarisation of vibration is directed along the  $c$ -axis (perpendicular to the in-plane layers), while for 'E', the polarisation is aligned along the basal plane (parallel to the in-plane layers).<sup>134</sup> Modes are further classified as infra-red active (IR), Raman active (R) or silent, according to the crystal symmetry and Raman selection rules.<sup>135,136</sup> As is suggested, the Raman active modes are observable in Raman spectroscopy and correspond to the peaks shown in the spectra (highlighted for  $\text{MoS}_2$  of  $D_{6h}$  symmetry in Figure 2.5b).

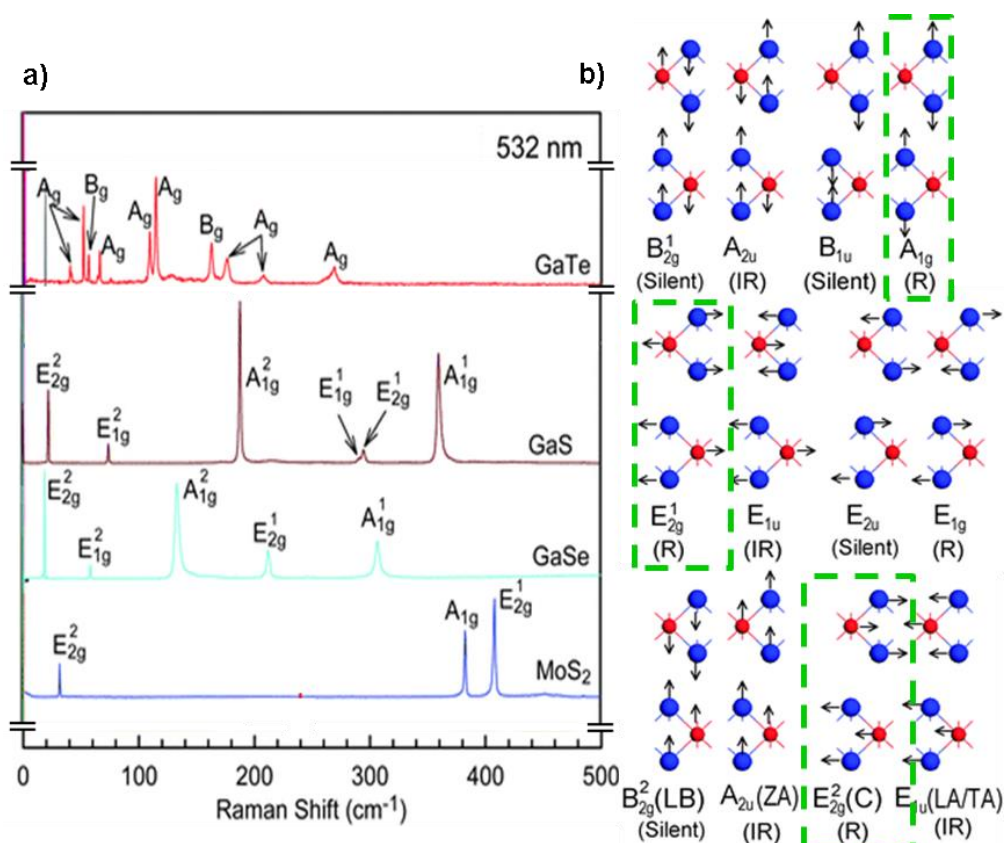


**Figure 2.5.** **a)** Raman spectra of bulk GaTe, GaS, GaSe and MoS<sub>2</sub>, probed at  $\lambda = 532$  nm. **b)** Normal vibrational modes of bulk MoS<sub>2</sub> indicating the Raman-active (R), infrared-active (IR), and both R and IR inactive (silent) modes. Figures reproduced and adapted with permission from: (a) ref. [133], © (2016), Royal Society of Chemistry and (b) ref. [137], © (2015), Royal Society of Chemistry.

GaSe and GaS also have  $D_{6h}$  symmetry in the  $\beta$ -phase, but instead have 8 atoms in the unit cell, corresponding to 24 vibrational modes.<sup>126</sup> In the observed Raman spectra, the GaSe modes are blue-shifted with respect to the GaS modes due to the larger mass of the selenium atoms.<sup>126</sup> As the Raman active modes are essentially determined from the crystal symmetry, Raman spectroscopy can be used to differentiate between the crystal phases of a given material. For example, GaSe and GaS can also be found in the  $\varepsilon$ -phase. For this phase, the unit cell has 8 atoms, but the crystal phase is now of  $D_{3h}$  symmetry, subsequently a new mode appears at  $252.1 \text{ cm}^{-1}$  that is not present in the spectra of the  $\beta$ -phase (not shown). The observable Raman modes reveal a host of information about layered materials,

such as the crystal structure, the layer stacking configuration, number of layers, the electronic structure, presence of adsorbed molecules or functional groups, structural damage and the presence of incorporated dopants – all of which can produce changes in the observed Raman frequencies or optical linewidths. Additionally, external perturbations, such as strain, temperature and electric field can modify the electronic, thermal and mechanical properties of layered materials, which can then be investigated as a function of thickness to determine applications in nanoscale electronic, opto- and thermoelectronics.<sup>137</sup>

Photoluminescence spectroscopy represents a complementary non-destructive technique and is an effective method of probing interband optical transitions in semiconductor systems. As such, the collected optical spectra are dominated by carrier recombination from the lowest energy states. These may originate from localised states, due to impurities or defects, or from band-to-band transitions, and are suitable for the investigation of thickness-induced electronic band structure changes in radiative systems. Figure 2.6 shows the photoluminescence emission from the III-VI compound GaTe and the TMDC MoS<sub>2</sub>. In contrast to MoS<sub>2</sub>, GaTe has a direct band gap in bulk form and photoexcited charge carriers are able to undergo radiative recombination, which persists in exfoliated nanosheets. As seen in Figure 2.6a, the PL blue-shifts to high energy with decreasing nanosheet thickness; this is attributed to the confinement of charge carriers along the axis perpendicular to the in-plane layers, corresponding to an increase in the energy separation between the conduction band and valence band edges.<sup>138</sup> In MoS<sub>2</sub>, the emergence of PL in monolayer sheets provides experimental evidence of the indirect-to-direct band gap crossover that is predicted to develop in the electronic band structure.<sup>56</sup>

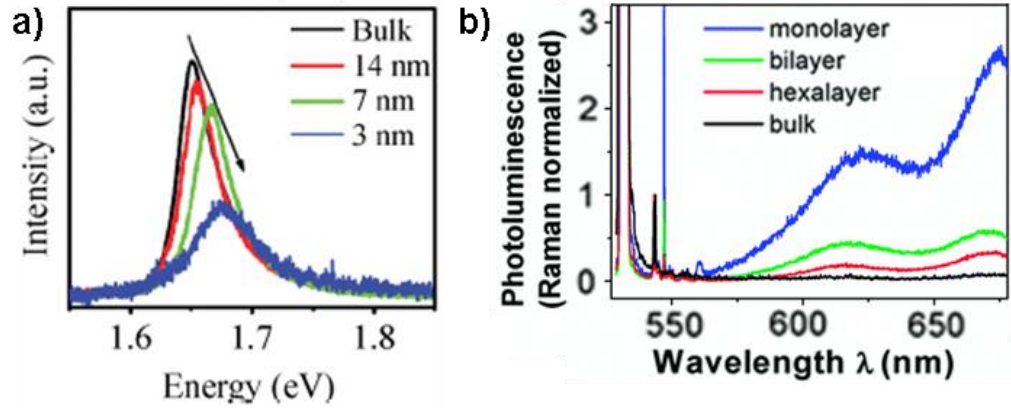


**Figure 2.6.** Photoluminescence from **a)** GaTe and **b)** MoS<sub>2</sub> as the crystal thickness is reduced. Figures reproduced and adapted with permission from: (a) ref. [138], © (2014), Tsinghua University Press and Springer-Verlag Berlin Heidelberg and (b) ref. [56], © (2012), American Chemical Society.

### 2.3.2 Electronic transport and photoresponsivity

Two figures of merit regularly used to characterise the potential of layered semiconductors for technological applications are the carrier mobility ( $\mu$ ) and the responsivity ( $R_\lambda$ ) of photosensitive field-effect transistors (FETs). Generally, the carrier mobility in III-VI compound nanosheets is determined from the field-effect differential mobility, *i.e.*,

$$\mu = g_m \left( \frac{L}{WC_i V_b} \right), \quad (2.3)$$

where  $L$  is the channel length,  $W$  is the channel width and  $V_b$  is the source-drain bias voltage. The transconductance is defined as

$$g_m = \frac{dI_s}{dV_g}, \quad (2.4)$$

where  $I_s$  is the source-drain current and  $V_g$  is the applied gate voltage. The gate capacitance between the conduction channel and gate (per unit area) is given as

$$C_i = \frac{\epsilon_0 \epsilon_r}{d}, \quad (2.5)$$

where  $\epsilon_r$  and  $d$  are the relative dielectric constant and the thickness of the insulating dielectric, respectively. Four-terminal and Hall bar geometries are less common, but provide a more realistic measure of the electronic properties by removing the contribution of the contact resistance from electrical measurements and allowing for the determination of the Hall mobility under an applied transverse magnetic field.

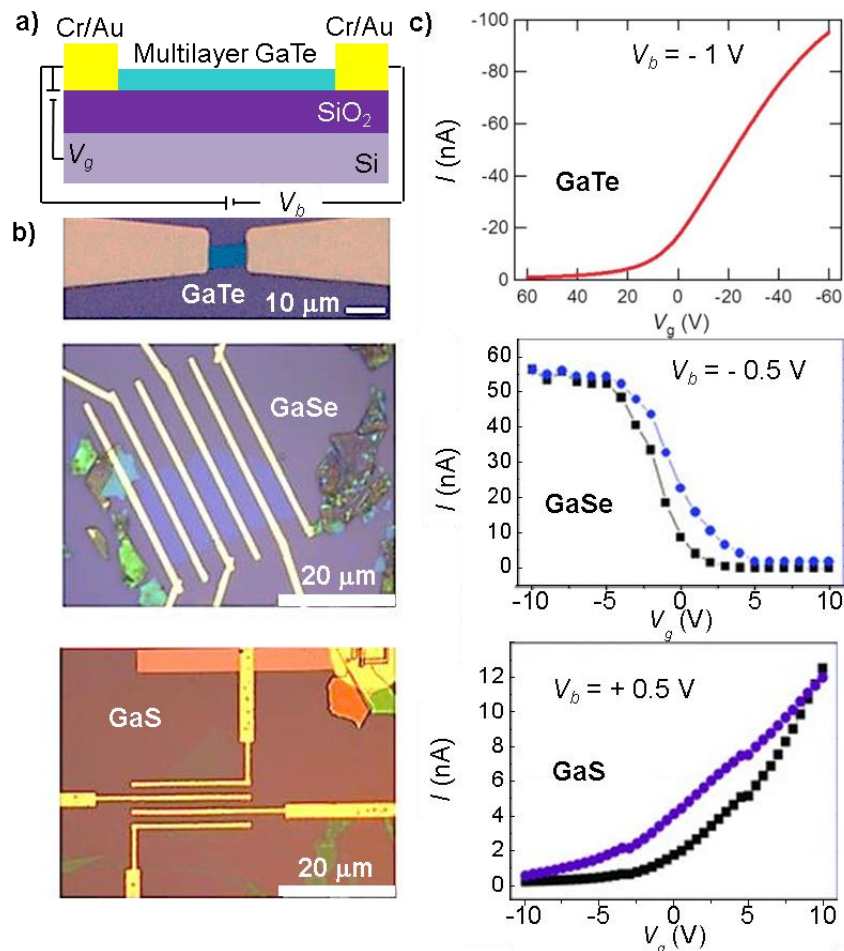


**Figure 2.7.** **a)** Schematic for a typical metal monochalcogenide field-effect transistor. **b)** Optical images of GaTe, GaSe and GaS FETs and **c)** the corresponding gate-dependence of the source-drain current (Note: the GaTe plot has reversed axes). Figures reproduced and adapted with permission from: ref. [125], © (2014), American Chemical Society and ref. [146], © (2012), John Wiley and Sons.

The first generation of vdW semiconductor FETs reported low carrier mobility values in comparison to similar graphene devices. The carrier mobility in the original *n*-type MoS<sub>2</sub> FETs was  $\mu \sim 0.5\text{-}3 \text{ cm}^2\text{V}^{-1}\text{s}^{-1}$  and

similar values were reported for III-VI compounds; InSe and GaS FETs were also reported to exhibit *n*-type behaviour, with  $\mu \sim 0.1 \text{ cm}^2\text{V}^{-1}\text{s}^{-1}$ ,<sup>108,140,141</sup> while GaSe and GaTe were shown to have *p*-type behaviour with  $\mu \sim 0.6$  and  $0.2 \text{ cm}^2\text{V}^{-1}\text{s}^{-1}$ , respectively (Figure 2.7).<sup>109,142</sup> A *p*-type field-effect mobility was reported for several few-layer bP FETs at room temperature with  $\mu \sim 35\text{-}1000 \text{ cm}^2\text{V}^{-1}\text{s}^{-1}$ ;<sup>11,55,143–146</sup> additionally, an electron mobility ( $\mu \sim 0.5 \text{ cm}^2\text{V}^{-1}\text{s}^{-1}$ ) was demonstrated, showing bP to have an ambipolar nature.<sup>145</sup>

Generally, the electronic transport in vdW semiconductors is more susceptible to the local environment and the low mobility values are attributed to charge carrier scattering mechanisms including phonon scattering, Coulomb scattering at charged interfaces, surface interface phonon scattering and roughness scattering.<sup>17,85,147</sup> Methods of enhancing the mobility ('mobility engineering') require further processing stages and include, optimising or annealing metallic contacts, employing top- or ionic-gating and layer encapsulation. Top-gated FETs demonstrate the sensitivity of vdW semiconductors to their external surroundings; Al<sub>2</sub>O<sub>3</sub> top-gates on bP FETs yield *n*-type behaviour, while HfO<sub>2</sub> gated bP devices are *p*-type.<sup>148</sup> Similar methods were applied to TMDC layer materials with charge carrier mobility generally approaching  $\mu \sim 100 \text{ cm}^2\text{V}^{-1}\text{s}^{-1}$ .<sup>17</sup>

InSe nanosheets are expected to be able to reach a higher carrier mobility than MoS<sub>2</sub> due to a lighter electron effective mass ( $m_e = 0.138m_0$  and  $0.45m_0$  for InSe and MoS<sub>2</sub>, respectively)<sup>149</sup> and a variety of approaches have demonstrated improvements to the carrier mobility values reported in the earliest InSe FETs. By using indium as the contact metal to an InSe nanosheet with thickness  $L \sim 33 \text{ nm}$ , an electron mobility of  $\mu \sim 160 \text{ cm}^2\text{V}^{-1}\text{s}^{-1}$  was obtained and outperformed Al, Ti and Cr contacts.<sup>150</sup> Similar carrier mobilities were seen in HfO<sub>2</sub> top-gated monolayer MoS<sub>2</sub> transistors ( $\mu \sim 200 \text{ cm}^2\text{V}^{-1}\text{s}^{-1}$ ) and MoS<sub>2</sub>

devices with  $L \sim 50$  nm on poly(methyl methacrylate) (PMMA) substrates ( $\mu \sim 500 \text{ cm}^2\text{V}^{-1}\text{s}^{-1}$ ).<sup>9,151</sup> Using both a  $\text{HfO}_2$  top-gate and PMMA surface together, gave a carrier mobility in  $\text{MoS}_2$  of  $\mu \sim 1090 \text{ cm}^2\text{V}^{-1}\text{s}^{-1}$ ; however, errors in the capacitive coupling introduce uncertainty in the quoted values. The authors of ref. [17] highlighted a few of the potential pitfalls in calculating the mobility and suggested methods of improving the estimations. The highest carrier mobility reported for InSe, also comparable to ultrathin strained-Si<sup>152</sup> and few-layer black phosphorus transistors,<sup>143</sup> are reported in back-gated multilayer InSe on a PMMA/ $\text{Al}_2\text{O}_3$  dielectric bilayer ( $\mu > 1000 \text{ cm}^2\text{V}^{-1}\text{s}^{-1}$ ). Investigation of multiple devices showed a thickness-dependence of the carrier mobility, with the optimum thickness in a device of  $L \sim 30$  nm; this device also has a current on/off ratio  $I_{\text{on}}/I_{\text{off}} \sim 10^8$ , demonstrating applicability with complementary metal-oxide semiconductor (CMOS) technology.<sup>149,153</sup>

Four terminal and temperature dependent studies corroborated the high mobility values in InSe, finding field-effect and Hall mobility values in the range of  $\mu \sim 50 - 2000 \text{ cm}^2\text{V}^{-1}\text{s}^{-1}$  across  $T = 20 - 300$  K, with a maximum room temperature field-effect mobility of  $\mu \sim 1250 \text{ cm}^2\text{V}^{-1}\text{s}^{-1}$ .<sup>154</sup> Given current trends in 2D semiconductor device processing, it is expected that developing top-gated InSe transistors will lead to further improvements in electronic performance. Efforts to establish the thickness-dependence of the dielectric and electronic properties in III-VI compounds were also reported (Figure 2.9). A non-destructive microwave impedance technique was used to determine the permittivity in  $\text{In}_2\text{Se}_3$  nanosheets (Figure 2.9 a-b)<sup>155</sup> and the dielectric properties of GaS and GaSe were calculated to exhibit a thickness-dependence.<sup>156</sup>

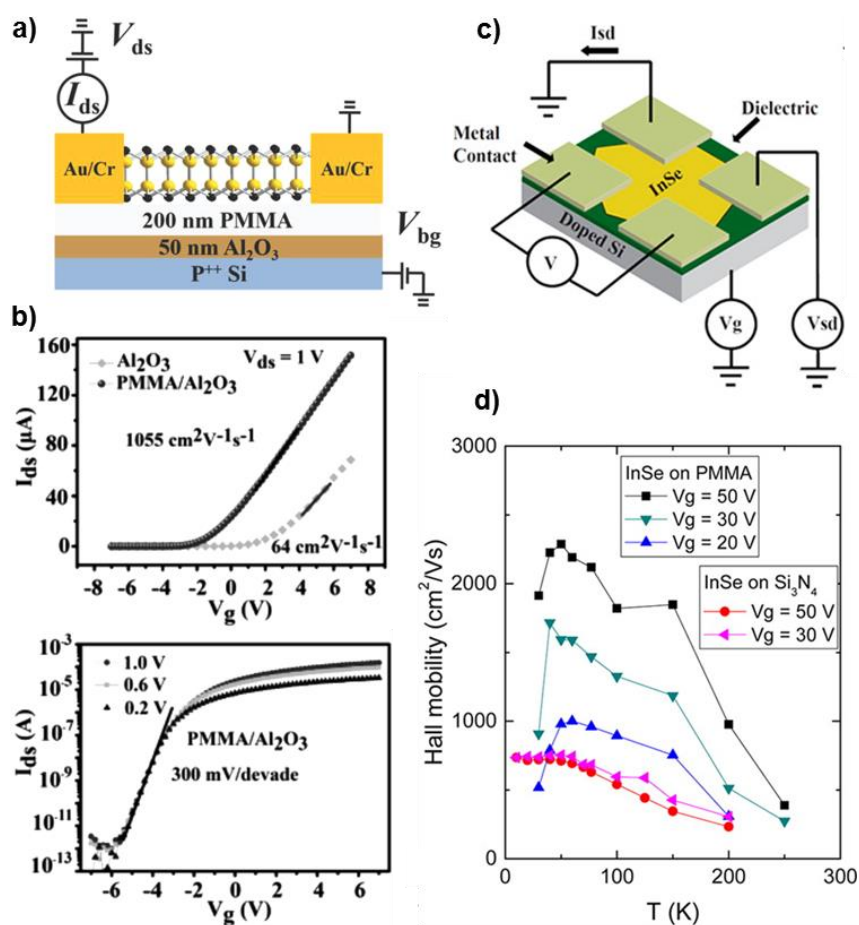


**Figure 2.8.** **a)** Schematic for a high mobility InSe nanosheet FET separated from a Si back-gate by a dielectric bilayer of Al<sub>2</sub>O<sub>3</sub> and PMMA. **b)** Gate-dependent source-drain current for InSe FETs with Al<sub>2</sub>O<sub>3</sub>/PMMA dielectric bilayer. **c)** Schematic for a four-terminal InSe FETs with Si back gate on a PMMA or Si<sub>3</sub>N<sub>4</sub> dielectric surface. **d)** Temperature-dependent Hall mobility of InSe FETs on PMMA or Si<sub>3</sub>N<sub>4</sub> surface dielectric surface. Figures reproduced and adapted with permission from: (a-b) ref. [149], © (2014), John Wiley and Sons and (c-d) ref. [154], © (2015), American Chemical Society.

Furthermore, a range of multilayer InSe FETs on PMMA/SiO<sub>2</sub> and SiO<sub>2</sub> dielectric substrates showed a maximum in the measured mobility from layers with  $L \sim 33$  nm (Figure 2.9c). While these results indeed suggest the dielectric and electronic properties are modified by changes of the nanosheet thickness, further experimental work will be required to address inconsistencies, as observed for measurements of similar dielectric-dependencies in the TMDCs (Figure 2.9d).<sup>17</sup>

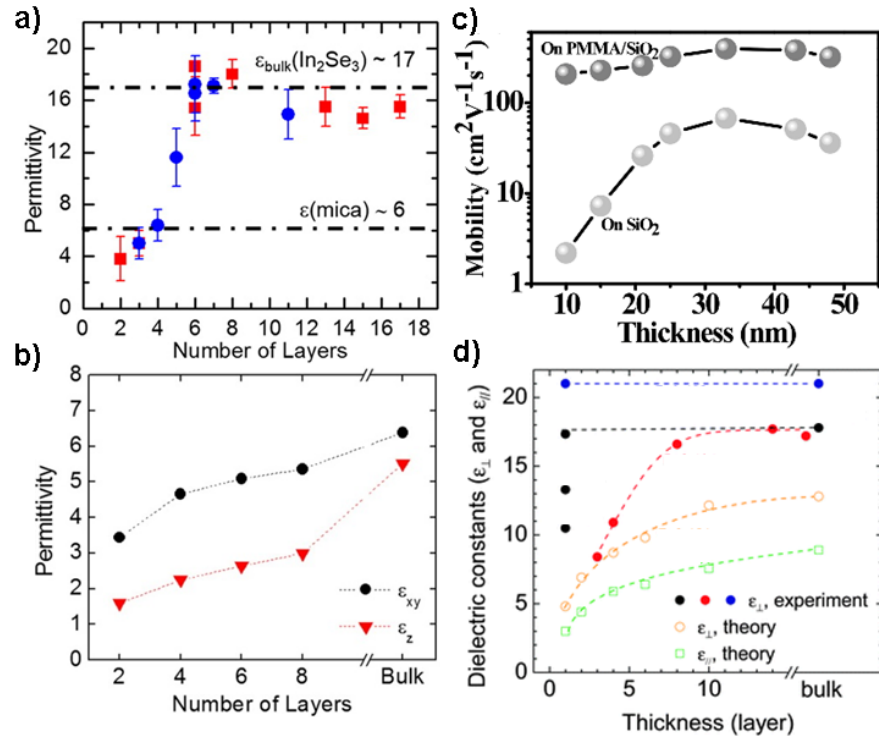


**Figure 2.9.** **a)** Permittivity as deduced from microwave impedance microscope measurements (MIM-Im) for  $\text{In}_2\text{Se}_3$ . **b)** DFT–HSE06 calculations of the ‘ion-clamped’ dielectric permittivity parallel ( $z$ ) and perpendicular ( $xy$ ) to the  $c$ -axis for  $\text{In}_2\text{Se}_3$ . **c)** Thickness-dependent carrier mobility of few-layer InSe FETs on  $\text{SiO}_2$  or PMMA/ $\text{SiO}_2$  substrates. **d)** Inconsistencies in determining thickness-dependent dielectric properties of ultrathin  $\text{MoS}_2$  FETs. Figures reproduced and adapted with permission from: (a-b) ref. [155], © (2015), American Chemical Society; (c) ref. [149], © (2014), John Wiley and Sons and (d) ref. [17], © (2015), Royal Society of Chemistry.

In addition to promising electronic properties, InSe provides a qualitatively different optical system to other vdW layered semiconductors such as TMDCs due to the presence of a direct band gap in the bulk and for few-layer nanosheets.<sup>157</sup> Efficient optical transitions, coupled with encouraging electronic properties, make InSe an appealing candidate for future optoelectronic technologies. In particular, several novel approaches were reported to improve the photoresponsivity

$$R_\lambda = \frac{\Delta I}{P}, \quad (2.6)$$

of InSe photodetectors, where  $\Delta I$  is the induced photocurrent and  $P$  is the power absorbed. In the earliest works, a photoresponsivity of

$R_\lambda \sim 34.7 \text{ mAW}^{-1}$  was reported.<sup>67</sup> The authors of ref. [140] configure the contact geometry of InSe FETs to allow for higher stable bias voltages which resulted in  $R_\lambda \sim 7 \text{ AW}^{-1}$  at  $V_b = 10 \text{ V}$  and also demonstrated the robustness of InSe as a photodetector by using flexible substrates. In the flexed state the InSe light-sensitive transistor has  $R_\lambda \sim 1.7 \text{ AW}^{-1}$ , comparable to the planar state with  $R_\lambda \sim 3.9 \text{ AW}^{-1}$  (Figure 2.10). Flexible GaSe, GaS and GaTe photodetectors were also demonstrated.<sup>93,108,99</sup> One of the more novel approaches, takes advantage of a high Schottky barrier between Al and InSe to operate the device as an avalanche photodetector ( $R_\lambda \sim 1.5 \text{ AW}^{-1}$  at  $V_b = 50 \text{ V}$ ) and also explores the effects of plasmonic enhancements by patterning Al nanostructures onto the InSe surface ( $R_\lambda \sim 37 \text{ AW}^{-1}$  at  $V_b = 30 \text{ V}$ , Figure 2.11).<sup>158</sup>

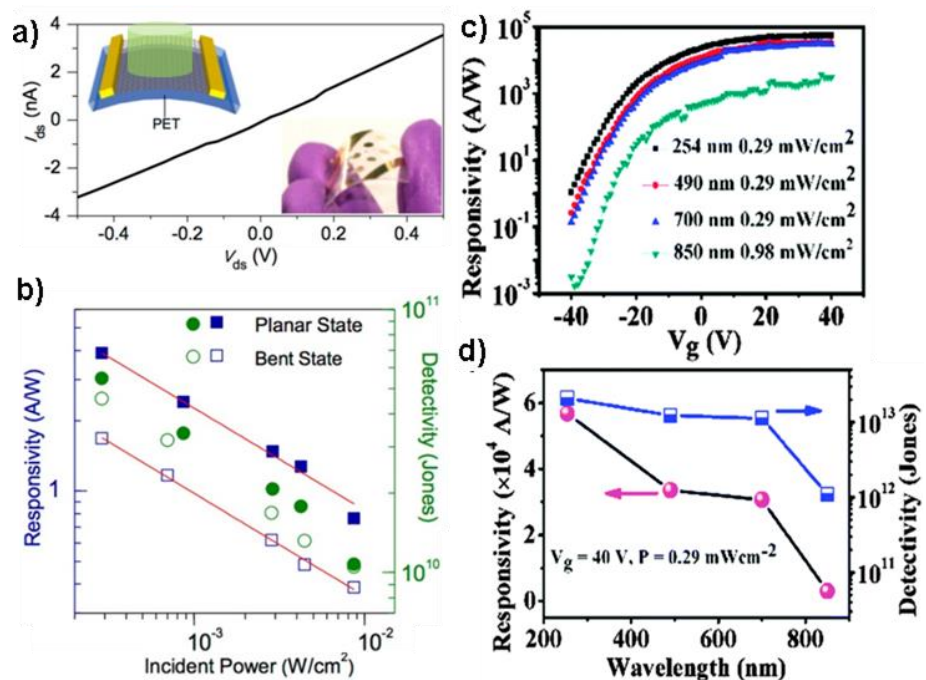


**Figure 2.10.** **a)** Source-drain current versus applied bias of a InSe phototransistor on a flexible PET substrate under dark conditions and **b)** responsivity versus incident power. **c)** Gate-dependent responsivity under a bias of  $V_s = 2 \text{ V}$  and  $P = 0.29 \text{ mWcm}^{-1}$  at  $\lambda = 254, 490, 700$  and  $850 \text{ nm}$ . **d)** Corresponding spectral responsivity and detectivity at  $V_g = 40 \text{ V}$ . Figures reproduced and adapted with permission from: (a-c) ref. [140], © (2014), American Chemical Society and (d-e) ref. [159] © (2015), Royal Society of Chemistry.

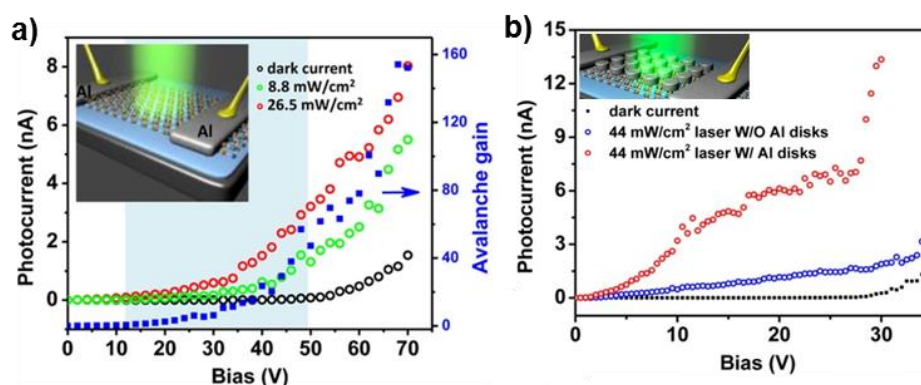


**Figure 2.11.** **a)** Photocurrent response of an InSe avalanche photodetector with Al contacts under different illumination intensities. The avalanche gain highlighted by the blue region. **b)** Photocurrent response of an InSe avalanche photodetector with and without a plasmonic Al nanodisk array, showing a substantial photocurrent enhancement. Figures reproduced and adapted with permission from ref. [158], © (2015) American Chemical Society.

Furthermore, applying a high transverse electric field through back-gating, ( $R_{\lambda} \sim 157 \text{ AW}^{-1}$  at  $V_b = 10 \text{ V}$  and  $V_g = 70 \text{ V}$ ),<sup>141</sup> combined with optimising the crystal thickness, facilitate multiple order of magnitude enhancements in the responsivity of InSe FETs ( $R_{\lambda} \sim 56800 \text{ AW}^{-1}$  at  $V_b = 5 \text{ V}$  and  $V_g = 40 \text{ V}$ ).<sup>159</sup>

As FETs approach the atomically thin-layer limit, information regarding the performance of different material systems is of paramount importance.<sup>17</sup> 2D vdW semiconductors with a low carrier effective mass and a large dielectric constant could be developed for nanoscale electronic devices with high carrier mobility and high operation frequencies. Ultrathin semiconducting materials demonstrating ambipolar nature should be compatible with complimentary logic, enabling low-power dissipation and integration with current technologies.<sup>11</sup> Furthermore, layered semiconductors have the potential to be developed as photodetectors which can be tuned within specific spectral windows in the ultraviolet (UV), visible (VIS), infrared (IR) and terahertz ranges of the electromagnetic spectrum.<sup>35,85</sup> In contrast to opaque silicon-based photodetectors, the atomic thickness of vdW layered semiconductors renders them nearly transparent and, together with their remarkable elastic properties,

enables a route to the realisation of novel applications, such as wearable technology<sup>85</sup> or integrated flexible photovoltaic structures.<sup>160,161</sup> Furthermore, being able to combine diverse 2D material properties in a single platform in vdW heterostructures represents one of the more novel approaches to the realisation of new technologies.

## 2.4 Van der Waals heterostructures

A significant milestone in the 2D material field was reached after an innovative approach to engineer the carrier mobility in graphene succeeded in creating one of the first prototype van der Waals heterostructures.<sup>3,162</sup> Concerns over the influence of enhanced scattering effects in graphene on SiO<sub>2</sub> surfaces, for example from trapped Coulomb impurities, surface states, surface roughness, phonon interactions<sup>162,163</sup> and microscopic ripples,<sup>164</sup> motivated interest in identifying alternative substrates to enhance the carrier mobility in graphene.<sup>165</sup> Dean *et al.* exploited the atomically flat surface of hBN vdW crystals, expected to be free of charge traps and dangling bonds, as a high quality substrate for graphene FETs and reported almost an order of magnitude improvement in the graphene carrier mobility compared to SiO<sub>2</sub> substrate devices.<sup>30</sup> Building on this idea, Mayorov *et al.* encapsulated graphene between hBN, thus enabling a record room temperature mobility for graphene of  $\mu \sim 2.5 \times 10^5 \text{ cm}^2\text{V}^{-1}\text{s}^{-1}$ . In addition to improving electronic performance, the early graphene-hBN heterostructures also enabled the study of physical phenomena, for example, the fractional quantum Hall effect<sup>166</sup> and electron-electron interactions (Coulomb drag) between two electronically isolated graphene sheets separated by an ultrathin ( $L \sim 1 \text{ nm}$ ) hBN barrier layer.<sup>167</sup>

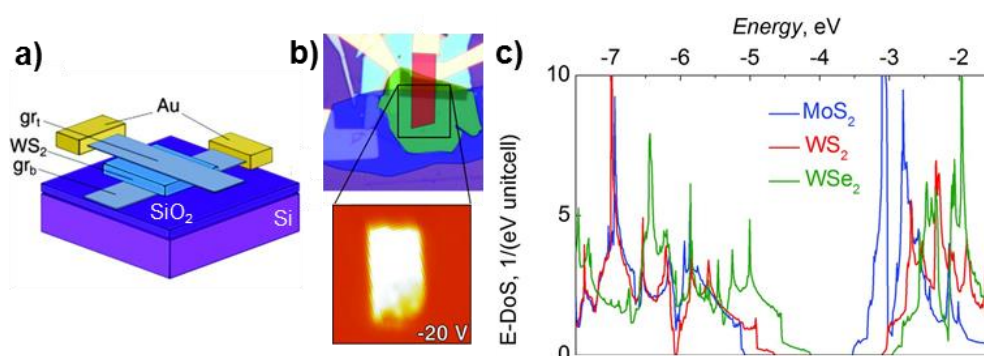


**Figure 2.12.** **a)** Schematic of a vertical graphene-WS<sub>2</sub>-graphene van der Waals heterostructure. **b)** Optical image and photocurrent map (no applied bias and  $V_g = 20$  V) showing a spatial photoresponse at the graphene-WS<sub>2</sub>-graphene overlap. **c)** DOS calculations for monolayer TMDCs. Figures reproduced and adapted with permission from ref. [15], © (2013), The American Association for the Advancement of Science.

Similar structures demonstrated the first graphene-based vertical field-effect transistors, where nanoscale hBN, MoS<sub>2</sub>, WS<sub>2</sub> exfoliated sheets were employed as tunnel barriers between graphene electrodes, showing potential applications in high frequency electronics,<sup>168</sup> transparent and flexible technology<sup>169</sup> and optoelectronics;<sup>15</sup> in particular, graphene-WS<sub>2</sub> heterostructures were shown to exhibit strong light-matter interactions, even for atomically thin semiconducting sheets, due to the presence of Van Hove singularities in the calculated electronic density of states (DOS).<sup>15</sup>

In terms of crystal stability under ambient conditions, the III-VI compounds of GaSe and InSe appear to sit between the TMDCs and black phosphorus, but vary depending on the particular chemical species; for example, exfoliated GaSe nanosheets are observed to readily oxidise in air, detrimentally affecting their optical properties,<sup>170,171</sup> while InSe nanosheets are vastly more stable, with persistently strong radiative recombination observed over considerably long time scales (Figure 2.13).<sup>171</sup> In van der Waals heterostructures, the photoactive crystals are likely to be encapsulated by protective, yet functional, adjacent layers and thus represent an ideal system for the exploitation of the full library of layered semiconductors, regardless of their stability under ambient conditions.

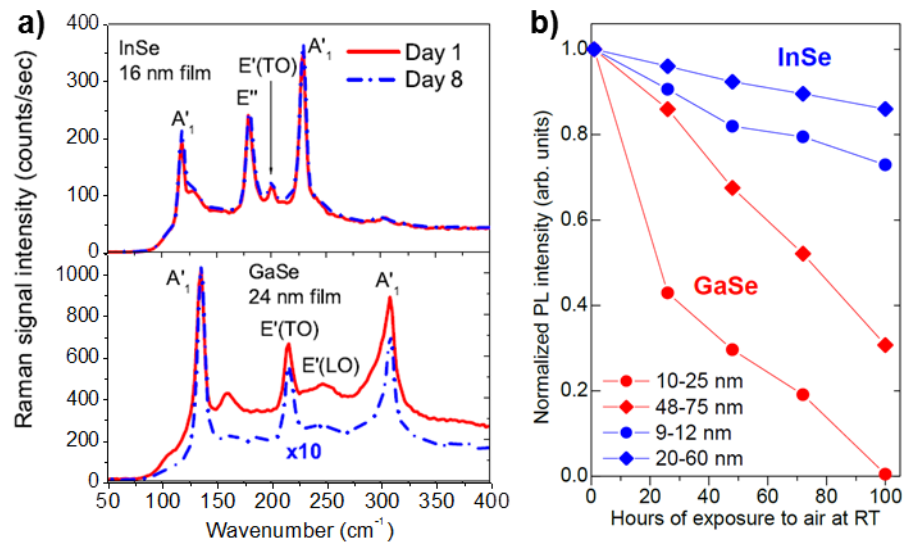


**Figure 2.13. a)** Room temperature Raman spectra for a 16 nm InSe (top) and a 24 nm GaSe (bottom) films measured immediately after exfoliation and after a period of one week. **b)** Normalised PL intensity measured as a function of time at  $T = 10$  K for GaSe and InSe thin films. Figures reproduced and adapted from ref. [171]

A range of 2D layered semiconductor heterostructures have been investigated for applications in optoelectronics, such as in photodiodes and photovoltaics.<sup>172</sup> Atomically thin  $p$ - $n$  junctions, made of WSe<sub>2</sub> ( $p$ -type) and MoS<sub>2</sub> ( $n$ -type) monolayers show gate-tunable, diode-like and photovoltaic behaviour, forming an atomically sharp heterointerface with a type-II band alignment. Charge extraction is further enhanced through the use of graphene electrodes contacted to the WSe<sub>2</sub> and MoS<sub>2</sub> monolayers.<sup>172,173</sup> A similar effect is seen in GaSe photodetectors with graphene electrodes, which also report an enhanced response time.<sup>174</sup> The low density of surface dangling bonds and ability to form a vdW interface with a range of materials also enables the coupling of 2D vdW semiconductors with bulk conventional semiconductors such as Si, avoiding the detrimental effects of lattice mismatch associated with heterointerfaces between conventional semiconductors. Recently, GaSe and GaTe layers were grown by MBE on  $n$ -Si wafers forming photodetectors with responsivity  $R_\lambda < 0.1 \text{ AW}^{-1}$ ,<sup>105,175</sup> and demonstrate the integration of III-VI

compounds with state-of-the-art Si-based technology (Figure 2.14).<sup>176</sup>

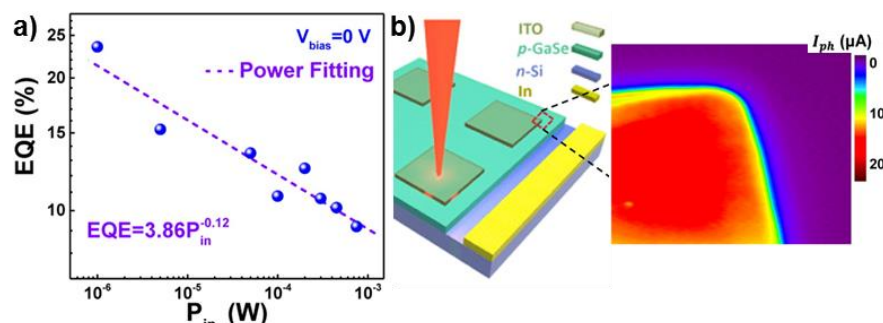


**Figure 2.14.** a) External quantum efficiency (EQE) dependence upon incident illuminating power at zero-bias voltage for GaSe-Si heterostructure. b) Schematic of GaSe-Si heterostructure and spatially resolved photocurrent map at zero-bias at the corner of the layered structure. Figures reproduced and adapted with permission from ref. [109], © 2015, American Chemical Society.

Mechanically-formed vdW heterostructure light emitting diodes can also be fabricated from layered semiconductors, including the III-VI compounds. Balakrishnan *et al.* reported on the optical and electrical properties of homojunction and heterojunctions formed from the stacking of *n*-InSe, *p*-InSe and *p*-GaSe, which exhibit room temperature electroluminescence (Figure 2.15).<sup>124</sup> A range of TMDC based electroluminescent devices have also been demonstrated, such as single-layer MoS<sub>2</sub> FETs, which are driven by hot carrier processes<sup>177</sup> and in TMDC *p-n* heterojunctions driven by electrostatic gating.<sup>23,178,179</sup> Some of the most complex vdW heterostructures that have been fabricated also succeeded in obtaining electroluminescent emission from single and multiple TMDC quantum wells (QWs).<sup>34</sup> In these light-emitting diode (LED) heterostructures, layers of hBN and graphene encapsulate single (WS<sub>2</sub>) or multiple (MoS<sub>2</sub>) QWs and required the manual stacking of at least 7 and 13 layers, respectively (Figure 2.15). The LEDs employ the ambipolar nature of the graphene electrodes to inject electrons and holes into the QWs neighbored by hBN; this configuration increases the lifetime of the quasiparticles within the semiconductor layer and enables the emission of photons.<sup>34</sup>

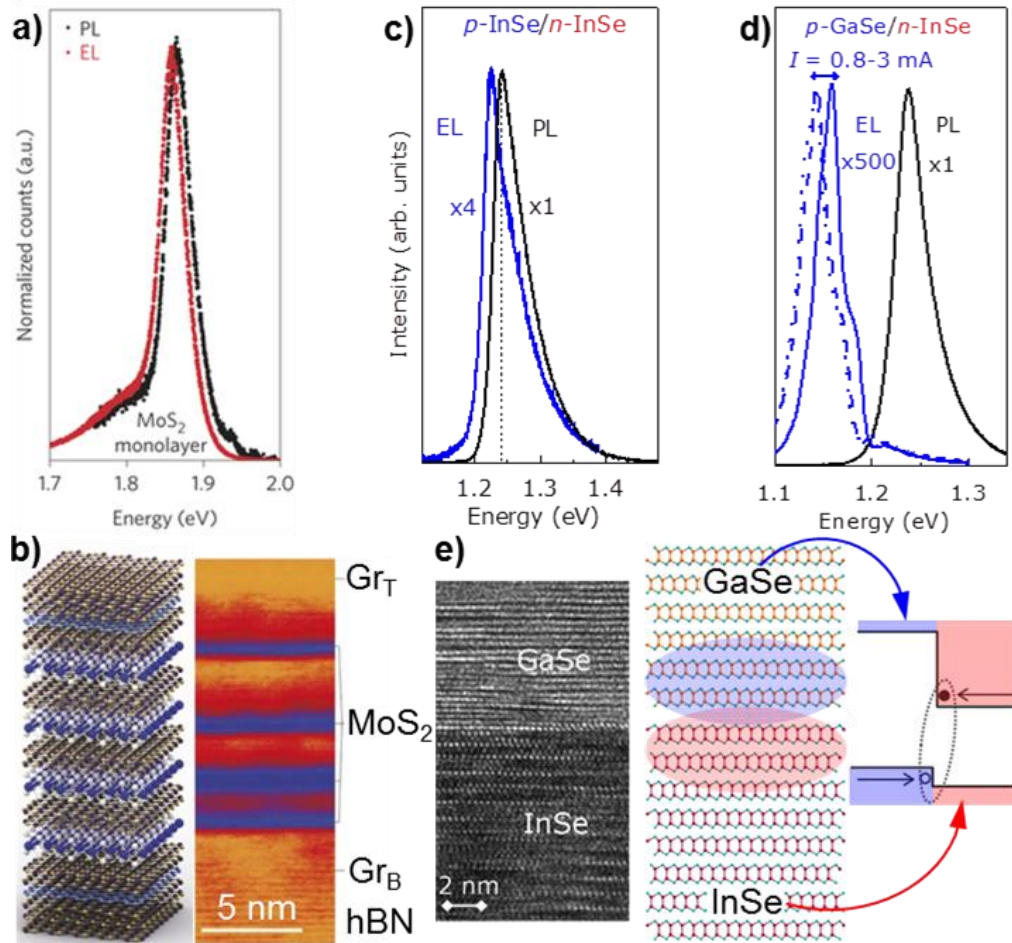


**Figure 2.15.** **a)** Comparison of the PL and EL spectra for an MoS<sub>2</sub> single quantum well. **b)** Schematic and STEM image of a hBN/graphene/MoS<sub>2</sub> multiple quantum well heterostructure. **c)** Comparison of PL and EL for a bulk *p*-*n* InSe homojunction and **d)** a bulk InSe/GaSe heterojunction. **e)** HRTEM image and schematic of the InSe/GaSe interface forming a type-II band alignment. Figures reproduced and adapted with permission from: (a-b) ref. [34], © 2015, Nature Publishing Group and (c-e) ref. [124], © 2014, John Wiley and Sons.

# Chapter 3

## Experimental methods

This chapter details the sample preparation and experimental techniques used to investigate nanosheets, devices and heterostructures fabricated from III-VI semiconductors and graphene. Source materials of the III-VI compound semiconductors were grown at the Institute for Problems of Materials Science at the National Academy of Sciences of Ukraine, Chernivtsi by Professor Z. D. Kovalyuk and Dr. Z. R. Kudrynskyi. Graphene was supplied by A. J. Marsden and Dr. N. R. Wilson from the University of Warwick. Preparation of the vdW nanosheets was carried out at The University of Nottingham by S. A. Svatek (PhD student) and myself, except for the samples measured under magnetic fields which were prepared at the Laboratoire National des Champs Magnétiques Intenses in Grenoble by Dr. K. Nogajewski and Dr. M. Molas.

### 3.1 Exfoliation and transfer methods of vdW crystals

#### 3.1.1 Mechanical exfoliation

Influenced by the techniques used to isolate single monolayers of graphene,<sup>1</sup> bulk crystals of III-VI semiconductors were mechanically exfoliated to produce nanosheets for characterisation and device fabrication. The general method used a low tack, low-residue tape to peel the nanosheets directly from the bulk crystals, which were then transferred to an intermediate polymer stamp or directly to a target substrate (*i.e.*, 500nm SiO<sub>2</sub>/Si wafers). The nanosheet thickness was identified by tapping-mode atomic-force microscopy (AFM) after initial sample identification by optical microscopy. For InSe, the mechanical exfoliation process produced a variety of nanosheets, with lateral dimensions in the range 10<sup>-1</sup> – 10<sup>2</sup> μm and thickness ranging from two-

monolayers (~2 nm) to micron-thick sheets. A single monolayer of InSe ( $L = 0.832$  nm) was not observed. Although not used in this project, the layer thickness of InSe nanosheets on SiO<sub>2</sub>/Si substrates can also be determined by optical contrast.<sup>180</sup> The approach has similar conclusions to the method of identifying monolayer and few-layer graphene on a SiO<sub>2</sub>/Si substrate, where the visibility of the van der Waals crystal is dependent upon the SiO<sub>2</sub> thickness and the wavelength of illuminating light.<sup>181</sup>

### 3.1.2 Deterministic transfer

A deterministic transfer set-up was constructed for the purpose of controlling the position and alignment of exfoliated vdW crystals and was based on the techniques detailed by Castellanos-Gomez *et al.*<sup>182</sup> Generally, the technique requires exfoliated nanosheets to be held on a transparent transfer arm, which can be positioned above a target substrate beneath an optical microscope. Layered crystals were mechanically exfoliated onto a transparent polymer stamp (Gel-pak, DGL film -50/17-X4), which adhered readily (*i.e.*, without adhesive) to a standard glass microscope slide. The exfoliated crystals were then characterised by atomic force microscopy (AFM), photoluminescence (PL) or Raman spectroscopy before continuing with the transfer. Following the characterisation, the microscope slide was attached to a transfer arm with the exfoliated nanosheets face down above the substrate. The mount for the substrate consisted of a copper plate on top of two linear translational stages in a *xy*-configuration (M-511.HD stages from Physik Instrumente). Double-sided polyamide tape was used to affix the substrate to the mount. The transfer arm was operated by hand controlled *x*-, *y*- and *z*-micrometres and the alignment of the exfoliated crystals above the substrate was observed through an optical microscope system. Following alignment in the *xy*-planes, the *z*-micrometer was adjusted to bring the exfoliated crystal and substrate into contact. At this stage it was possible, if necessary, to

adjust the temperature of the substrate using a resistive heater in the copper plate to promote a successful transfer. The temperature was controlled by a Lakeshore LS331S heating unit and computer running Labview. To complete the transfer, the z-micrometer was adjusted incrementally in order to peel the stamp from the substrate surface. Slow and controlled adjustments to the z-micrometer usually resulted in a complete transfer of the exfoliated crystal from stamp to substrate. Plans have been made to incorporate a rotational stage into the deterministic stamping set-up to further control the alignment. Additionally, it may also be possible to replace the copper heating unit by a Peltier device should rapid cooling ever be required. A schematic of the equipment used is shown in Figure 3.1.

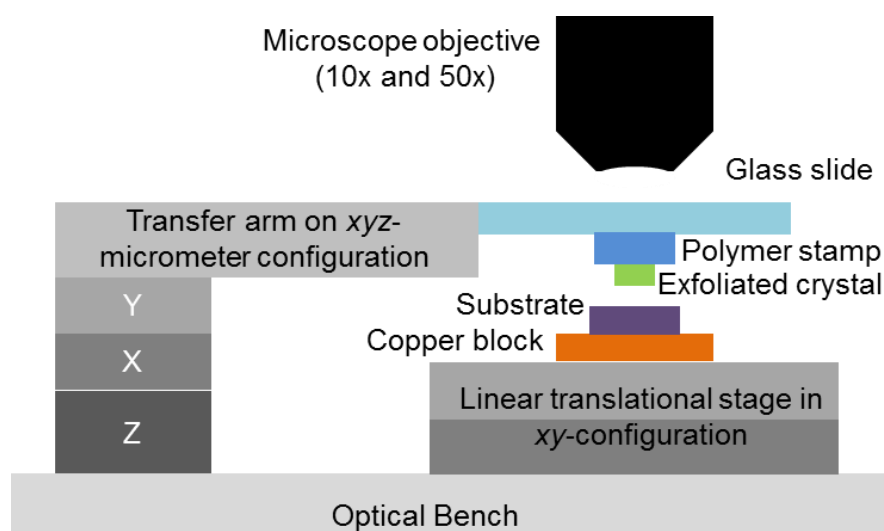


**Figure 3.1.** Diagram of the deterministic transfer set-up. A polymer stamp on a transparent microscope glass slide holds exfoliated van der Waals crystals above a target substrate. The glass slide is attached to a transfer arm and is manoeuvred by x-, y- and z-micrometers. The target substrate is controlled by two motorised, linear translational stages in a xy-configuration. The exfoliated crystals and target substrate are aligned beneath an optical microscope system. A copper plate with resistive heater is used as a mount for the target substrate. Temperature control, motorised stage movement and microscope image collection are controlled by a computer running Labview.

### 3.2 Microfabrication techniques

A range of structures were fabricated from van der Waals crystals using clean room based microfabrication techniques including

electron beam lithography (EBL), oxygen plasma etching and thin metal deposition by thermal evaporation.

### 3.2.1 Planar metal-InSe junctions

Exfoliated nanosheets of *n*-InSe were deposited onto SiO<sub>2</sub>/Si substrates (300 or 500 nm oxide thickness). A contact geometry for planar devices was defined by EBL patterning of dual layers of poly(methyl methacrylate) resin (PMMA). The dual layer was formed by first spin-coating a single layer of PMMA (8% in anisole with molecular weight 495K) at 4000rpm for 60s on the target substrate. Immediately after spin-coating, the substrate was transferred to a hotplate preheated to  $T = 180^{\circ}\text{C}$  for 10 minutes to partially bake the PMMA. The polymer-substrate stack was then left to cool to room temperature before further spin-coating with a second layer of PMMA (2% in anisole with molecular weight 950K); again at 4000rpm for 60s, followed by a partial bake for 10 mins at  $T = 180^{\circ}\text{C}$ .

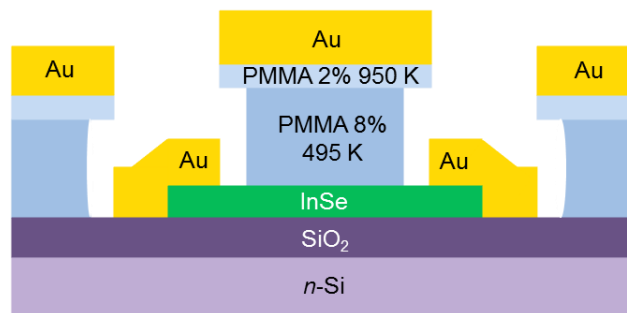


**Figure 3.2.** Sketch of an ‘overhang’ feature developed in a PMMA dual-layer. Metal deposited on the PMMA surface is abruptly separated from metal deposited in the geometry defined by the contact mask and increases the yield of clean devices.

EBL patterning of the dual polymer layer was carried out with a JEOL/XENOS JSM-7000F + XPG2 scanning electron microscope (SEM), modified with XENOS equipment for lithography purposes. The EBL set-up enabled the patterning of surfaces using a focussed electron beam within a single field of view ( $\sim 500 \mu\text{m}^2$ ). Larger patterns require the movement of the substrate, which was mounted on a

Kleindiek (KD) *xy*-translational stage and could result in small ( $\sim 1 \mu\text{m}$ ) pattern stitching faults. Writing patterns were custom defined by using the 'Exposure Control Program' from XENOS Semiconductor Technologies, which communicated with the XPG2 writer control unit. The dual layer of PMMA was used as a high resolution positive resist where electron beam exposure ( $\sim 320 \mu\text{C}/\text{cm}^2$ ) caused scission of the polymer chains. Developing in an IPA (Isopropanol) and deionised water solution (3:1) removed the broken, shorter chain molecules leaving the unexposed PMMA as a mask for metal deposition by thermal evaporation. The molecular weight of the PMMA layers determines the extent of the lateral exposure when under a focussed electron beam. Electrons penetrate further into the layer with least molecular weight (PMMA A8 495K) and result in an 'overhang' of the upper layer after development (Figure 3.2). The EBL developed dual-layer promotes an abrupt separation between polymer and sample surface during the deposition of evaporated metals and aids with the formation of 'clean' contact geometries.

Following EBL development of the polymer mask, the polymer-substrate stack was loaded into an Edwards Auto 306 thermal evaporator for the deposition of thin metal films. The typical composition of contacts deposited onto the exfoliated crystals consisted of a 5-10 nm Ti adhesion layer followed by a 100-150 nm Au layer. Deposition rates of 0.1 and 0.2  $\text{nm s}^{-1}$ , at currents of 26 and 32 A were used, respectively. The metal-polymer-substrate was then allowed to cool to room temperature before the lift-off procedure. The excess metal was removed by immersion in acetone at  $T = 60^\circ\text{C}$  for  $\sim 1$ -3 hours. Acetone acts to remove unexposed PMMA and therefore any metal that is not in direct contact with the substrate surface is also removed. The metal-substrate stack was then further rinsed with IPA and gently dried by a pressurised nitrogen gas stream. The resulting

metal-vdW crystal junction was then mounted on a suitable header and wire-bonded.

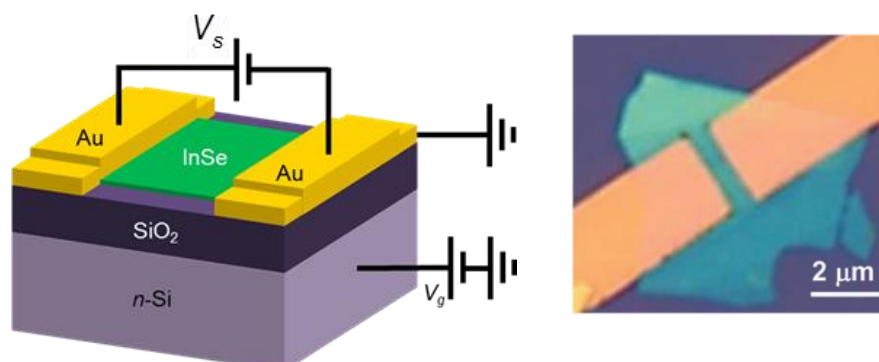


**Figure 3.3.** Schematic and optical image of a planar metal-InSe junction. Standard EBL processing is used to deposit Au/Ti contacts onto an exfoliated  $\gamma$ -InSe nanosheet on a  $\text{SiO}_2/\text{Si}$  substrate.

For inverted structures, a vdW crystal was deterministically transferred onto metal electrodes. In some cases, this resulted in a suspension of the vdW crystal above the  $\text{SiO}_2/\text{Si}$  substrate.

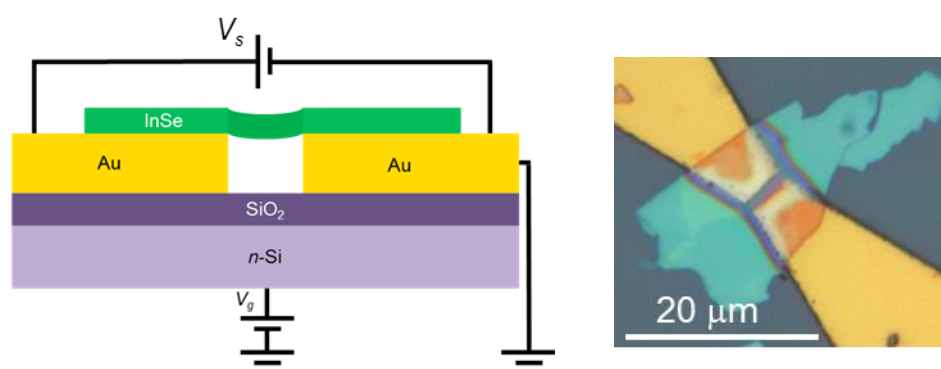


**Figure 3.4.** Schematic and optical image of an InSe-metal structure. Provided the channel length between the contacts is short enough, it was possible to suspend the deterministically transferred vdW sheets.

### 3.2.3 Planar graphene-InSe-graphene heterostructures

In more advanced device architectures, CVD-grown graphene was used as an electrode to form a graphene- $n$ -InSe interface. The CVD-grown graphene was supplied by A. J. Marsden and Dr. N. R. Wilson from the University of Warwick. The processing of devices incorporating CVD-graphene was developed by S. A. Svatek and Prof. P. H. Beton at The University of Nottingham.

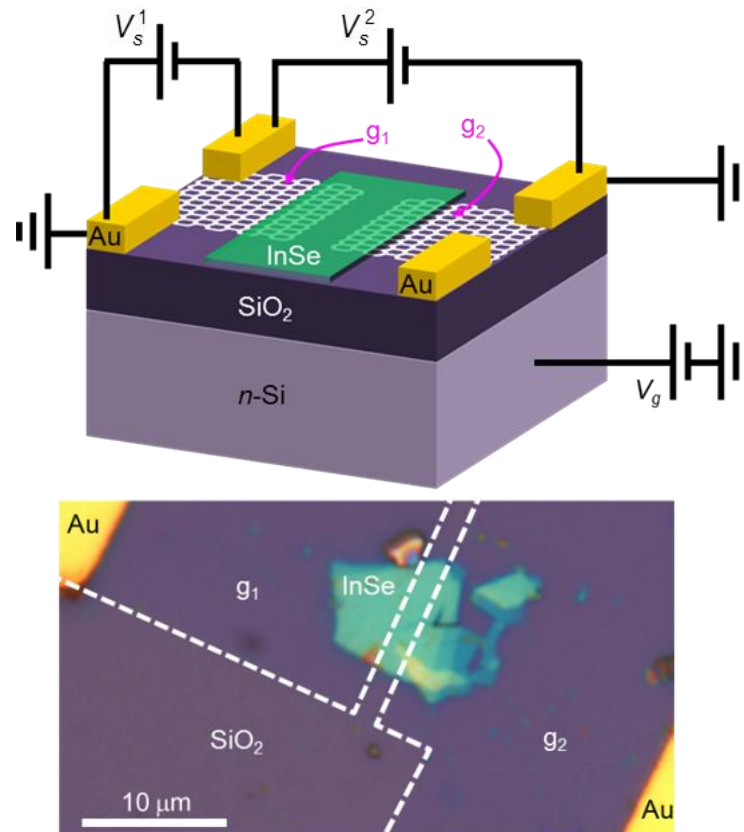


**Figure 3.5.** A schematic and optical image of a planar graphene-InSe heterostructure. EBL patterning and Ar/O<sub>2</sub> plasma etching are used to fabricate two graphene electrodes from a CVD-grown sheet. A  $\gamma$ -InSe nanosheet is then deposited bridging the individual graphene sheets in a nitrogen atmosphere. Contact pads (Au/Ti) allow for transport measurements to be taken through the individual graphene sheets *i.e.*,  $V_s^1$  and across the graphene-InSe-graphene planar heterostructure *i.e.*,  $V_s^2$ .

The CVD-graphene sheets were grown on a copper substrate. The copper was removed before transferring the graphene onto a SiO<sub>2</sub>/Si substrate for EBL processing. A single-layer of PMMA was spin-coated to the graphene surface of the graphene-copper stack using a similar method as described in Section 3.2.1. Once partially baked, the PMMA layer provided an easily observable support for the graphene. The copper substrate was removed after being placed onto the surface of FeCl<sub>3</sub> etchant (Transene, CE-100). The PMMA-graphene stack was then rinsed in a hydrochloric acid bath, followed by further rinsing in deionised water before being placed onto a substrate and allowed to dry for a period of ~48 hours (ambient conditions). After

drying, the PMMA layer was removed from the top of the PMMA-graphene-substrate stack by immersion in acetone ( $T = 60^{\circ}\text{C}$  for  $t = 1\text{-}2$  mins), rinsing in IPA and annealing in an Ar:H (95:5) gas mixture at  $400^{\circ}\text{C}$  for several hours. A mask for the graphene electrodes was fabricated by similar EBL methods used previously (Section 3.2.1). Any graphene unprotected by the PMMA mask was subsequently removed by etching in an Ar/O<sub>2</sub> plasma. After the removal of the PMMA mask (as described previously), the patterned graphene substrate was transferred to a nitrogen atmosphere for the exfoliation of a vdW crystal (i.e. *n*-InSe). Each graphene sheet was contacted to two Au/Ti metal pads which allowed the individual sheets, as well as the graphene-InSe-graphene planar heterostructure, to be characterised.

### **3.2.4 Vertical graphene-InSe-graphene heterostructures**

The fabrication processing of vertical heterostructures is more complex than for the planar architectures. Two different fabrication processes were used, one using exfoliated graphene (Method A), while the second used CVD-grown graphene sheets (Method B). Method A was used at the University of Manchester by Dr. L. Hague (Prof. K. S. Novoselov). Method B was developed by S. A. Svatek and Prof. P. H. Beton at The University of Nottingham.

#### **3.2.4.1 Method A: Exfoliated graphene**

Method A used a deterministic transfer method to stack layers of exfoliated graphene and  $\gamma$ -InSe layers in an overlaying vertical graphene-InSe-graphene heterostructure. A single metal contact was deposited onto each graphene electrode, which allowed electrical measurements to be taken through the graphene-InSe-graphene vertical heterostructure (Figure 3.6).

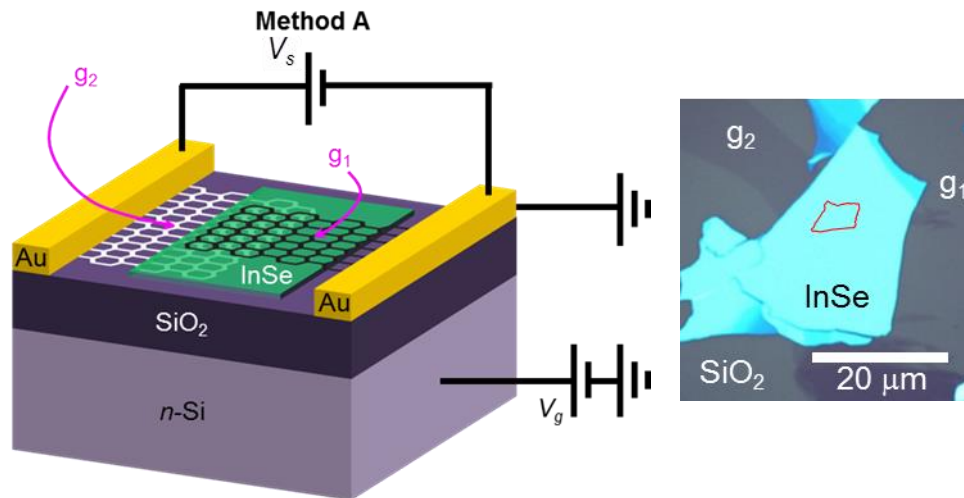


**Figure 3.6.** A vertical graphene-InSe-graphene heterostructure produced by method A. Exfoliated layers of graphene and  $\gamma$ -InSe are deterministically transferred to form a vertical stack with an overlay area between the graphene sheets separated by the  $\gamma$ -InSe. Metal contact pads are deposited onto the graphene electrodes following the placement of the vdW stack on a SiO<sub>2</sub>/Si substrate.

### 3.2.4.2 Method B: CVD-graphene

Method B produced vertical graphene-InSe-graphene heterostructures by EBL patterning of large area CVD-grown graphene sheets and an isolating polymer layer. As in Section 3.2.3, a CVD graphene sheet was deposited on a 300 nm SiO<sub>2</sub>/Si substrate and cleaned. Mechanical exfoliation was used to deposit InSe nanosheets, which were then identified by optical microscopy and PL measurements. The graphene layer was patterned and etched using an Ar/O<sub>2</sub> plasma to leave a graphene strip, which provided a continuous connection to the unexposed graphene beneath the selected InSe nanosheets. Au/Ti contact pads were deposited at each end of the graphene strip allowing the graphene and the heterostructure to be characterised. Contacts for the top strip were also deposited during this stage. An isolation layer was formed by EBL patterning of AR-N, a negative resist. The AR-N layer completely covered the lower graphene strip and edges of the InSe nanosheet in order to avoid the formation of electrical shorts between the upper and lower graphene strips. A window with an area of  $\sim 2 \times 2 \mu\text{m}^2$  was

developed in the AR-N layer on the top surface of the InSe layer to facilitate the mechanical contact to the upper graphene layer. A second layer of CVD graphene was then deposited and patterned via EBL into an upper graphene strip (running perpendicular to the lower strip) forming the final graphene-InSe-graphene heterostructure (Figure 3.7).

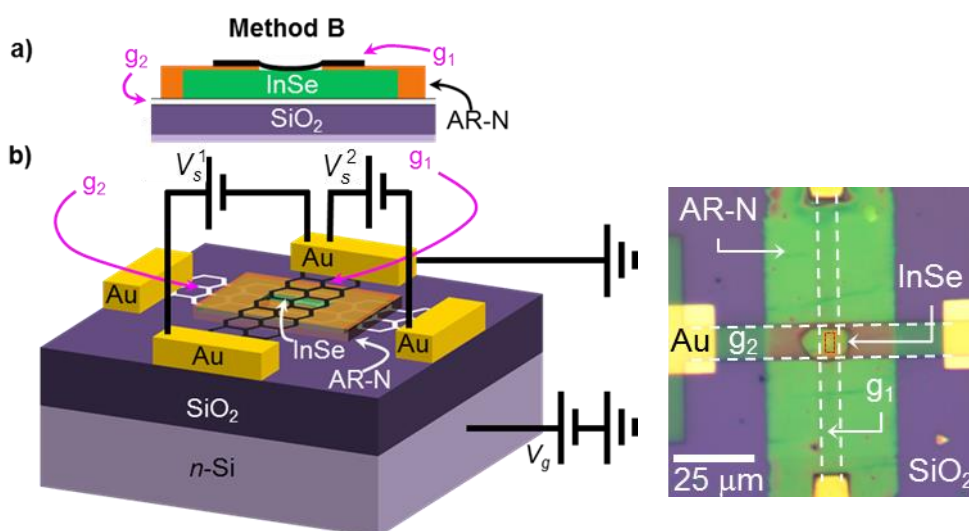


**Figure 3.7.** **a)** A cross-section through the vertical graphene-InSe-graphene heterostructure. The upper graphene electrode ( $g_1$ ) is able to form a mechanical contact to the  $\gamma$ -InSe nanosheet through a window that was patterned (EBL) into the AR-N isolation layer. **b)** A schematic and optical image of a vertical graphene-InSe-graphene heterostructure produced by method B. Two CVD-grown graphene sheets are used to form electrodes and are patterned by EBL and Ar/O<sub>2</sub> plasma etching. The upper ( $g_1$ ) and lower ( $g_2$ ) electrodes (perpendicular) are separated by a  $\gamma$ -InSe nanosheet and an AR-N isolation layer. Each graphene electrode has two contact pads which enable transport measurements to be taken through the individual graphene sheets *i.e.*,  $V_s^1$  and through the graphene-InSe-graphene heterostructure *i.e.*,  $V_s^2$ .

### 3.3 Experimental techniques: Optical characterisation

#### 3.3.1 Room temperature micro-photoluminescence and Raman spectroscopy

The optical properties of exfoliated  $\gamma$ -InSe nanosheets, devices and heterostructures were investigated by a micro-photoluminescence ( $\mu$ PL) and Raman spectroscopy system. The samples were mounted

on a motorized  $xy$  linear positioning stage (step size  $0.1 \mu\text{m}$ ) and were excited by either a He-Ne or frequency doubled Nd:YVO<sub>4</sub> laser ( $\lambda = 633 \text{ nm}$  and  $532 \text{ nm}$ , respectively). A confocal microscope system was used to focus the laser excitation onto the sample and to direct the emitted signal to the detector components. A LabRAM HR-UV spectrometer equipped with 150 and 1200 grooves/mm gratings, Si charge-coupled device (CCD) and liquid-nitrogen cooled (InGa)As array photodetector were used in the detection of the optical emission from the sample. The range of detection wavelengths accessible for the CCD and InGa(As) photodetector are  $\Delta\lambda_{\text{CCD}} = 350\text{-}1100 \text{ nm}$  and  $\Delta\lambda_{\text{InGa(As)}} = 800\text{-}1600 \text{ nm}$ . A range of objectives provided 10x, 50x and 100x optical magnification with focal length  $f_L = 18, 3.6$  and  $1.8 \text{ mm}$  and numerical aperture  $NA = 0.25, 0.55$  and  $0.9$ , respectively. The beam was focussed close to the diffraction limit to a diameter  $d \sim 1 \mu\text{m}$  primarily using the 100x objective. The Rayleigh criterion was used to estimate the beam diameter,

$$d_R = 1.22 \times \frac{\lambda}{NA}. \quad (3.1)$$

For  $\lambda = 633 \text{ nm}$  and  $NA = 0.9$ , then  $d_R = 0.86 \mu\text{m}$ , which corresponds to the spatial resolution of the confocal microscope. Use of a pinhole aperture offers further control, acting to block the contribution of signal emitted outside the sampling area and focal plane, leading to a reduced depth of focus. The aperture diameter ( $200 \mu\text{m}$ ) was selected to be small enough to ensure high spatial resolution, but large enough to allow sufficient signal to reach the detector. Spectra were obtained at low powers ( $P > 100 \mu\text{W}$ ) to avoid lattice heating.

### 3.3.2 Low temperature micro-photoluminescence spectroscopy

For temperature dependent measurements, a cold-finger optical cryostat replaced the motorised linear stage and introduced a  $1 \text{ mm}$

sapphire window to the optical path. Samples were held in vacuum, affixed to a copper plate by thermally conducting silver paint. The copper plate was cooled by contact with a liquid helium flux and reached temperatures as low as  $T \sim 8$  K. Constant helium flux was supplied via a transfer tube from a helium dewar with an external pressure regulator. Intermediate temperatures between  $T = 8$  K and 300 K were reached by balancing the level of helium flux against the output of the cryostat internal heaters (controlled by a Lakeshore LS331S temperature control unit). The distance from sample surface to the underside of the optical window can be adjusted from 0 to 3 mm. Mapping capabilities were retained through the use of a motorised scanning mirror above the objective, albeit for a reduction in scan size ( $< 5 \times 5 \mu\text{m}^2$  for the 100x magnification) due to a loss of focus caused by the slight changes to the optical path. The scanning mirror mode was also available for the room temperature set-up when stage movement needed to be minimised.

### 3.3.3 Magneto-photoluminescence spectroscopy

Magneto-optical studies were undertaken at The Laboratoire National des Champs Magnétiques Intenses (LNCMI) in Grenoble, France. Samples were mounted on a piezoelectric, xyz-motorised stack in a continuous gas flow cryostat at liquid He temperature ( $T \sim 4.5$  K). Optical fibres were used in a  $\mu\text{PL}$  set-up for excitation of the sample with an Ar CW laser ( $\lambda = 514.5$  nm) and to collect the emitted optical signal. Resistive magnets provided magnetic fields of up to  $B = 30$  T in a Faraday configuration. The laser beam diameter was focussed to  $d \sim 1 \mu\text{m}$  using a 50x objective. The detection of the signal was made using a 0.5 m monochromator with 300 g/mm grating and CCD camera. Due to the use of optical fibres in the system, the magnetic-field-induced rotation of the linear polarization angle (Faraday effect) can induce a modulation of the PL emission intensity.<sup>183,184</sup>

### 3.4 Experimental techniques: Atomic force microscopy

Topological images of vdW crystals (*i.e.*, InSe and graphene) were acquired by atomic force microscopy (AFM) in tapping mode under ambient conditions. A MFP-3D system supplied by Asylum Research (Oxford Instruments) was used with Windsor Scientific Multi 75Al-G AFM probes. The MFP-3D system has a sub-angstrom resolution in the  $z$  direction and nanometre resolution in the  $xy$  plane, dependent upon tip quality. The AFM system monitors the oscillation amplitude of a cantilever with sharp tip, through reflection of an infrared laser onto a split-quadrant photodiode. A feedback loop monitors the  $z$  readout for the cantilever. During scanning, the application of a voltage to a piezoelectric motor adjusts the  $z$  height to accommodate for any detected changes. A voltage-distance calibration factor is applied to determine the  $z$  height of the tip from the feedback voltage at given  $xy$  coordinates and provides a topographical image of the sample surface. AFM resolution is typically beyond the diffraction limit associated with traditional optical imaging systems. AFM measurements were primarily used to determine the apparent height of exfoliated samples and fabricated devices.

### 3.5 Experimental techniques: Transport studies

#### 3.5.1 Current-Voltage ( $I$ - $V$ ) characteristics

The  $I$ - $V$  characteristics of devices fabricated from van der Waals crystals were first measured under dark conditions. Devices were connected with a Keithley 2400 DC voltage source in a two-probe configuration. The photocurrent versus applied voltage (DC) was acquired in a similar manner by exposing the devices to an unfocussed beam from a He-Ne laser ( $\lambda = 633$  nm and  $P$  up to 1mW). Further DC photocurrent measurements were taken using the  $\mu$ PL set-up where the laser beam was focussed to a diameter  $d \sim 1$   $\mu$ m ( $\lambda = 633$  nm and  $P < 0.1$  mW). Scanning the beam across the surface by using the

motorised stage produced photocurrent maps, which highlighted the light-sensitive regions of the devices.

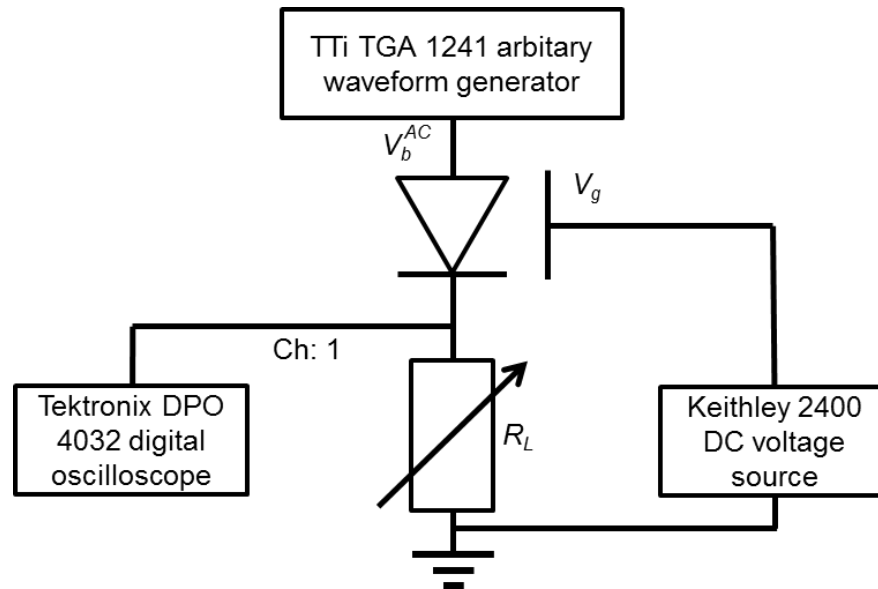


**Figure 3.8.** Set-up used for temporal studies of the devices under dark conditions. A TTI TGA 1241 arbitrary waveform generator and  $1\text{ M}\Omega$  load resistor were connected in series with the device. A gate voltage was applied using a Keithley 2400 DC voltage source. The dark current was measured by observing the voltage drop across the load resistor using a Tektronix DPO 4032 digital oscilloscope.

For temporal studies under dark conditions, the Keithley 2400 DC voltage source was replaced by a TTI TGA 1241 arbitrary waveform generator and the device was connected in series with a  $1\text{ M}\Omega$  load resistor. Low noise signals were measured using a Tektronix DPO 4032 digital oscilloscope by measuring the voltage drop across the load resistor. The response of the dark current to an AC square driving signal was studied in the frequency range  $f = 10^{-1}$ – $10^5$  Hz. Temporal studies of the photocurrent were measured using a similar set-up which reverted back to the Keithley 2400 DC voltage source in place of the TTI TGA 1241 arbitrary waveform generator. An unfocussed, mechanically modulated He-Ne laser ( $\lambda = 633\text{ nm}$  and  $P$  up to  $1\text{ mW}$ ) was used to generate an AC signal from the photogeneration and recombination of charge carriers. The

photocurrent signal was investigated in the frequency range  $f = 1 - 400$  Hz.

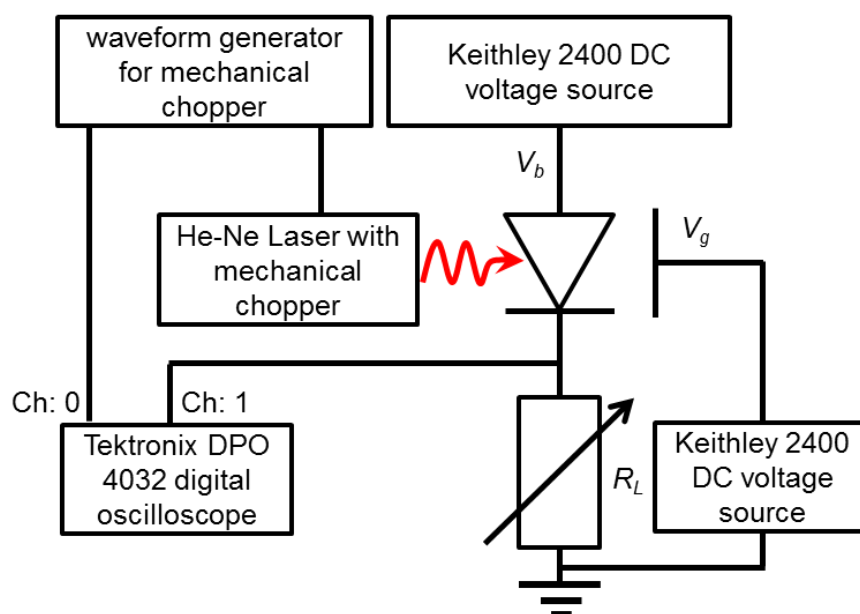


**Figure 3.9.** Set-up used for temporal studies of the photocurrent. A Keithley 2400 DC voltage source and  $1 \text{ M}\Omega$  load resistor were connected in series with the device. A gate voltage was applied using a Keithley 2400 DC voltage source. Photocurrent was determined by measuring the voltage drop across the load resistor using a Tektronix DPO 4032 digital oscilloscope.

### 3.5.2 Photocurrent spectroscopy

For sensitive photocurrent measurements at different photon wavelengths, a Keithley 2400 DC voltage source was connected in series with the device and a variable resistor ( $R = 1 - 100 \text{ M}\Omega$ ). Light from a 250 W, quartz halogen lamp was dispersed through a 0.25 m monochromator (bandwidth of  $\sim 10 \text{ nm}$ ), modulated with a mechanical chopper and focussed onto the device. The photoinduced current was measured by observing the voltage drop across the load resistor using a Stanford SR830 lock-in amplifier by a standard lock-in amplification technique.

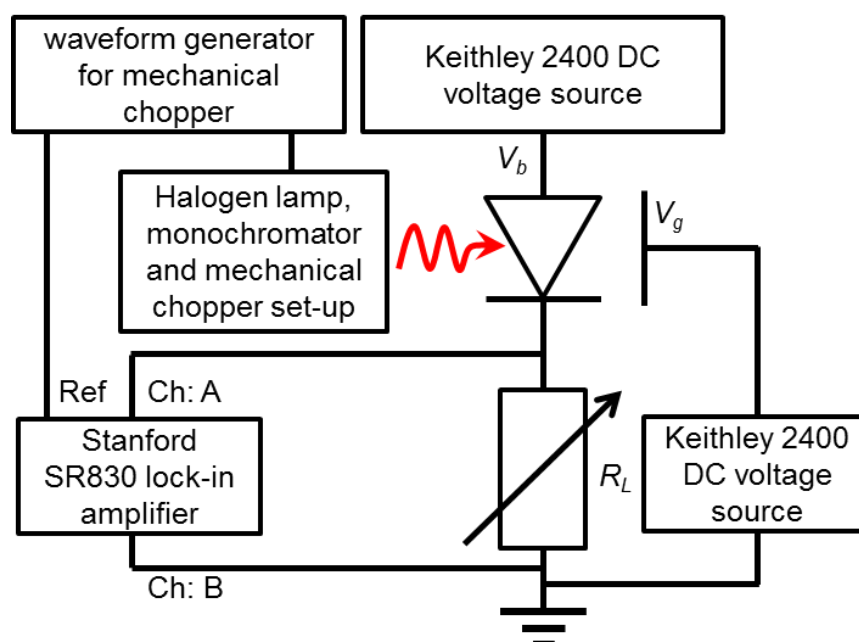


**Figure 3.10.** Photocurrent spectroscopy set-up. A Keithley 2400 DC voltage source and 1 M $\Omega$  load resistor were connected in series with the device. A gate voltage was applied using a second Keithley 2400 DC voltage source. A photocurrent signal was generated by mechanically modulated light from a 250 W, quartz halogen lamp dispersed through a 0.25 m monochromator. The photocurrent was measured by observing the voltage drop across the load resistor using a Stanford SR830 lock-in amplifier.

## Chapter 4

### Tuning the band gap of InSe nanosheets by quantum confinement

This chapter describes the effects of quantum confinement on photoexcited carriers generated in exfoliated layers of  $\gamma$ -InSe. The optical properties of the nanosheets were probed by micro-photoluminescence ( $\mu$ PL), Raman and photocurrent (PC) spectroscopy. Topographical images were obtained by atomic force microscopy (AFM) scans. Section 3.1.1 explains the preparation of the exfoliated layers, Section 3.2.1 describes the fabrication of planar metal-InSe devices for PC, and Sections 3.5.1 and 3.5.2 provide details of the transport measurements. PL and Raman spectra, PL maps and AFM scans were collected by myself, and the photocurrent spectroscopy measurements were taken with T. H. Ren, a 3<sup>rd</sup> year undergraduate student at The University of Nottingham. Density functional theory (DFT) band structure calculations were provided by the group of Prof. V. Falco of the National Graphene Institute, The University of Manchester. Results presented in this chapter were published in *Advanced Materials*, **25**, 5714 (2013).

#### 4.1 Introduction

Quantum mechanical effects arise in layered semiconductor systems as the crystal thickness is decreased. Charge carriers are confined in the axis perpendicular to the layered plane (*c*-axis) and quantum well (QW) structures are formed. A consequence of the confinement is the modification of the crystal optical and electronic properties, which can be tuned through control over the number of layers in the nanosheet, providing routes to engineer the electronic structure of materials at the nanoscale. Perhaps the most striking

demonstration of layer dependent effects on the optical properties of 2D crystals occurs in MoS<sub>2</sub>. When exfoliated to a single layer, the MoS<sub>2</sub> band gap undergoes a transition from indirect-to-direct and a significant increase in the photoluminescence emission intensity occurs. However, the practicalities of optical tuning by confinement in MoS<sub>2</sub> systems is lost when moving beyond the limit of a single layer, as the band gap reverts back to an indirect transition.<sup>7,8</sup> The III-VI compound of indium selenide (InSe) provides a qualitatively different vdW system to the transition metal dichalcogenides (TMDCs) such as MoS<sub>2</sub> due to, amongst other differences, the presence of a direct-band gap in bulk form.<sup>106,119,185–191</sup> In this chapter, I demonstrate that the room temperature photoluminescence from exfoliated layers of  $\gamma$ -InSe exhibits a large energy blue-shift as the crystal thickness is reduced to a few nanometres. The effects of confinement are also apparent in the photocurrent spectroscopy measurements. Room temperature Raman spectroscopy from layers down to  $L \sim 6$  nm are also presented. A comparison of the thickness-dependent optical spectroscopy provides experimental evidence of a direct-to-indirect transition as InSe approaches the 2D limit, which is qualitatively distinct from the indirect-to-direct transition occurring in the TMDCs.<sup>8,56,192</sup>

## 4.2 Tunable photoluminescence emission

The normalised room temperature PL spectra of InSe nanosheets are shown in Figure 4.1. For  $L = 20$  nm the InSe nanosheets emit at photon energies centred around  $h\nu \sim 1.25$  eV, which corresponds to the excitonic emission in bulk InSe, taking into account the band gap ( $E_g = 1.2635$  eV) and the excitonic binding energy ( $E_b \sim 14$  meV).<sup>106,193</sup> With decreasing nanosheet thickness, the emission energy blue-shifts to higher energies, as seen for a nanosheet with  $L \sim 7$  nm which approaches  $h\nu \sim 1.5$  eV, as a result of increasing quantum confinement of the charge carriers along the *c*-axis. The exfoliated nanosheets are optically active in the near-

infrared spectral range between 1 and 0.8  $\mu\text{m}$ , and the emission persists for several months when they are left in air, indicating a high chemical stability. As the crystal thickness is reduced sufficiently, a quantum well is formed and the band-to-band direct edge transition energy,  $E_{2D}$ , can be modelled using a square potential of infinite height, *i.e.*,

$$E_{2D} = E_g - E_b + \frac{\pi^2 \hbar^2}{2L^2 \mu_c} \quad (4.1)$$

where  $\mu_c = (1/m_e^* + 1/m_h^*)^{-1} = 0.054m_0$  is the exciton reduced mass, as derived from the measured effective mass of the electron ( $m_e^* = 0.08m_0$ )<sup>187</sup> and hole ( $m_h^* = 0.17m_0$ )<sup>194</sup> for motion along the *c*-axis in bulk InSe,  $E_b \sim 14$  meV is the exciton binding energy,<sup>106,193</sup> and  $m_0$  is the electron rest mass in vacuum.

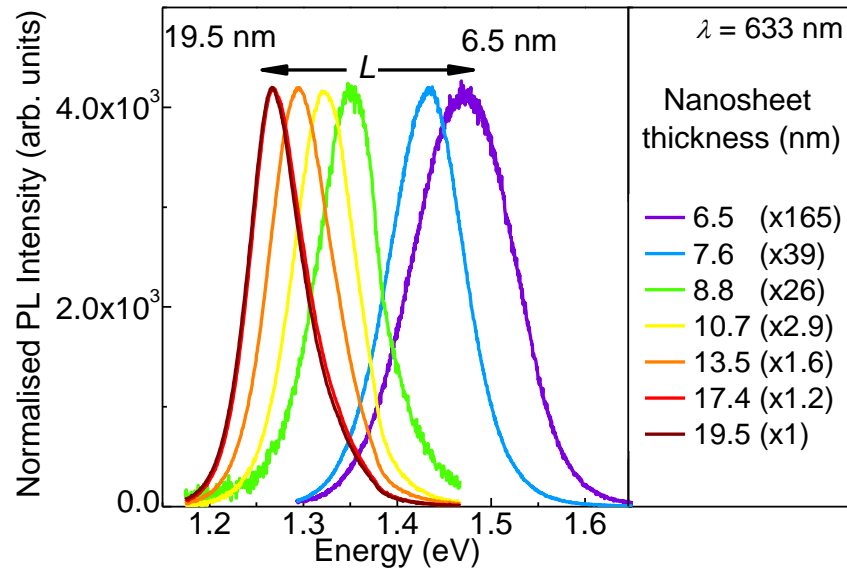


**Figure 4.1.** Normalised room temperature PL emission observed from exfoliated  $\gamma$ -InSe nanosheets with  $L \sim 7 - 20$  nm ( $\lambda = 633$  nm and  $P < 0.1$  mW).

The effective mass model (Equation 4.1) reproduces the layer dependence of the central peak PL emission energy, shown in Figure 4.2. Quantum confinement effects are stronger in InSe compared to other III-VI compounds, such as GaSe, due to the smaller exciton

reduced mass ( $\mu_c = 0.054m_0$ ). As a result, carriers experience a stronger sensitivity to the roughness of the layers, as revealed by the layer dependence of the PL optical linewidth (see Section 4.3). The inset of Figure 4.2 presents representative room temperature PL spectra of the thinnest measured InSe nanosheets. For these measurements, a higher energy excitation source ( $\lambda = 532$  nm) had to be used due to the significant increase in the band gap energy. A blue-shift of over 600 meV is observed in the PL emission energy for a nanosheet with  $L \sim 1.7$  nm.

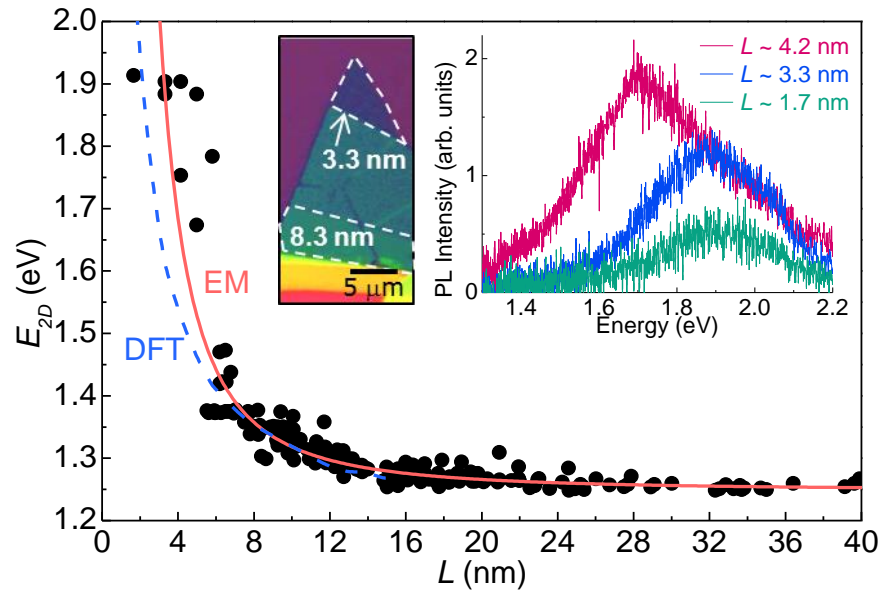


**Figure 4.2.** Calculated (line) and measured (symbols) energy shift of the band gap of  $\gamma$ -InSe nanosheets versus thickness  $L$  ( $\lambda = 633$  nm  $P < 0.1$  mW). The calculated energy shift is derived from DFT calculations (dashed) and from a square quantum well potential of infinite height in the effective mass (EM) approximation (solid). The inset presents an optical image and representative PL spectra from the thinnest measured nanosheets ( $\lambda = 532$  nm,  $P < 0.1$  mW).

Deviations of the PL emission data from the effective mass model ( $E_{2D}$ ) may come from the difference between the hard wall potential assumed by the model and the real confinement potential. In particular, charge carriers can be confined within an InSe nanosheet with an effective thickness that is smaller than that measured by AFM. Thin surface films, into which carrier wave functions do not penetrate,

can originate from the native oxidised surface layer that forms on as-grown InSe as a result of the chemisorption of water and oxygen molecules on a low density of dangling bonds on the InSe surface.<sup>119</sup> The method of matching the PL maps to the AFM scans, in order to identify emission from nanosheets in close proximity (and/or terraced nanostructures), may also provide deviations. Nevertheless, the large sample size investigated shows a good alignment of the PL data to the model of carrier confinement in a 2D quantum well.

### 4.3 Effects of nanosheet interface roughness

The systematic increase in the linewidth of the PL signal with decreasing thickness is attributed to monolayer fluctuations in the nanosheet surface height (Figure 4.3). The PL signal from quantum wells with thickness comparable to the exciton Bohr radius,  $a_{ex}$ , is dependent upon the uniformity of composition and abruptness of the interface.<sup>195,196</sup> A statistical model of the exciton PL emission was used to quantify the spectral linewidth. The model considers the roughness of the layers and the dependence of the exciton recombination energy,  $E_{2D}$ , on layer nanosheet thickness  $L$ . The model assumes that the two interfaces of the nanosheet are comparable in quality, that the well width fluctuates by one monolayer ( $\delta_1$ ) around its mean value  $L$  and that the roughness consists of islands with thickness  $L \pm \delta_1$  which have the same concentration and average lateral size  $\delta_2$ . AFM studies show that nanosheets tend to be almost flat on the atomic scale and show surface fluctuations of about one monolayer ( $\delta_1 = 0.832$  nm). The contribution of the interface roughness to the linewidth (full width at half maximum) is described as<sup>195,196</sup>

$$W_R = \sqrt{2.8}(\Delta^+ + \Delta^-) \frac{\delta_2}{4a_{ex}}, \quad (4.2)$$

where

$$\Delta^\pm = \delta_1 \left( \frac{\partial E_{2D}}{\partial L} \right)_{L \pm \delta_1} . \quad (4.3)$$

To describe the measured value of  $W$ , we consider a constant contribution to the linewidth ( $W_0$ ) from electron-phonon scattering and other disorder-related broadening effects that are assumed to be independent of  $L$ , *i.e.*,

$$W = W_0 + W_R \quad (4.4)$$

where  $W_0 = 64$  meV.

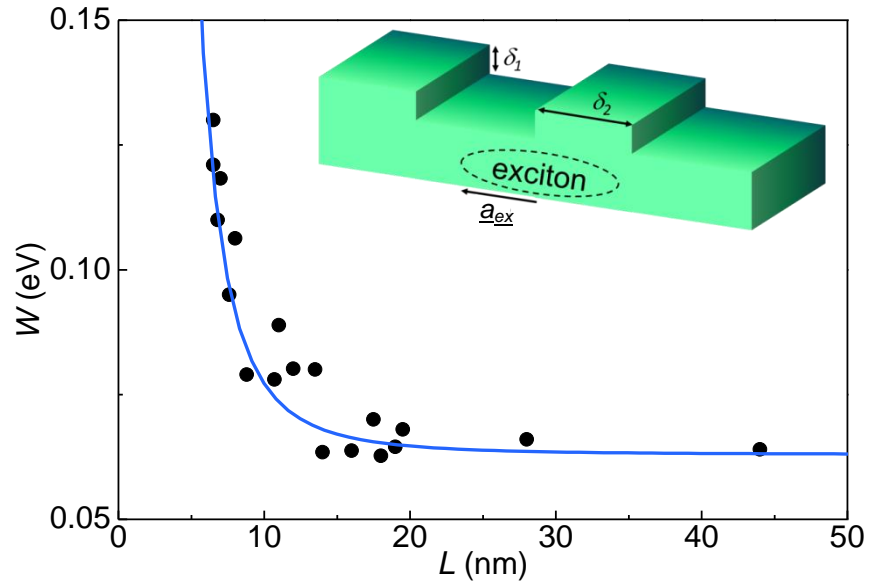


**Figure 4.3.** Measured (symbols) and calculated (line) of Full width half maximum ( $W$ ) of the PL emission versus the thickness of the nanosheet (symbols). The inset illustrates the parameters defined by the statistical model used to describe  $W$ .

The calculated value of  $W$  increases monotonically with decreasing  $L$  and reproduces the measured data (Figure 4.3) if the typical scale of the roughness ( $\delta_2$ ) is comparable to the exciton Bohr radius,

$$a_{\text{ex}} = \frac{4\pi\epsilon_0\epsilon_\infty\hbar^2}{e^2\mu_c}, \quad (4.5)$$

*i.e.*,  $\delta_2/a_{ex} = 1.4 \pm 0.6$ . For  $a_{ex} = 6.9$  nm this gives  $\delta_2 = 10 \pm 4$  nm. The agreement between the data and model provides evidence for the role of even a small degree of interface roughness on the PL linewidth of thin nanosheets.

#### 4.4 A direct-to-indirect band gap crossover

The room temperature integrated intensity of the PL from the exfoliated InSe nanosheets is observed to decrease with the nanosheet thickness, as shown in Figure 4.4. An estimation of the PL intensity,  $I_{PL}$ , was calculated from a simple model of the light intensity,  $I_{abs}$ , absorbed by the layer *i.e.*,

$$I_{PL} \propto I_{abs} = I_0[1 - \exp(-\alpha L)] \quad (4.6)$$

where  $I_0$  represents the intensity of light at the surface of the nanosheet (a fitting parameter) and  $\alpha$  is the absorption coefficient ( $\alpha \sim 4 \times 10^5 \text{ m}^{-1}$  at  $\lambda = 633$  nm).<sup>69,106</sup> The model assumes the lateral area of the sample region is constant for all nanosheets (*i.e.*, the focussed area of the laser spot). Our estimate of the PL intensity is in good agreement with the measurements from thicker nanosheets. However, there is a gradually stronger quench of the luminescent intensity for the thinnest measured nanosheets, which suggests that a reduction in layer number may be altering the intrinsic (*i.e.*, electronic band structure) and/or extrinsic (*i.e.*, enhancement of nonradiative recombination at surface/interface charge traps) properties of the crystal.

A change to the band structure of bulk InSe (direct-to-indirect transition) has already been observed under hydrostatic pressure studies<sup>189,194</sup> and in InSe nanoparticles by quantum confinement.<sup>197,198</sup> For the case of InSe nanoparticles, the intensity of the PL emission is dependent on the nanoparticle size due to the combined effects of the carrier confinement along the *c*-axis and in the *xy*-plane.<sup>197–199</sup>

Fluorescence is observed in small nanoparticles (confined in three dimensions to diameters of  $<5$  nm); in contrast, larger nanoparticles are non-fluorescent as confinement along the  $c$ -axis becomes a dominant effect, leading to a reversal in the direct and indirect optical transitions.<sup>197,198</sup> In the hydrostatic pressure studies, increasing pressure on bulk InSe crystals acts to shift the conduction band (CB) minimum at the  $Z$ -point of the Brillouin zone towards the upper  $B$ -minimum, leading to a direct-to-indirect transition.<sup>189,194</sup> Previously, we believed this may also be the case for InSe nanosheets. However, recent theoretical calculations, stimulated in part by our room temperature optical studies, provide evidence that modifications to the valence band (VB) are mainly responsible for the direct-to-indirect crossover in thin InSe.<sup>65,88,200–203</sup>

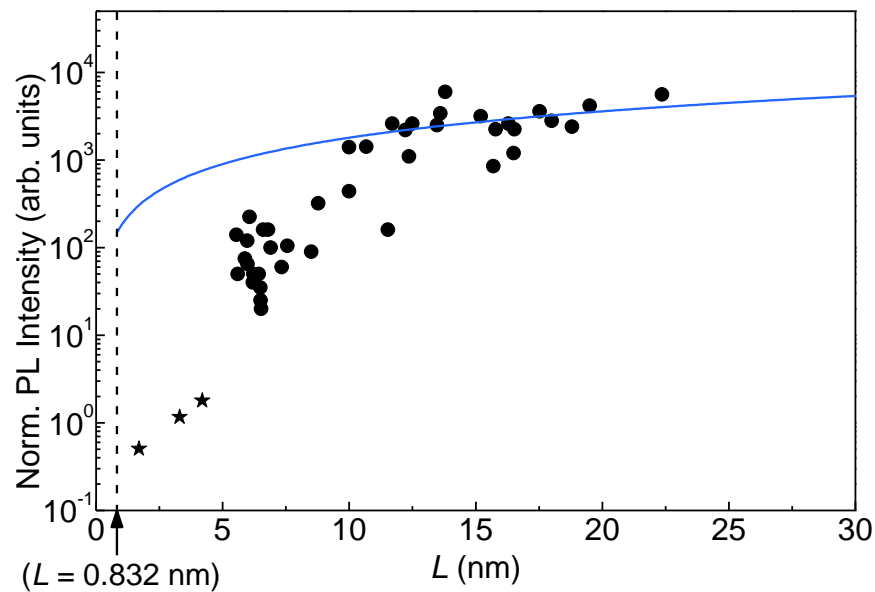


**Figure 4.4.** Measured (symbols) and calculated (line) PL emission intensity versus the thickness  $L$  of the nanosheets. Circles are for  $\lambda = 633$  nm and stars are for  $\lambda = 532$  nm.

Recent works in the literature suggest that a direct-to-indirect band gap transition occurs when the nanosheet thickness is reduced below a critical value.<sup>65,88,200,201</sup> Our colleagues at the National Graphene Institute at the University of Manchester have conducted density functional theory (DFT) calculations of the band structure of

InSe. As shown in Figure 4.5, when the layer thickness is reduced the conduction band minimum (CBM) remains at the  $\Gamma$ -point and shifts to higher energies; in contrast, the valence-band maximum (VBM) moves away from  $\Gamma$  towards the K-point, and its dispersion takes the form of a ‘Mexican hat’. In particular, for small  $L$  ( $< 5$  layers) the energy dispersion becomes anisotropic in the  $k$ -plane with 6-fold rotational symmetry. From Figure 4.6, it can be seen that for an InSe monolayer, the valence band comprises of six maxima that are arranged in a circle around  $\Gamma$ ; this anisotropy is not observed for 5 layers of InSe.

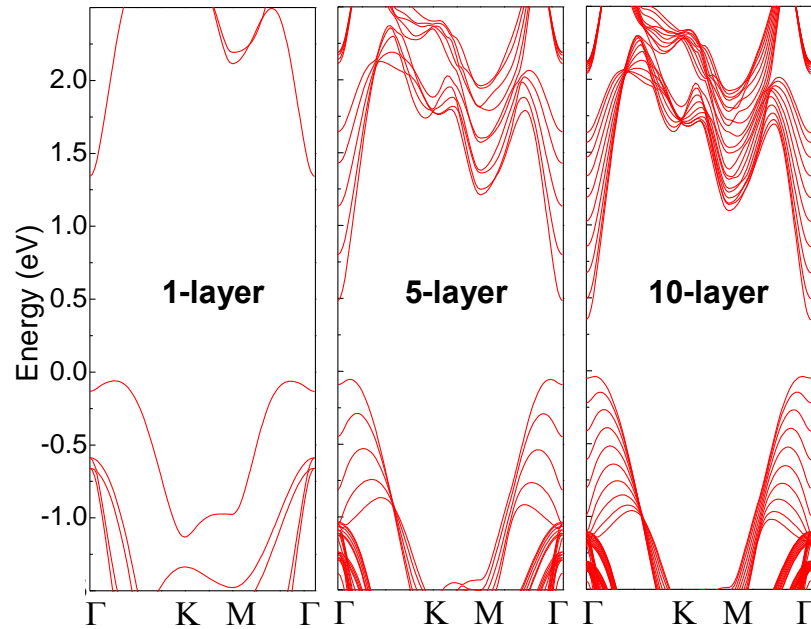


**Figure 4.5.** Density functional theory (DFT) calculations of the band structure of InSe with  $L = 1, 5$  and  $10$  layers.

To quantify the change of the VB with decreasing  $L$ , we focus on two parameters: the distance in  $k$ -space,  $k_r$ , of the valence band edge from  $\Gamma$ , and the energy separation  $\Delta E_{VB}$  between the valence band extremum at  $\Gamma$  and the VBM. With decreasing  $L$ ,  $\Delta E_{VB}$  increases from 0 to 0.07 eV; correspondingly,  $k_r$  shifts from 0 to about 30% of the size of the Brillouin zone along the  $\Gamma$ -K line ( $k_r \sim 3 \text{ nm}^{-1}$  for  $L = 1$  layer). Thus the crossover from a direct-to-indirect band gap occurs progressively with decreasing  $L$  due to a ‘soft’ change of the VB. For comparison to

the measured PL spectra, an estimate of the  $L$ -dependence of  $E_{2D}$  is derived from the bulk value of InSe ( $E_g = 1.2635$  eV), the excitonic binding energy ( $E_b \sim 14$  meV),<sup>106,193</sup> and the energy gap shift calculated by DFT (shown in Figure 4.2).

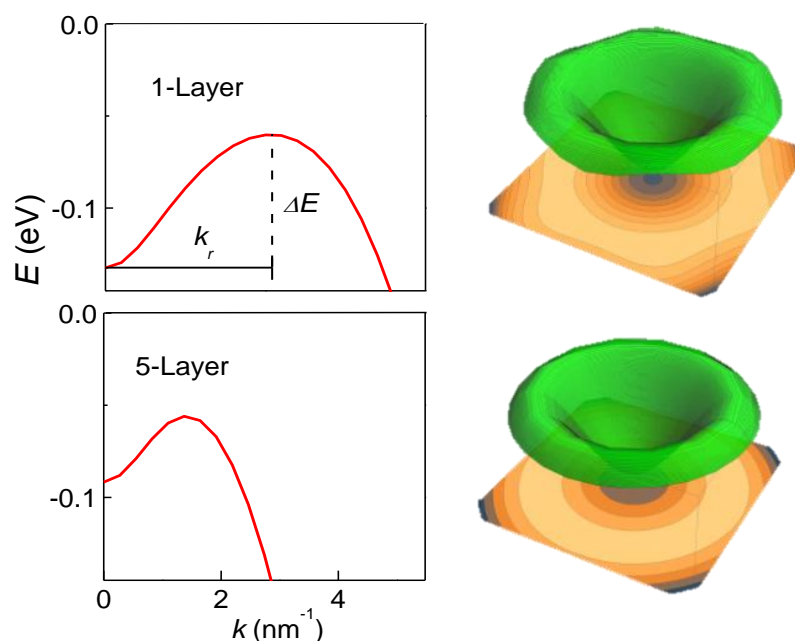


**Figure 4.6. a)** Valence band (VB) over a narrow range of energy and  $k$ -values in the Brillouin zone for monolayer and 5-layer InSe. The insets show contour plots of the VB energy dispersions in the  $k$ -plane centred at  $\Gamma$ .

Similar band structure changes and the formation of a Mexican hat valence band energy dispersion are common to other metal monochalcogenides and layered materials such as GaSe, GaS and InS;<sup>86,108,203,204</sup> monolayers of  $\text{Bi}_2\text{Te}_3$ ,<sup>205</sup>  $\text{BiSe}_3$ <sup>206</sup> and AB-stacked bilayer graphene (under a vertically applied electric field).<sup>207–209</sup> For metal monochalcogenide layered compounds, the valence band features could lead to tunable magnetism, superconductivity, and enhanced thermoelectricity.<sup>204,210</sup>

#### 4.5 Room temperature Raman spectroscopy

The polytype phase of as-grown InSe was determined previously by X-ray and Raman spectroscopy.<sup>211</sup> Room temperature Raman spectra of the exfoliated InSe nanosheets are presented in Figure 4.7a. Raman peaks centred at 115.7, 179.2, 201.2, 212.4 and

228.0  $\text{cm}^{-1}$  are indicative of the  $\gamma$ -polytype and the layer dependence of the intensity of the most prominent peaks (115.7 and 228.0  $\text{cm}^{-1}$ ) are shown in Figure 4.7b. Several Raman peaks were observed under non-resonant conditions using an excitation energy of  $h\nu = 1.96$  eV ( $\lambda = 633$  nm) and correspond to the  $A_1'$  ( $\Gamma_1^2$ ),  $E'$  ( $\Gamma_3^1$ )-TO and  $E''$  ( $\Gamma_3^3$ ),  $A_2''$  ( $\Gamma_1^1$ )-LO,  $E'$  ( $\Gamma_3^1$ )-LO and  $A_1'$  ( $\Gamma_1^3$ ) modes, respectively (shown in Figure 4.7c). Decreasing the thickness of the nanosheets (down to  $L \sim 6$  nm) does not cause a shift of the Raman peak positions and indicates that the material retains the same  $\gamma$ -polytype of the as-grown bulk crystals.

The absence of a layer dependent shift of the Raman peaks in the InSe nanosheets is likely to be due to the weak vdW interactions between the layers, resulting in a short (few-layer) vibration coherence length along the  $c$ -axis.<sup>212</sup> Schwarz *et al.* predicts that confinement effects may manifest in Raman measurements for a crystal thickness below the coherence length, predicting a shift for the  $A_1'$  ( $\Gamma_1^2$ ) and  $A_1'$  ( $\Gamma_1^3$ ) peaks for crystals of thickness below 5 layers ( $L \lesssim 4$  nm). Gacem *et al* and Chen *et al* suggest the Raman signal may approach that of  $\varepsilon$ -InSe in ultrathin nanosheets.<sup>213,214</sup>

In Figure 4.7, the Raman intensity for the  $A_1'$  ( $\Gamma_1^2$ ) and  $A_1'$  ( $\Gamma_1^3$ ) peaks is compared to a  $L$ -dependent absorption model and falls, as expected, from a reduction in the amount of absorbing material. The absence of significant changes of the Raman spectra indicate that the structure of the crystal is not damaged *i.e.*, the exfoliation procedure does not damage the nanosheets and there is not an increasing number of physical defects occurring as the crystal thickness is reduced.

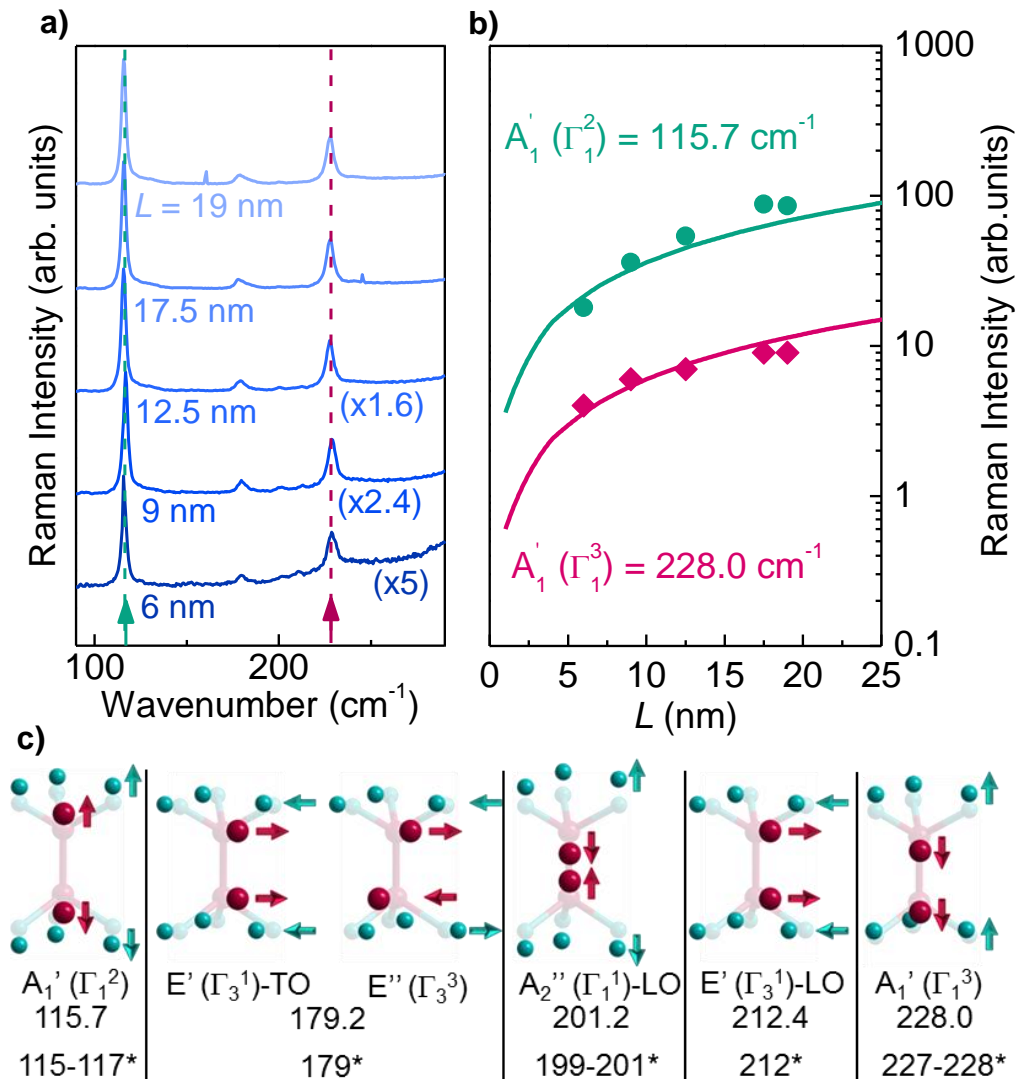


**Figure 4.7.** **a)** Normalised Raman spectra for nanosheets of thickness  $L = 6$ - $19$  nm. **b)** Dependence of the normalised Raman intensity for the  $A_1'(\Gamma_1^2)$  and  $A_1'(\Gamma_1^3)$  modes on the layer thickness at  $115.7$  (circles) and  $228.0 \text{ cm}^{-1}$  (diamonds), respectively; ( $\lambda = 633 \text{ nm}$  and  $P < 0.1 \text{ mW}$ ). **c)** Vibrational modes in bulk and few-layer  $\gamma$ -InSe from this work and from ref. [139]\*.

## 4.6 Tunable optical absorption

InSe devices intended for photocurrent spectroscopy measurements were fabricated from as-grown crystals and exfoliated nanosheets deposited on  $300 \text{ nm SiO}_2/\text{Si}$  substrates. The contact geometry consisted of two-terminal Au/Ti contacts that were deposited using a standard EBL method. In the absence of light, both the InSe

as-grown crystal and exfoliated samples were found to be highly resistive at room temperature with resistivity values of  $\rho > 10 \text{ } \Omega\text{cm}$ . Figure 4.8 shows the room temperature photocurrent spectrum for an  $L = 10 \text{ nm}$  (solid) and  $75 \text{ nm}$  (dotted) exfoliated nanosheet and also for an as-grown crystal (dashed). As detailed in Section 3.5.2, photocurrent was generated in the devices through illumination by a mechanically chopped, quartz halogen lamp and monochromator set-up with a power density of  $P_d \sim 10^{-3} \text{ Wcm}^{-2}$ . The absorption spectrum for the  $L = 10 \text{ nm}$  device shows an absorption edge located above photon energies of  $h\nu \sim 1.4 \text{ eV}$ . The spectrum appears to be blue-shifted in energy in comparison to the as-grown and bulk-like exfoliated layer by  $\sim 200 \text{ meV}$  which is consistent with the 2D carrier confinement observed in the PL measurements.

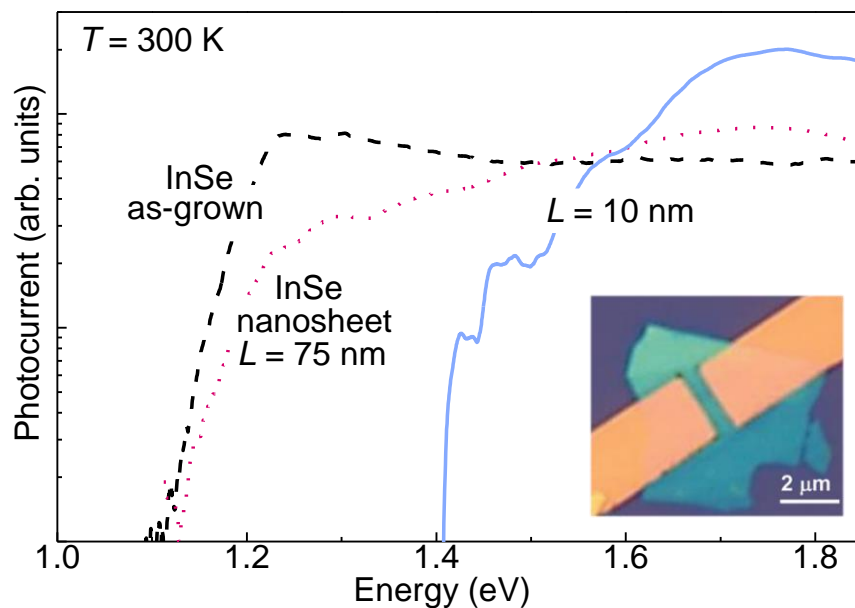


**Figure 4.8.** Room temperature photocurrent spectra for planar metal-InSe devices for as-grown InSe crystals (dashed line),  $L = 75 \text{ nm}$  (dotted line) and  $L = 10 \text{ nm}$  (solid line) exfoliated nanosheets. Photocurrent generated through optical illumination from a quartz halogen lamp and monochromator with power density  $P_d \sim 10^{-3} \text{ Wcm}^{-2}$ .

## 4.7 Summary

Room temperature photoluminescence emission from mechanically exfoliated nanosheets of InSe has been demonstrated. The PL emission energy, spectral linewidth and signal intensity are all observed to have a dependence on the crystal thickness. Due to increasing confinement of the charge carriers along the *c*-axis, the PL emission energy can be tuned by the crystal thickness. A PL energy blue-shift of over 600 meV was revealed from a systematic comparison of crystals ranging from as-grown ingots to  $L \sim 1.7$  nm nanosheets. AFM scans and comparison of the PL spectral linewidth with a statistical roughness model indicate that the exfoliated crystals are atomically flat with a surface roughness of approximately 1 monolayer ( $L = 0.832$  nm), to which charge carriers become increasingly sensitive upon a reduction in crystal thickness. The PL signal intensity was observed to systematically decrease with the number of layers in the nanosheet. A strong reduction in the luminescence was observed in the thinnest measured nanosheets, highlighting that reducing the crystal thickness induces a direct-to-indirect band gap crossover, as supported by DFT-calculations of the electronic band structure.

Room temperature Raman spectroscopy did not reveal a shift in the peak wavenumber positions from the thinnest measured nanosheets and indicates that the  $\gamma$ -phase is preserved from the as-grown crystal. A close agreement between the measured data and model of the Raman intensity with decreasing crystal thickness provided evidence that thinner nanosheets do not contain a greater concentration of physical defects than in the thicker samples.

Demonstration of a strong radiative recombination, stable emission at room temperature under ambient conditions, a tunable band gap by control of the crystal thickness, and photosensitive detection, identify ultrathin layers of semiconducting InSe as a promising candidate for nanoscale optoelectronics. Furthermore, a low

#### Chapter 4: Tuning the band gap of InSe by quantum confinement

concentration of dangling bonds and an atomically flat surface make InSe suitable for combination with graphene and other 2D crystals in the fabrication of vdW heterostructures. Properties sought after by such devices could take advantage of the absorption and/or emission capabilities of InSe nanolayers, which extend between the visible-to-near infrared (VIS-to-NIR) regions ( $\sim 0.65 - 1.0 \mu\text{m}$ ) of the electromagnetic spectrum.

## Chapter 5

### Acceptor and donor states within InSe nanosheets

The following chapter presents a temperature-dependent photoluminescence investigation into the radiative recombination from acceptor and donor states in  $\gamma$ -InSe nanosheets. The exfoliated crystals were housed within a cold-finger optical cryostat and probed by micro-photoluminescence ( $\mu$ PL). Topographical images were obtained by atomic force microscopy (AFM) scans. Experimental details are provided in Section 3.3.2 and results of this investigation were published in *Applied Physics Letters*, **105**, 221909 (2014).

#### 5.1 Introduction

In general, there are many factors contributing to the observed differences between PL spectra from semiconducting systems at room temperature ( $T \sim 300$  K) and liquid He temperatures ( $T \sim 4.2$  K). At room temperature ( $RT$ ), photogenerated charge carriers possess sufficient thermal energy to escape to higher energy levels and non-radiative recombination centres. While at low temperatures ( $LT$ ), carriers are effectively frozen-out and experience a reduced exciton (electron) – phonon interaction. The recombination processes most frequently observed in PL spectra are associated with the lowest energy states, as the timescale of radiative recombination of carriers is much slower ( $\sim 10^{-9}$ s) than that associated to carrier relaxation ( $\sim 10^{-12}$ s).<sup>215</sup> Consequently, PL spectra at  $LT$  tend to be dominated by strong, sharp luminescence emission due to carrier recombination from states associated with impurities and defects within the crystal, often located within the band gap. With increasing temperature, the effects of carrier thermalisation to non-radiative states and an enhancement of

the efficiency of transitions requiring the absorption of phonons, leads to a significant loss in the luminescence intensity and broadening of the optical linewidth due to the overlapping of bands with close energies. Any emission that is observed at  $RT$  tends to originate from the most efficient states *i.e.*, in a direct band gap semiconductor, the PL dominant emission is usually associated with the band-to-band transition and related free excitonic state. Increasing temperature also usually acts to decrease the band gap energy.<sup>216</sup> The mean square displacement of lattice atoms from equilibrium (*i.e.*, interatomic distance) is increased with temperature and acts to weaken the ionic potential experienced by charge carriers within the crystal, which reduces the band gap energy.<sup>106,216–218</sup> By taking these factors into account, a comprehensive comparison of temperature-dependent  $\mu$ PL spectra can prove valuable when investigating shallow impurities within novel semiconducting crystals, such as InSe, and provides understanding of how the effects of dopant atoms and defects could affect future technological developments. Charge carrier localisation on strongly confined dopant states may degrade the carrier mobility in nanoscale FETs,<sup>149,150,154,219</sup> while the capture and release of carriers at trap-like impurity states could increase noise levels, produce slow optical temporal responses and broaden emission lines. Such effects are detrimental to the full exploitation of InSe in the prototype optoelectronic devices, such as photodetectors and LEDs.<sup>67,85,141,158,159</sup> In this chapter, I demonstrate that at  $LT$ , photogenerated charge carriers in InSe nanosheets are bound to unintentional donor and acceptor states, with binding energies that increase significantly when the nanosheet thickness is reduced to a few nanometres.

## 5.2 Photoluminescence at $T = 8$ K and $T = 300$ K

The PL spectra of exfoliated InSe nanosheets ( $L = 7 - 20$  nm) at  $RT$  and  $LT$  are shown in Figure 5.1. Experimental details are given in Section 3.3.2 and  $RT$  and  $LT$  refer to the temperature of the liquid-He

cooled cold-finger sample holder, which is in thermal contact with the sample. Comparison of the spectra shows that, for a reduction in crystal thickness, both series of spectra shift to higher energies and broaden. For the thinnest nanosheets (*i.e.*,  $L = 7$  and  $10$  nm), the position of the main PL band is only weakly affected by temperature. For the thicker nanosheets (*i.e.*,  $L = 16$  and  $20$  nm) the energy blue-shift at  $LT$  is more pronounced.

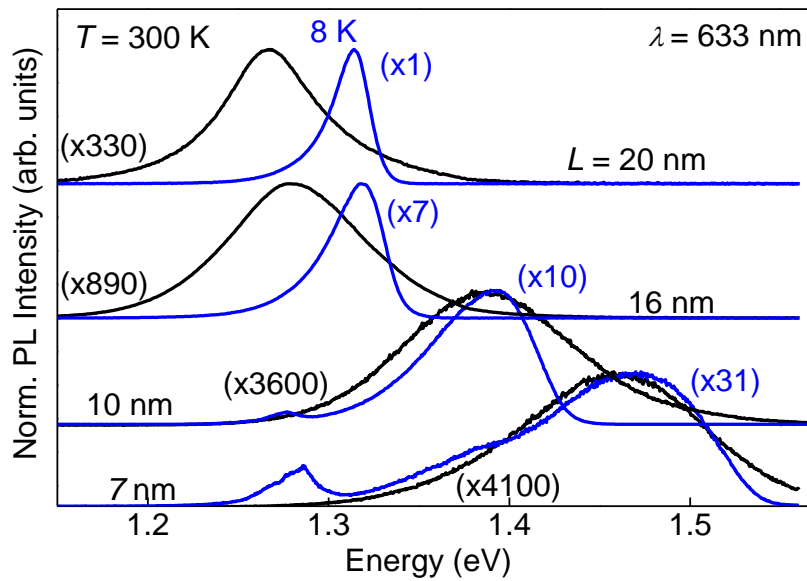


**Figure 5.1.** Normalised PL spectra of  $\gamma$ -InSe nanosheets with thickness  $L = 7, 10, 16$  and  $20$  nm at  $T = 8$  K (blue) and  $T = 300$  K (black) ( $P < 0.1$  mW and  $\lambda = 633$  nm).

The dependence of the PL emission on both temperature and thickness seems to be a product of competing processes, namely, the effect of temperature on the band gap energy and the effects of quantum confinement on both the band gap and the binding energies of the native dopants in the InSe nanosheets. In bulk InSe, the band gap at  $T = 0$  K is  $E_g(0 \text{ K}) = 1.3525$  eV, and monotonically reduces with increasing temperature to a value of  $E_g(300 \text{ K}) = 1.2635$  eV (as determined by optical absorption measurements).<sup>106</sup> The temperature-dependence of the band gap energy can be calculated by Varshni's relation<sup>220</sup>

$$E_g(T) = E_g(0) - \frac{\alpha T^2}{(T + \beta)}, \quad (5.1)$$

where  $\alpha = 0.76 \text{ meV K}^{-1}$  and  $\beta = 480 \text{ K}$  are the thermal coefficients for bulk  $\gamma$ -InSe.<sup>221</sup>

For the case of thin InSe nanosheets, the dependence of  $E_g$  on  $L$  is described using an infinite-height square quantum well model, due to the quantum confinement of carriers along the  $c$ -axis *i.e.*,

$$E_{gL}(0) = E_g(0) + \frac{\pi^2 \hbar^2}{2L^2 \mu_c} \quad (5.2)$$

where  $\mu_c = (1/m_e^* + 1/m_h^*)^{-1} = 0.054m_0$  is the exciton reduced mass as defined for Equation 4.1.  $E_{gL}(LT)$  can therefore be individually calculated for each nanosheet thickness. Considering only band-to-band transitions and Equation 5.2, the  $LT$  PL emission energies shown in Figure 5.1 should lie at energies exceeding 1.3525 eV. This is not the case for nanosheets of thickness  $L = 16$  and 20 nm and highlights the presence of an alternative mechanism *i.e.*, recombination from impurity states.

### 5.3 Temperature-dependent photoluminescence

Figure 5.2 presents a series of temperature-dependent PL spectra ( $T \sim 10 - 300 \text{ K}$ ) for nanosheets with  $L = 7, 10$  and 20 nm. Varshni's empirical model predicts a monotonic decrease of the band gap energy with increasing  $T$ ;<sup>220</sup> however, the temperature-dependence of the main peak PL emission appears to be more complex, following an S-shaped trend associated with the presence of impurity states. With increasing temperature, the gradual unbinding of carriers from shallow mid-gap impurity states to near band-to-band transitions, can cause a blue-shift in emission energy which compensates the expected monotonic red-shift predicted by Varshni's empirical model.

A straightforward conjecture is to assume the presence of hydrogenic impurities in the form of acceptors and donors within the crystal. The three-dimensional binding energy,  $E_b^*$ , and Bohr radius,  $a^*$ , of the dopant states are calculated using the hydrogenic model,

$$E_b^* = \frac{1}{2} m^* e^4 \frac{1}{(4\pi\epsilon_0\epsilon_\infty\hbar)^2} \quad (5.3)$$

and

$$a^* = \frac{4\pi\epsilon_0\epsilon_\infty\hbar^2}{e^2 m^*} \quad (5.4)$$

where  $m^*$  represents the respective carrier effective mass listed in Table 5.1 and  $\epsilon_\infty = 7$  is the relative dielectric constant of  $\gamma$ -InSe.<sup>121</sup>

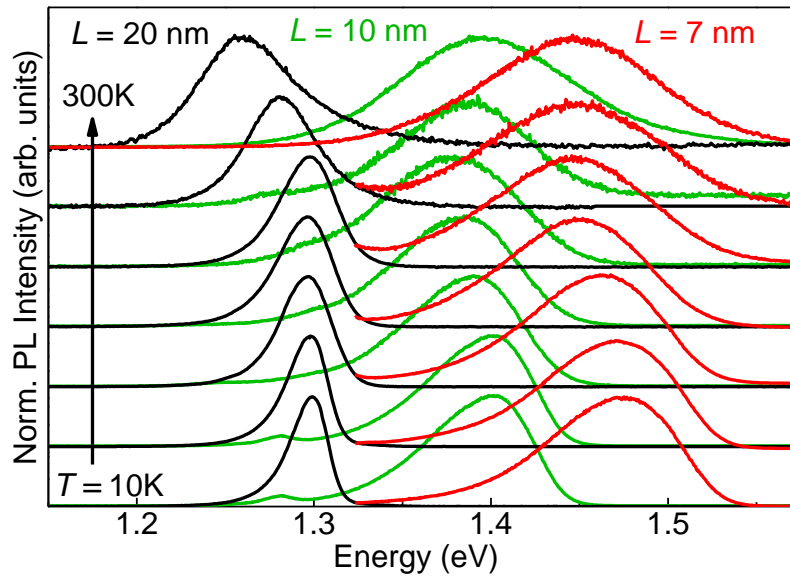


**Figure 5.2.** Normalised PL emission spectra in the range  $T \sim 10 - 300$  K for nanosheets with  $L = 7$  nm (red), 10 nm (green) and 20 nm (black) ( $P < 1$  mW,  $\lambda = 633$  nm).

For bulk InSe, the binding energies (Bohr radii) for the donor and acceptor states are  $E_D = 22$  meV ( $a_D = 4.7$  nm) and  $E_A = 47$  meV ( $a_A = 2.2$  nm), respectively. Previous works in the literature suggest the presence of both donors and acceptors within bulk InSe, with binding energies of  $\sim 20$  meV<sup>222–224</sup> and 40 – 65 meV,<sup>225,226</sup> respectively. The

binding energies of these dopant impurities are also subject to quantum confinement when quantum well structures are formed, due to the compression of the carrier wavefunction along the  $c$ -axis.<sup>227</sup> The dopant binding energy increases as the carrier is kept close to the attractive centre by the walls of the quantum well and experiences a larger potential than in the absence of a quantum well. Such an effect can explain the weak temperature dependence of the main PL band as shown for the  $L = 7$  and 10 nm nanosheets in Figure 5.1.

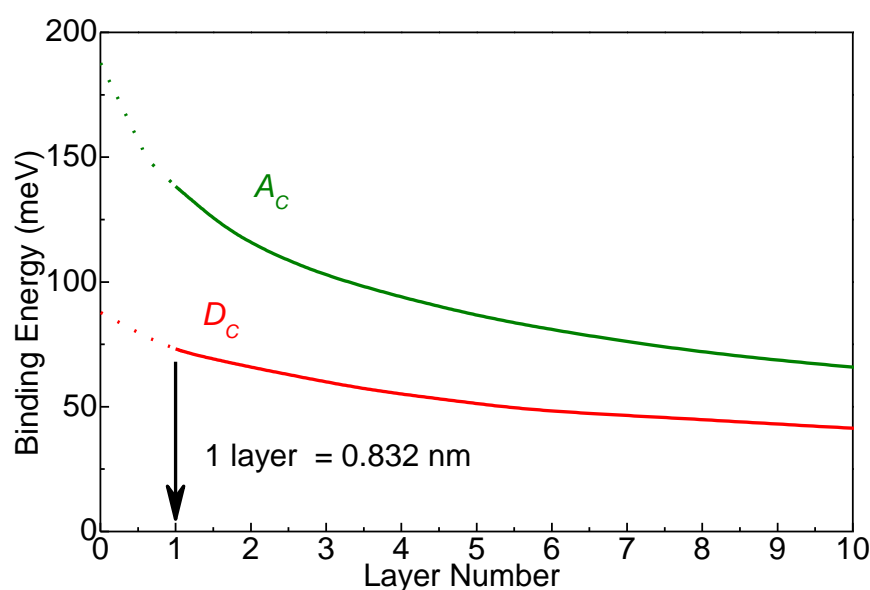


**Figure 5.3.** Calculated binding energy of a donor ( $D_c$ ) and acceptor ( $A_c$ ) in the limit of small  $L$  ( $<10$  layers).<sup>227,228</sup> The vertical arrow shows the limit for a single layer of InSe ( $L = 0.832$  nm).

The dependence of the dopant binding energy on nanosheet layer number can be modelled using a 2D hydrogenic model of impurity states in a quantum well (Figure 5.3).<sup>227,228</sup> The model also predicts a spreading of the dopant binding energy levels, due to a positional dependence of the impurities with respect to the walls of the quantum well. Considering donors and acceptors located in the central plane of the well, the binding energy increases monotonically with a decrease in nanosheet thickness. In particular, the binding energy reaches four times the bulk value as the crystal thickness is reduced to the 2D limit.<sup>227,228</sup> Using the parameters for InSe, the binding energy for the

acceptor and donor would reach  $4E_D = 88$  meV and  $4E_A = 188$  meV; for a single InSe layer, these energies reduce to 74 meV and 138 meV, respectively. For impurities located off-centre ( $D_E$  and  $A_E$ ), the binding energy reaches a minimum of  $E_{A/D}^{3D}/4$  at the well boundary and only exceed  $E_{A/D}^{3D}$  after the nanosheet is reduced below a critical layer thickness.<sup>228</sup> Taking this model into account, with a decrease in nanosheet layer number, the calculated binding energies tend to increase due to quantum confinement and spread in energy due to the dopant position.

**Table 5.1.** Electron ( $m_e^*$ ) and hole ( $m_h^*$ ) effective masses along the  $c$ -axis ( $\parallel c$ ), band gap ( $E_g$ ) at  $T = 0$  K and 300 K, thermal coefficients and relative dielectric constant ( $\epsilon_\infty$ ) for  $\gamma$ -InSe. Reproduced with permission from: ref. [121], © (2010), American Physical Society; ref. [95], © (1978), American Physical Society and ref. [221], © (1999), IOP Publishing.

$m_e^*$	$m_h^*$	$E_g(0\text{ K})$	$E_g(300\text{ K})$	$\alpha$	$\beta$	$\epsilon_\infty$
( $m_0$ )	( $m_0$ )	(eV)	(eV)	(meV K <sup>-1</sup> )	(K)	
0.081	0.17	1.3525	1.2635	0.76	480	7.0
ref.[121]	[121]	[95]	[95]	[221]	[221]	[121]

## 5.4 Donor and acceptor binding energies

In order to understand the origin of the PL emission at  $LT$ , the dependence of the peak emission energy,  $h\nu$ , (see Figure 5.4) on temperature is compared to the calculated dependencies for the exciton ( $X$ ), free electron to neutral-acceptor ( $e-A$ ), free hole to neutral-donor ( $h-D$ ) and donor-acceptor ( $D-A$ ) transitions for a nanosheet with  $L = 20$  nm. Varshni's model is used to calculate the temperature-dependence of the transition energies, where  $E_{gL}(0)$  can be replaced with the low temperature exciton recombination energy in bulk  $\gamma$ -InSe ( $E_x = 1.338$  eV) or the calculated donor and acceptor energies for the  $e-A$ ,  $h-D$  and  $D-A$  transitions ( $E_{e-A} = 1.306$  eV,  $E_{h-D} = 1.331$  eV and  $E_{D-A} = 1.284$  eV, respectively). The dopants responsible for the donor

and acceptor-related recombination in the nominally undoped  $\gamma$ -InSe nanosheets are likely to originate from an excess of In-atoms (<1%) and N-substitutional impurities (<3%) that are detected in our EDX experiments.<sup>124</sup> N-substitutional atoms on Se-sites behave as acceptors<sup>229</sup> and an excess of In can lead to the formation of In-interstitial atoms,<sup>223</sup> which are known to behave as shallow donors and produce  $n$ -type conductivity in  $\gamma$ -InSe.<sup>225,229,230</sup>

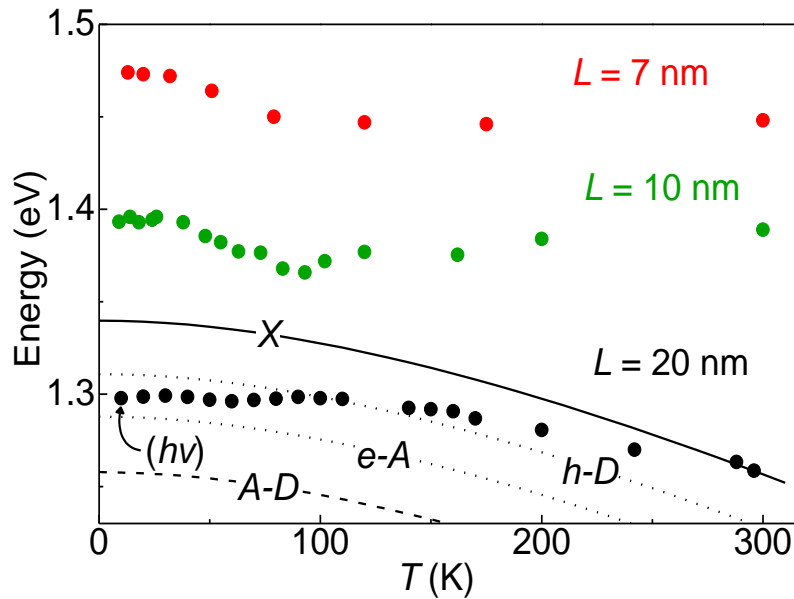


**Figure 5.4.** PL peak energy dependence on temperature (symbols) for  $L = 7$ , 10 and 20 nm. Lines represent the calculated temperature dependence for the free exciton ( $X$ ), acceptor-band ( $e-A$ ), donor-band ( $h-D$ ), and donor-acceptor ( $D-A$ ) transitions for  $L = 20$  nm. The calculated curves are for dopant atoms positioned in the centre of the well.

The spectral broadening restricts the calculation of the binding energies for individual donor and acceptor states from the PL spectra. Instead, an effective binding energy,  $\Delta E$ , is estimated from the energy difference between the lowest temperature values of the peak PL emission,  $h\nu$ , and the band gap energy,  $E_{gL}$ , as derived from Varshni's model and the assumption that  $E_{gL} = h\nu$  at  $T = 300$  K. The hydrogenic model for impurities in a quantum well is used to plot the  $L$ -dependence of the binding energies of the donor, acceptor, and donor-acceptor complex transitions in  $\gamma$ -InSe, assumed to be located in the centre of the quantum well ( $D_C$ ,  $A_C$  and  $D_C-A_C$ , respectively).

Additionally, the off-centre donor to on-centre acceptor ( $D_E-A_C$ ) is included to demonstrate the spread in energies that occurs in these states due to the positional dependence of the binding energy introduced in the hydrogenic model.<sup>227,228</sup> The calculated energies for the  $D_C$ ,  $A_C$  and  $D_{C/E}A_C$  states generally reproduce the increase of  $\Delta E$  with decreasing crystal thickness (Figure 5.5).

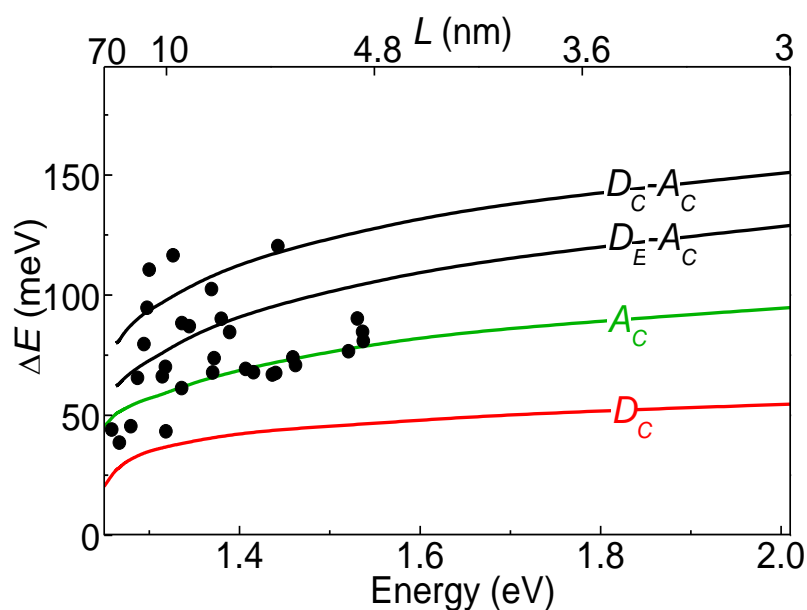


**Figure 5.5.** Calculated dependence of the binding energy of a donor ( $D_C$ ), acceptor ( $A_C$ ) and donor-acceptor pairs ( $D_C-A_C$  and  $D_E-A_C$ ) on the estimated thickness  $L^*$  (top axis) and on the band gap energy at  $T = 300$  K (bottom axis) of the InSe nanosheets. The subscripts  $C/E$  refer to dopants at the centre or boundary edge of the well. The data points estimate the thickness dependence of the binding energies, deduced from an analysis of the  $RT$  PL data.

The scatter in the data is consistent with the assumption that the PL arises from the recombination of carriers at acceptors and donors located in different positions within the nanosheet. Further scatter in the PL emission energy may originate from modulations of the Coulomb landscape due to, for example, charged impurity pairs or impurity clustering.

### 5.5 Thermal quenching of luminescence intensity

At  $LT$ , the normalised integrated PL intensity follows a similar dependence on the crystal thickness as observed at  $RT$  (Figure 5.6),

showing a sharp loss in luminescence intensity for the thinnest nanosheet, which was attributed to a direct-to-indirect crossover in Section 4.4. A decrease in the luminescence efficiency in InSe could also be expected from the presence of stacking faults,[209] crystal defects and dopant impurities which, along with the roughness ( $\pm 1$  monolayer) of thin InSe nanosheets, can all cause a lower recombination rate and induce a preferential recombination of carriers from localized states. Additionally, reducing the nanosheet thickness increases the surface-to-volume ratio which may cause an enhancement of carrier interaction with non-radiative surface states.<sup>17</sup>

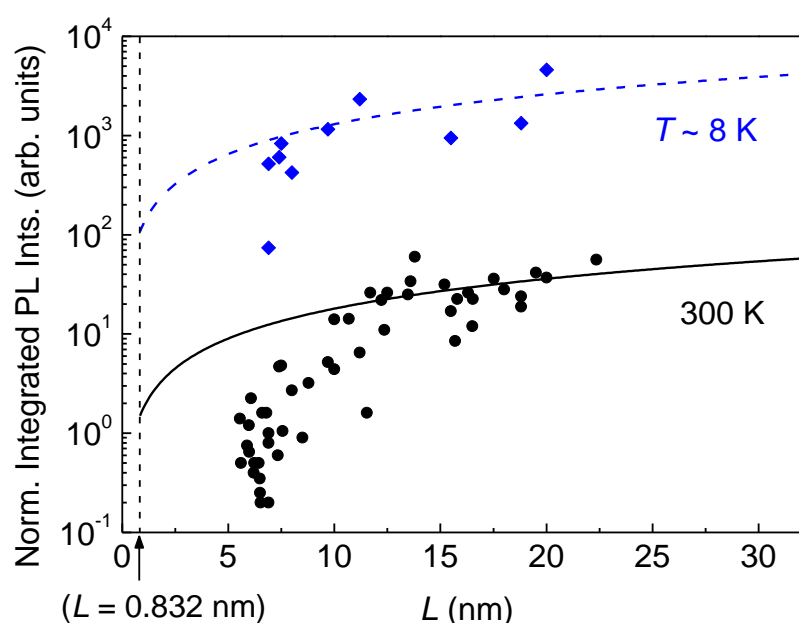


**Figure 5.6.** Normalised PL integrated intensity for nanosheets with decreasing layer thickness at room temperature (circles) and low temperature (diamonds). The lines estimate the PL emission based on equation 4.4. at room temperature (solid) and low temperature (dashed) and  $\lambda = 633$  nm.

In order to probe the effects of extrinsic defects on the optical luminescence efficiency, temperature-dependent PL spectra were compared for two nanosheets of thickness  $L = 15$  nm (sheet A) and  $L = 10$  nm (sheet B), as shown in Figure 5.7. If the surface-to-volume ratio were playing a significant role in the enhancement of non-radiative carrier loss and thus a reduction in the luminescence intensity, then it could be expected that the thinner of the two nanosheets (B) would

experience a stronger thermal quenching of the luminescence intensity. However, no stronger thermal quenching was observed (see Figure 5.7b). The overall temperature dependence for both nanosheets is very similar, corresponding to a decrease of around  $\sim 10^3$  as  $T$  approaches  $RT$ , supporting the conclusion that the luminescence quench associated with reducing the crystal thickness is likely to be a result of the direct-to-indirect band gap crossover.

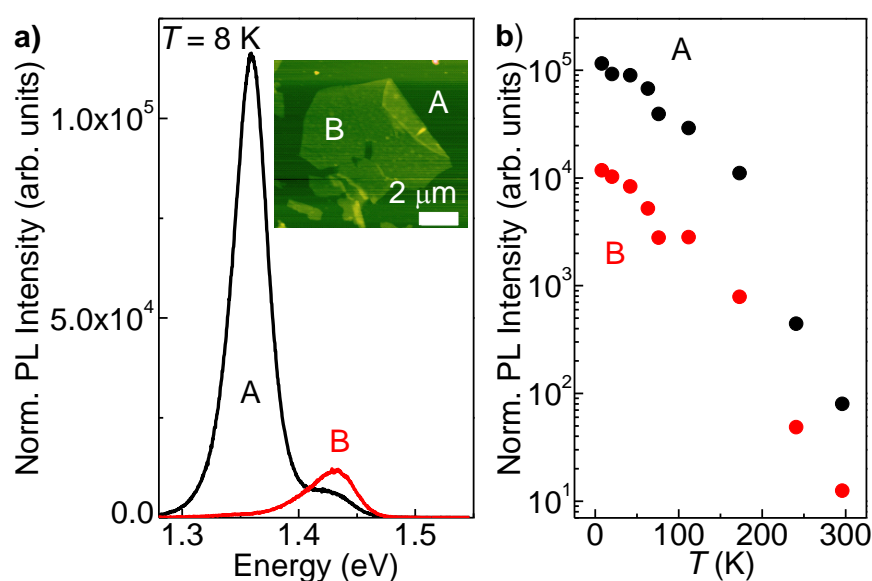


**Figure 5.7.** **a)** PL spectra for nanosheets A and B at  $T = 8$  K and corresponding AFM image (inset). **b)** Temperature dependence for the normalised PL intensity for nanosheets A and B ( $P < 1$  mW,  $\lambda = 633$  nm).

## 5.6 Summary

Comparison of temperature-dependent PL spectra reveals that the optical emission from InSe nanosheets at low temperature is dominated by recombination of photoexcited carriers bound at native donors and acceptors. The binding energies of the impurity states are sensitive to the dopant position within the nanolayer and increase significantly following a reduction in the crystal thickness. Information regarding the effects of unintentional or intentional dopants on vdW crystal properties is relevant to the design and fabrication of nano-optical and electronic devices whose performance could be degraded

by carrier localisation on strongly confined dopant states. Of particular interest, is the possibility of observing a Lifshitz transition associated with the sombrero shaped form of the valence band when the InSe nanosheet thickness is reduced to a few nanometres.<sup>231</sup> The application of large transverse electric fields ( $0.2-0.3 \text{ Vnm}^{-1}$ )<sup>65</sup> or presence of sufficiently high acceptor densities ( $p \sim 6 \times 10^{13} \text{ cm}^{-2}$ )<sup>231</sup> could satisfy the requirements to experimentally attain an insulator-to-metal transition in  $p$ -InSe.

## Chapter 6

### Magneto-photoluminescence studies of exfoliated InSe

This chapter presents the results of a spatially-resolved magneto-photoluminescence investigation of exfoliated  $\gamma$ -InSe. The magneto-optical properties of the exfoliated sheets were probed by micro-photoluminescence ( $\mu$ PL) within the bore of a resistive magnet in the Faraday configuration; further details are found in Section 3.3.3. The initial preparation of InSe samples for the magneto-optical studies were undertaken at the Laboratoire National des Champs Magnétiques Intenses (LNCMI) in Grenoble by Dr. K. Nogajewski and Dr. M. Molas. The magneto-photoluminescence investigation was performed by Dr. M. Molas and myself at the LNCMI and the density functional theory (DFT) calculations of the band structure were provided by the group of Prof. V. Falko of the National Graphene Institute, The University of Manchester.

#### 6.1 Introduction

In addition to size-induced quantum mechanical effects, the application of an external electric and/or magnetic field provides a method of controllably changing the electronic band structure of van der Waals layered crystals. As introduced in the previous chapters, metal monochalcogenides, such as InSe and GaSe, undergo a direct-to-indirect transition as the number of layers is decreased below a critical value. One well-established technique to probe the band structure relies on using magnetic fields to further confine charge carriers and quantize the electronic motion into Landau levels (LLs). In this chapter we show that a magnetic field,  $B$ , applied perpendicular to the plane of InSe nanosheets induces a marked change of the measured optical spectrum, with a transfer of intensity from a low-to-

high energy component at high  $B$ , corresponding to an indirect-to-direct band gap crossover. We propose that the induced transition arises from the Landau quantization of the carrier motion and crossover between hole cyclotron orbits centred on closed edges of the valence band, which in metal monochalcogenides takes the form of the aforementioned ‘Mexican hat’.

## 6.2 Valence band of InSe nanosheets

As shown in Figure 6.1a, the layer-dependent energy shift of the band gap of InSe, as measured by  $RT$   $\mu$ PL and calculated from an effective mass (EM) approximation (Equation 4.1), is closely reproduced by DFT calculations. The resulting DFT-calculated band structure is shown in Figure 6.1b, which focuses on a narrow range of  $k$ -values in  $k$ -space, from the  $\Gamma$ -point towards the K-point, and energy, from the conduction band minimum (CBM) at  $\Gamma$  to the valence band maximum (VBM) along  $\Gamma$ -K and valence band edge at  $\Gamma$  ( $VBE_{\Gamma}$ ).

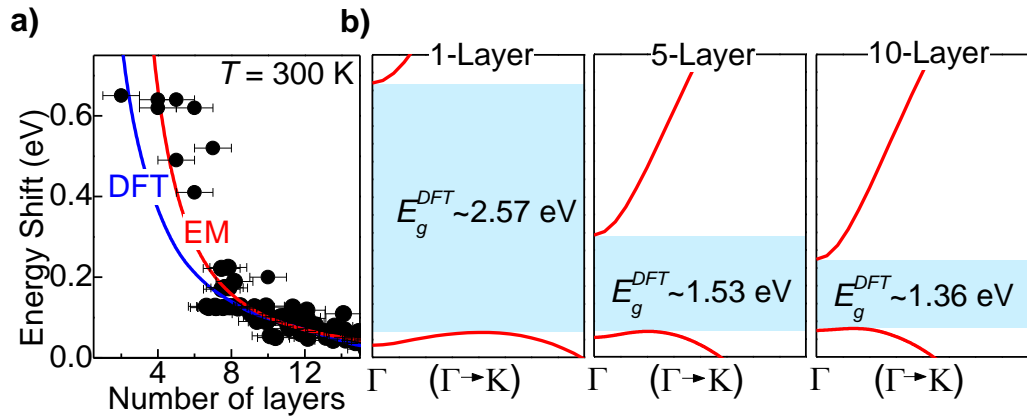


**Figure 6.1.** **a)** Calculated (lines) and measured (symbols) energy shift of the band gap of InSe versus number of layers. The calculated energy shift is derived from DFT calculations (blue line) and from a square quantum well potential of infinite height in the effective mass (EM) approximation (Equation 4.1). The measured values of the PL energy shift and thickness were obtained from  $\mu$ PL and AFM, respectively ( $T = 300$  K). **b)** Calculated band structure for 1, 5 and 10 layers of InSe over a narrow range in energy and  $k$ -space from  $\Gamma$  towards K (1-Layer = 0.832 nm).

The CBM remains positioned at  $\Gamma$  and undergoes a shift to higher energies with decreasing nanosheet thickness. The shift is accompanied by the emergence of a ‘Mexican hat’ feature in the valence band, as the VBM shifts along  $\Gamma$ -K while a minimum develops at  $\Gamma$ . Consequently, holes can occupy states away from  $\Gamma$ , which partially accounts for the quenching of the PL observed from the thinnest nanosheets associated with the direct-to-indirect crossover.

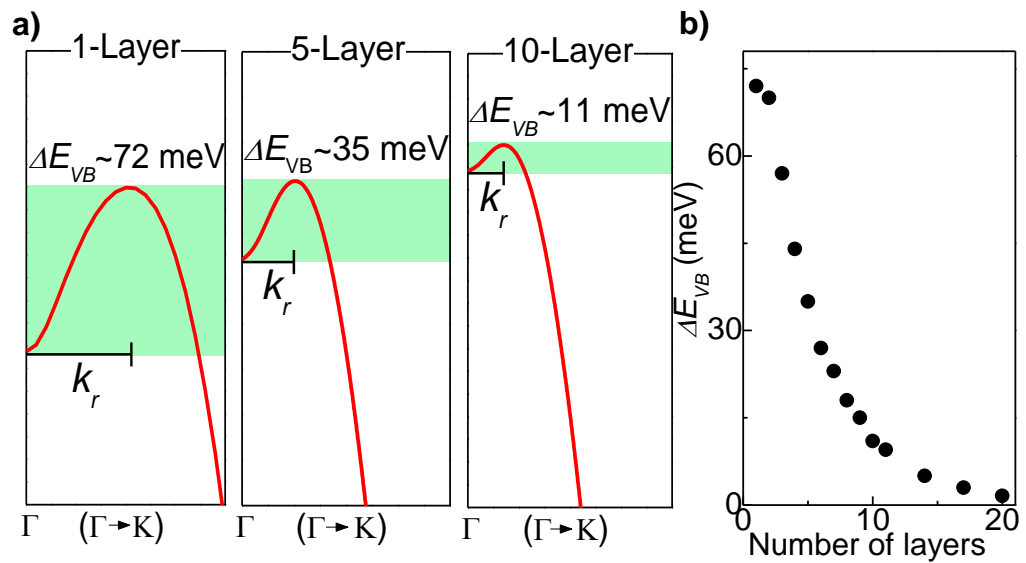


**Figure 6.2.** **a)** Calculated valence band structure for 1, 5 and 10 layer InSe over a narrow range in energy and  $k$ -space from  $\Gamma$  towards K.  $\Delta E_{VB}$  and  $k_r$  represent the VBM and VBE $_{\Gamma}$  separation in energy and  $k$ -space, respectively. **b)** Calculated energy difference between the VBM and VBE $_{\Gamma}$  ( $\Delta E_{VB}$ ) for 1 to 20 layer InSe.

Figure 6.2a focusses on the valence band structure at  $\Gamma$  and along  $\Gamma$ -K for 1, 5 and 10 layer InSe. The calculated separation between the VBM and VBE $_{\Gamma}$  in  $k$ -space ( $k_r$ ) and energy ( $\Delta E_{VB}$ ), changes gradually with InSe layer number, inferring the direct-to-indirect crossover occurs progressively, rather than abruptly. With decreasing layer number,  $k_r$  shifts from 0% to around 30% of the Brillouin zone along  $\Gamma$ -K ( $k_r \sim 3$  nm $^{-1}$  for a monolayer) and  $\Delta E_{VB}$  increases from 0 to around 0.07 eV (Figure 6.2b). Due to the small  $\Delta E_{VB}$  and broad PL linewidth observed in the thinnest InSe nanosheets

(Figure 6.3), a PL experiment alone would not be able to distinguish between direct and indirect optical transitions that are close in energy and have different oscillator strengths. However, the presence of a strong applied magnetic field can act to quantize the charge carrier motion into Landau levels (LLs) and modify the oscillator strengths of the corresponding interband LL transitions, detectable through a change in the PL lineshape with increasing  $B$ .

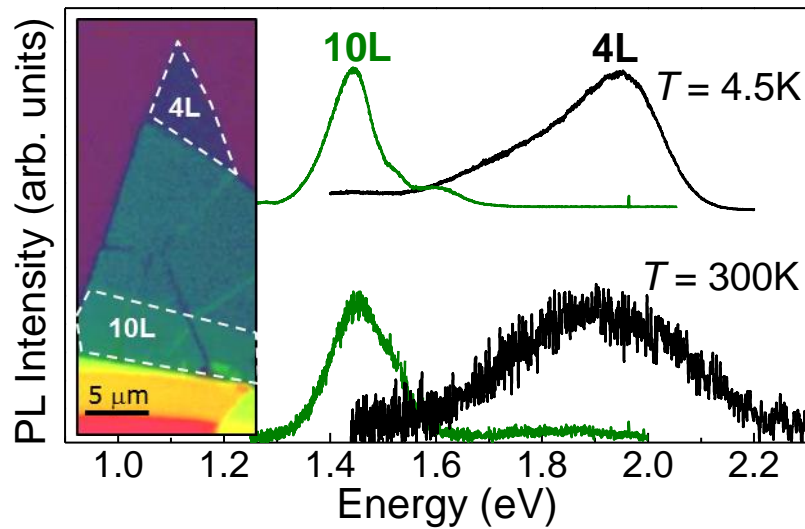
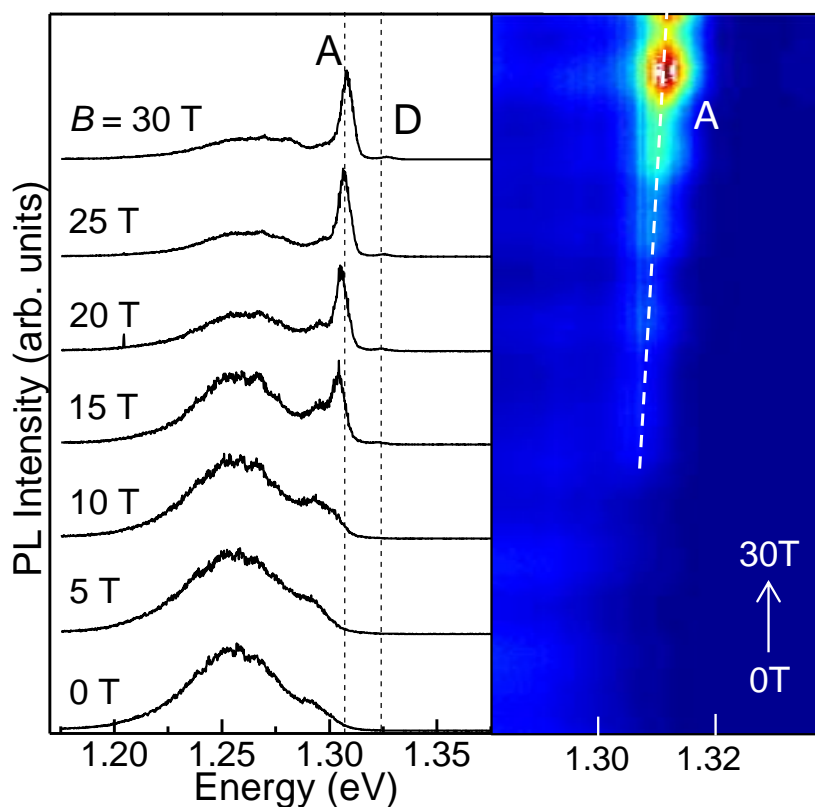


**Figure 6.3.** Normalised  $\mu$ PL spectra of  $\gamma$ -InSe nanosheets with 4 and 10 layers at  $T = 4.5$  K and 300 K for  $\lambda = 532$  nm. The inset is an optical image of the nanosheets.

### 6.3 Magneto-photoluminescence studies on exfoliated InSe

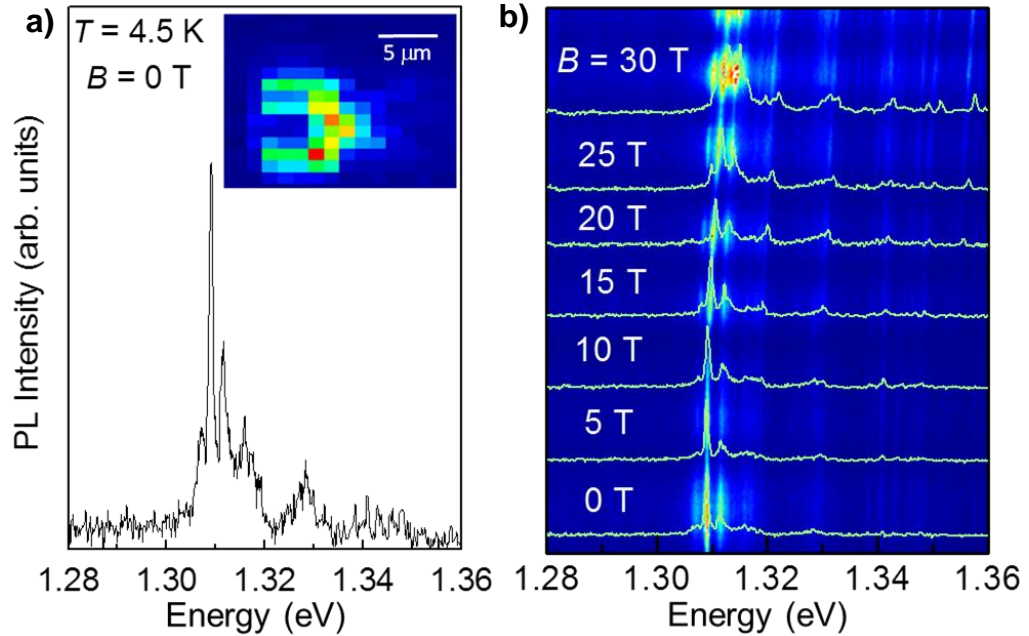
The magnetic field dependence of the  $\mu$ PL spectra for bulk exfoliated InSe ( $L > 20$  nm) at  $T = 4.5$  K is shown in Figure 6.4. As detailed in Chapter 5 (for  $B = 0$  T) the PL emission from InSe originates from carrier recombination from native donors (D), acceptors (A) and donor-acceptor pairs. As the magnetic field increases, the D and A related bands blue-shift. At  $B > 15$  T, the diamagnetic shift  $\delta E$  of the A-transition has a linear dependence on magnetic field of the form  $\delta E = \sigma_{\parallel} B$ , where  $\sigma_{\parallel} = (2.8 \pm 0.2) \times 10^{-4}$  eV/T is the diamagnetic

coefficient. A smaller diamagnetic shift is observed for the donor peak (D) for which  $\sigma_{//} = (2.5 \pm 0.2) \times 10^{-4}$  eV/T. These measured energy shifts are comparable to those calculated ( $\delta E = 4.5$  meV at  $B = 30$  T) and derived from optical absorption measurements ( $\delta E = 5.1$  meV at  $B = 30$  T) for the free exciton in bulk InSe.<sup>232</sup>



**Figure 6.4. Left:**  $\mu$ PL spectra at applied magnetic fields of  $B = 0 - 30$  T in the Faraday geometry and  $T = 4.5$  K for bulk InSe ( $L > 20$  nm). **Right:** A colour map of the  $\mu$ PL intensity versus magnetic field and photon energy. The diamagnetic shift of the band-to-acceptor (A) transition is represented by the dashed white line.

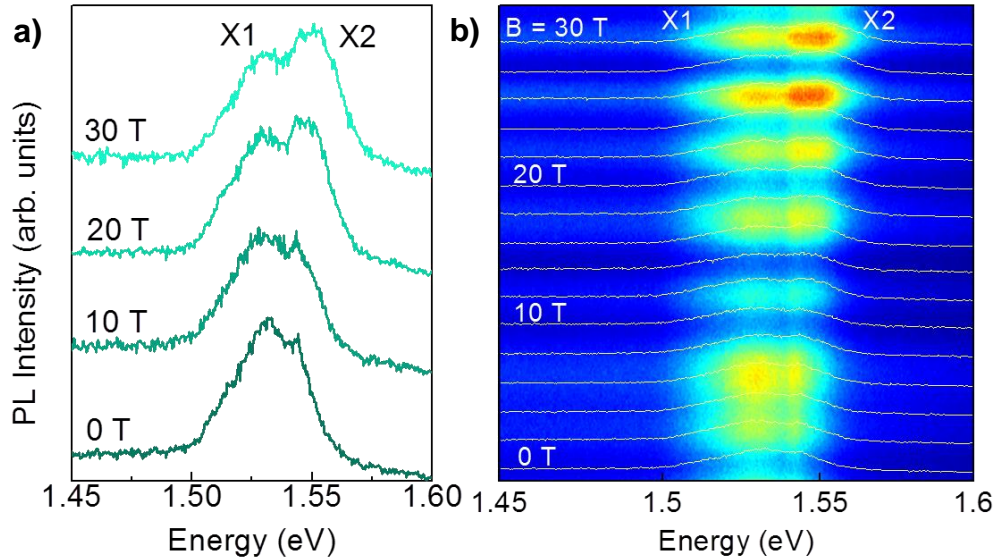
Additionally, narrow ( $\sim 0.5$  meV) and bright PL emission lines with a small diamagnetic shift ( $\sim 3 - 4$  meV at 30 T) are also observed across a range of bulk-like nanosheets (Figure 6.5) and suggest a spatial localisation of photoexcited carriers in the plane of the nanosheet and quantum-dot defect-like  $\mu$ PL emission similar to those reported in single layer metal dichalcogenides.<sup>233–236</sup>



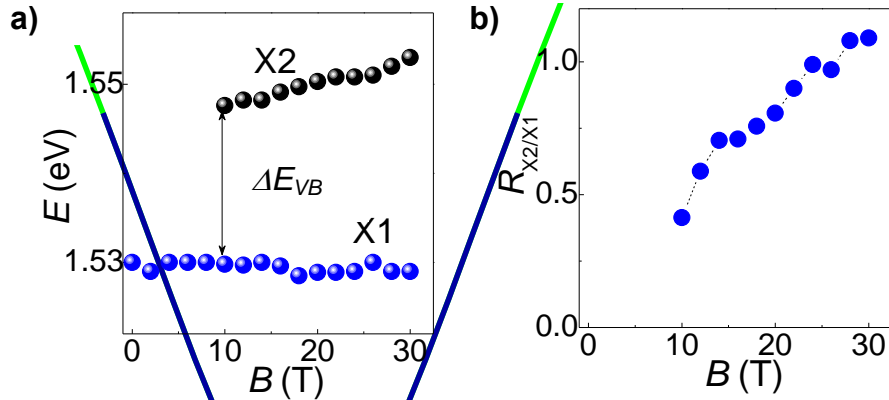
**Figure 6.5.** **a)**  $\mu$ PL spectrum at magnetic field  $B = 0$  T and  $T = 4.5$  K for bulk InSe. The inset shows a  $\mu$ PL map acquired at the energy of the  $\mu$ PL line at 1.309 eV. **b)** Colour map of the PL intensity versus magnetic field  $B$  and photon energy. The  $\mu$ PL spectra for representative  $B$  are overlapped on the colour map. The experiment was conducted in the Faraday geometry with the magnetic field applied parallel to the  $c$ -axis.

Figure 6.6a presents a series of  $\mu$ PL spectra at  $T = 4.2$  K for magnetic fields up to  $B = 30$  T for an InSe nanosheet of  $\sim 7$  layers. The spectra are overlapped over a colour plot of the intensity of the PL emission versus magnetic field and photon energy in Figure 6.6b. For  $B = 30$  T, the main PL band (X1) is centred at 1.53 eV, higher than in bulk InSe. With increasing  $B$ , a stronger PL emission band (X2) emerges at higher energy. Figure 6.7a shows the  $B$ -dependence of the energy positions of the X2 and X1 PL peaks and the corresponding ratio of intensities,  $R_{X2/X1}$ , as derived from fits to the PL spectra by two Gaussian lineshapes (Figure 6.7b). The relative intensity of the X1 and X2 bands changes with increasing  $B$  and appears to shift from the low energy (X1) to high energy peak (X2). Also, whereas the X1 band is weakly shifted in energy, the X2 band tends to blue-shift linearly with

increasing  $B$ . This  $B$ -dependence of the two bands has the characteristic form of a quantum mechanical admixing effect.



**Figure 6.6.** **a)**  $\mu$ PL spectra at magnetic field  $B = 0, 10, 20,$  and  $30$  T and  $T = 4.5$  K for an InSe flake with  $L \sim 7$  layers. **b)** The  $\mu$ PL spectra are overlapped over a colour map of the PL intensity versus  $B$  and photon energy.



**Figure 6.7.** **a)** Energy peak position of the X2 and X1  $\mu$ PL bands **b)** Ratio of intensity,  $R_{X2/X1}$ , for X1 and X2 versus  $B$ .

In order to understand the  $B$ -dependence of the  $\mu$ PL spectra of thin InSe sheets, we consider the quantisation of the hole and electron in-plane motion (Figure 6.8). When applied parallel to the  $c$ -axis, the magnetic field acts to quantise the motion of charge carriers in the  $xy$  plane into a series of LLs; in turn, this can change the oscillator

strength of the interband transitions. Near the edges of each band, the LL energy shift,  $E_n^{e(h)}$ , for electrons ( $e$ ) and holes ( $h$ ) can be approximated by

$$E_n^{e(h)} = \hbar\omega_c^{e(h)}\left(n + \frac{1}{2}\right), \quad (6.1)$$

where  $n$  is an integer and

$$\omega_c^{e(h)} = \frac{eB}{m_{\perp c}^{e(h)}} \quad (6.2)$$

is the cyclotron frequency and  $m_{\perp c}^{e(h)}$  is the electron (hole) in-plane cyclotron mass at the VBM ( $m_{hVB}$ ) and at  $\Gamma$  ( $m_{e\Gamma}$  and  $m_{h\Gamma}$ ). Table 6.1 shows the values of  $m_{e\Gamma}$ ,  $m_{h\Gamma}$  and  $m_{hVB}$  as derived from the DFT energy dispersion curves for bulk and 1, 2, 5 and 10 layer InSe. Compared to the parameters for bulk InSe,<sup>232</sup>  $m_{e\Gamma}$  tends to increase with decreasing nanosheet thickness, with values that are similar to the in-plane cyclotron mass in bulk InSe ( $m_{e\Gamma} = 0.138m_0$ );<sup>187</sup> for hole states at  $\Gamma$  and at the VBM, the hole masses have opposite sign, with absolute values that tend to be larger at the VBM than at  $\Gamma$  for thinner nanosheets.

**Table 6.1.** Values of the electron ( $m_{e\Gamma}$ ) and hole ( $m_{h\Gamma}$  and  $m_{hVB}$ ) in-plane cyclotron masses, band gap separation ( $E_{2D-DFT}$ ) and VBE $_{\Gamma}$  to VBM energy separation ( $\Delta E_{VB}$ ) as derived from the DFT for 1, 2, 5 and 10 layer InSe. The values for bulk  $\gamma$ -InSe are from the literature.<sup>232</sup>

	$m_{e\Gamma}/m_0$	$m_{h\Gamma}/m_0$	$m_{hVB}/m_0$	$E_{2D-DFT}$ (eV)	$\Delta E_{VB}$ (meV)
Bulk	0.138	-0.730	-0.730	1.264	0
10-Layer	0.12	1.03	-1.02	1.361	11
5-Layer	0.13	0.68	-0.80	1.528	35
2-Layer	0.15	0.61	-1.05	2.000	70
1-Layer	0.18	0.70	-2.1	2.570	72

Figure 6.8 represents a basic Landau level spectrum for bulk and 1, 2, 5 and 10 layer InSe, calculated using Equations 6.1 and 6.2 and using the effective mass parameters given in Table 6.1. The table also includes the band gap energy ( $E_{2D-DFT}$ ) and the energy separation between the VBM and  $VBE_{\Gamma}$  at  $B = 0$  T as derived by DFT. We note that since DFT underestimates the band gap energy, we set the value for bulk from the literature and use the calculated quantum shift to estimate  $E_{2D-DFT}$  at different  $L$ . Here we assume that near each extremum the energy-momentum dispersion curve can be described to a good approximation by a parabolic curve.

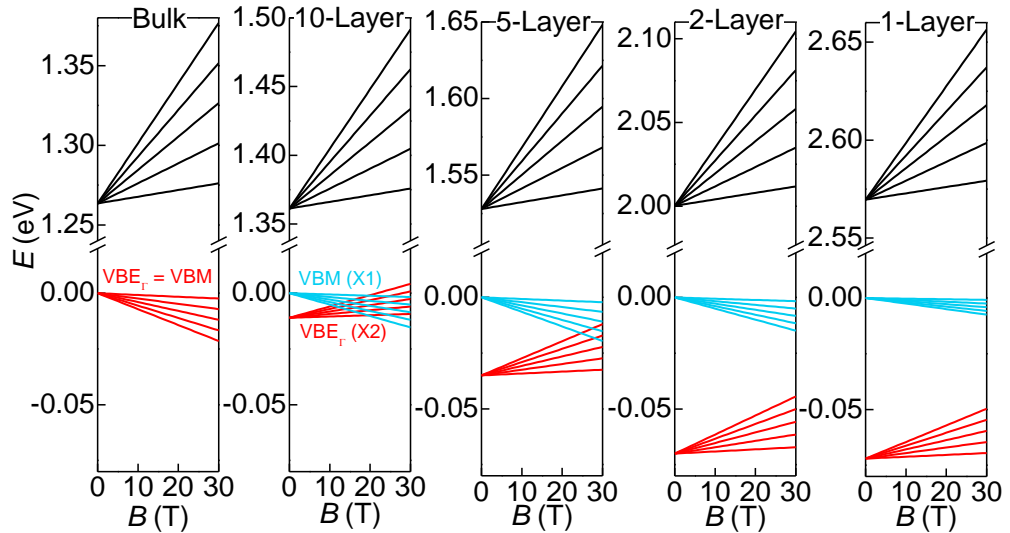


**Figure 6.8.** Energy of the Landau levels versus  $B$  for electrons near the conduction band minimum (black) and holes at  $\Gamma$  ( $VBE_{\Gamma}$ ) (red) and at the valence band maximum (VBM) (cyan) for bulk and 1, 2, 5 and 10 layer InSe.

As the energy shift of the LLs are proportional to the in-plane cyclotron mass, the LLs at the VBM and at  $VBE_{\Gamma}$  tend to overlap and admix with increasing  $B$ . The optical transition X1 arises from recombination of electrons at the bottom of the CB with holes at the VBM and requires phonons with large wavevector ( $k \sim 10^9 \text{ m}^{-1}$ ). Holes with a large value of  $k$  near the edge of the valence band overlap mainly with LLs in the CB with high  $n$ -indices, whereas their overlap with LLs at the bottom of the CB is small. Thus, this transition should

be quenched by a large magnetic field when the degeneracy of the LLs is lifted. On the other hand, optical transitions near  $\Gamma$  (X2) are allowed and involve electron and hole LLs with the same quantum number. From Figure 6.7a, it can be seen that the X1 and X2 PL bands are separated in energy by  $\Delta E_{VB} \sim 20$  meV, which is comparable with the calculated  $\Gamma$ -VBM energy splitting ( $\Delta E_{VB} = 23$  meV) for flakes with  $L \sim 7$  layers (Figure 6.2b); the energy peak position of the two PL peaks is also consistent with an InSe nanosheet of the same thickness. This suggests that X1 and X2 arise from electron recombination with holes from the two closed edges of the VB (Figure 6.9). As the X1 band is weakly shifted by  $B$  and persists at high  $B$  (Figure 6.6), it is possible that the holes are distributed over a range of energies in the VB and hence optical transitions involve hole states with a broad range of  $k$ -vectors near the VBM. Furthermore, the larger energy shift of the X2 band and its significant increase beyond a magnetic field  $B \sim 10$  T (Figure 6.6), suggests a transition of the hole cyclotron motion from orbits in  $k$ -space centred at the VBM to adjacent orbits around  $\Gamma$ , which overlap more effectively with the conduction electrons (Figure 6.9). The measured energy shift of the X2 band is well described by the calculated energy of the interband transition between LLs with  $n = 0$  *i.e.*,

$$\Delta E_{VB} = \frac{\hbar\omega}{2} = \frac{\hbar eB}{2\mu_{\Gamma}}, \quad (6.3)$$

where

$$\frac{1}{\mu_{\Gamma}} = \frac{1}{m_{e\Gamma}} + \frac{1}{m_{h\Gamma}} \quad (6.4)$$

gives the in-plane reduced mass at  $\Gamma$  ( $\mu_{\Gamma}$ ) for 7 layers of InSe. The crossover of hole orbits is equivalent to a magnetic field breakdown between closed Fermi surfaces in the plane normal to the magnetic

field.<sup>237</sup> The condition for magnetic breakdown should be determined by the form of the valence band. With decreasing layer number, the distance in  $k$ -space of the VBM from the centre of the Brillouin zone increases (Figure 6.2), thus a correspondingly larger magnetic field should be required for the breakdown to occur.

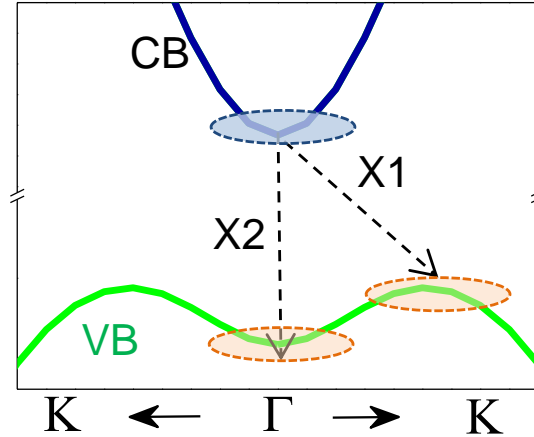


**Figure 6.9.** Interband transitions associated with the X1 and X2  $\mu$ PL bands: hole cyclotron orbits (dashed circled) are centred at different  $k$ -points of the valence band; hole orbits centred at  $\Gamma$  have larger overlap with the electron cyclotron orbits.

Our model does not take into account Coulomb interactions between electrons and holes, which can contribute to the measured  $B$ -dependence of the PL spectrum. In bulk InSe, the exciton binding energy is  $E_{ex} \sim 14$  meV.<sup>106,193</sup> This should be compared with the magneto-confinement energy of the exciton, which is

$$\hbar\omega_c = \hbar \frac{eB}{\mu}, \quad (6.5)$$

where  $\mu$  is the in-plane exciton reduced mass. We estimate that at sufficiently large  $B$  ( $> 20$  T),  $\hbar\omega_c > E_{ex}$  and Coulomb interaction effects should be weak compared to the changes of the electron and hole orbital motion by the magnetic field. Additionally, spin splitting effects were not observed, which is in line with the weak spin-orbit interaction expected in both bulk and atomically thin metal monochalcogenides.<sup>238</sup> Thus, the behaviour of InSe distinctly differs from that of 2D transition metal dichalcogenides, where the strong coupling between the spin

and valley degrees of freedom leads to large spin splittings in the optical spectra.<sup>233–236</sup> It is worth noting that these results have stimulated a more rigorous theoretical approach, which models the effects of an applied magnetic field on the band structure of InSe.

## 6.4 Summary

These magneto-photoluminescence studies suggest a magnetic field induced indirect-to-direct band crossover in the two dimensional metal monochalcogenide InSe. Investigating bulk samples of exfoliated InSe reveal bright and narrow ( $\sim 0.5$  meV) PL emission lines, with a small diamagnetic shift and no observable Zeeman splitting, advocating photoexcited carrier localisation and quantum-dot defect-like emission, similar to the observations in monolayer WSe<sub>2</sub>.<sup>233–236</sup> Analysis of the PL magnetic field dependence, with consideration of DFT calculations and a basic LL model suggests a magnetic field induced transition of the hole orbital motion. The indirect-to-direct crossover is attributed to the modification of the ‘Mexican hat’ features of the InSe valence band due to the application of a magnetic field perpendicular to the in-plane layers.

These experimental observations have stimulated ongoing work into the theoretical modelling of the electronic band structure of InSe nanosheets under large magnetic fields. Similar transitions in other metal monochalcogenides or systems with analogous valence band features may also be observable. The controlled changes of the electronic properties by magnetic fields provide a stringent test of theoretical models of the band structure of this class of materials, which differ qualitatively from that of other van der Waals crystals. A set of unique electronic properties and absence of large spin-related effects also provide a platform for a different range of potential applications.

# Chapter 7

## InSe van der Waals heterostructures and devices

This chapter discusses the optoelectronic properties of van der Waals heterostructures and devices with exfoliated  $\gamma$ -InSe as the photoactive component. Section 3.2 explains the fabrication procedures and Section 3.5 details the methods used when conducting the transport studies. Source-drain ( $I$ - $V_s$ ) and current-gate ( $I$ - $V_g$ ) traces, photocurrent spectroscopy, photocurrent mapping and the determination of device response time characteristics were collected by S. A. Svatek and myself. Results of this study were published in *Advanced Materials*, **27**, 3760 (2015) and *Journal of Physics: Conference Series*, **647**, 012001 (2015).

### 7.1 Introduction

The intense research interest surrounding two-dimensional layered crystals has revealed an assortment of material properties which hold promise for the next generation of photodetectors. For graphene, a high mobility  $\mu$  offers potential for ultrafast detection speeds<sup>239,240</sup> and a gapless electronic spectrum<sup>45</sup> enables photon absorption across a broad-band spectral range.<sup>241</sup> However, the small absorption and gapless nature has somewhat limited graphene photodetectors in terms of responsivity ( $R_\lambda = \Delta I / P \sim 6.1 - 100 \text{ mA/W}^{-1}$ , where  $\Delta I$  is the photocurrent and  $P$  is the incident power on the device area).<sup>20</sup> In contrast, layered van der Waals semiconductors have band gaps that cover a broad spectral range<sup>242</sup> and have demonstrated high photosensitive gain<sup>85</sup> due to strong light-matter interactions.<sup>16,32</sup> Furthermore, tuning of the electronic band structure in van der Waals semiconductor systems is possible through quantum mechanical confinement of charge carriers in ultrathin crystals, enabling further spectral selection.<sup>200,242-244</sup> A high mechanical robustness facilitates

band engineering through applied strain<sup>245,246</sup> and, when coupled with the inherent transparency of atomically thin layers, provides a route to the integration of two-dimensional semiconductors into novel multi-component flexible technologies.<sup>20</sup> The diverse properties of individual layered materials can be combined and exploited in unison through the artificial stacking of crystals in van der Waals heterostructures.<sup>3</sup> The component layers are separated by van der Waals gaps which conserve the structural integrity and electronic and optical properties of the individual atomic planes, providing a versatile range of potential configurations for specific applications. In this chapter, I present a comparison of both planar and vertical geometries of graphene-InSe-graphene heterostructures. Metal-InSe interfaces are also considered. The planar graphene-InSe interface has a favourable band alignment, facilitating the formation of Ohmic contacts and enabling the efficient extraction of photogenerated charge, with a spectral response that extends from the near-infrared to the visible spectrum (NIR-to-VIS). In the vertical van der Waals heterostructures, graphene acts as a broadband optical window capable of charge extraction from a nanoscale photosensitive channel with a high photoresponsivity at room temperature.

## 7.2 Metal-InSe junctions

The current-voltage ( $I$ - $V_s$ ) characteristics of a two-terminal metal-InSe junction under dark and illuminated conditions are shown in Figure 7.1a. Au/Ti contacts were deposited using a standard electron beam lithography method onto an InSe exfoliated nanosheet ( $L^* \sim 10$  nm and area  $A \sim 1 \mu\text{m}^2$ ). The dark current is of the order  $I_D \sim 10$  pA and an increase in the source-drain current is observed when the device is illuminated by a focussed laser beam ( $P \sim 1 - 100 \mu\text{W}$  at  $\lambda = 633$  nm). The responsivity ( $R_\lambda$ ) of the Au-InSe-Au planar heterostructure (see Figure 7.1b) decreases with increasing incident laser power and follows an empirical power law relation of the

form  $R_\lambda = CP^{-n}$  where  $n \sim 0.8$  and  $C$  is a constant. The lowest power at which the device is sensitive is  $P \sim 1 \mu\text{W}$  which corresponds to a responsivity  $R_\lambda \sim 10^{-3} \text{ A/W}$  ( $V_s = 1.5 \text{ V}$ ). This is close to larger area ( $A = 23 \mu\text{m}^2$ ) metal-InSe devices reported in the literature ( $R_\lambda \sim 3.47 \times 10^{-2} \text{ AW}^{-1}$  at  $V_s = 3 \text{ V}$ ).<sup>140</sup>

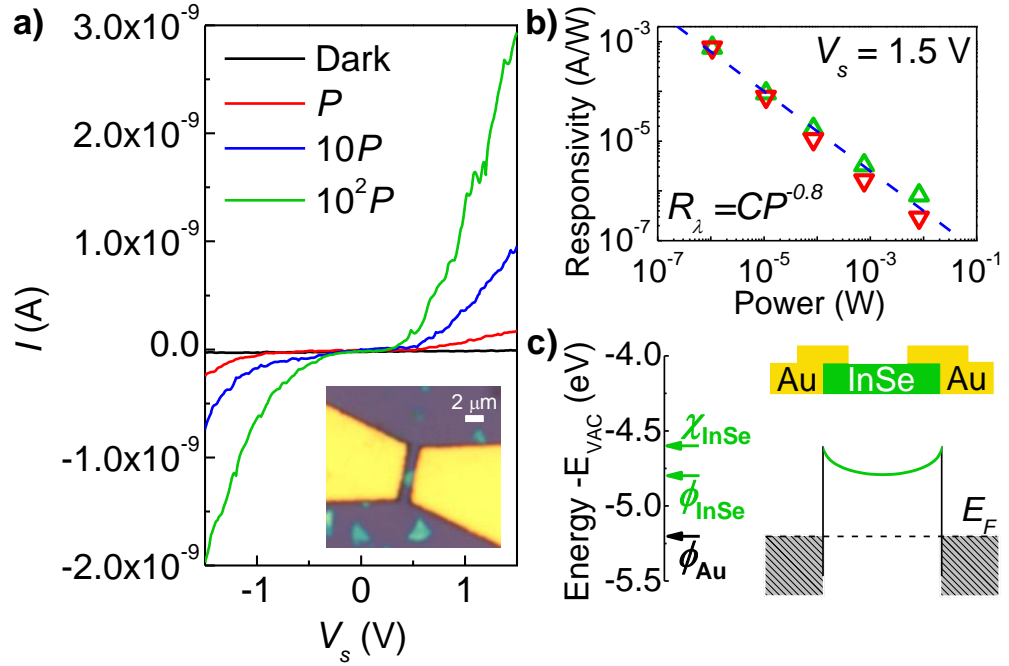


**Figure 7.1.** **a)** Current-voltage ( $I$ - $V_s$ ) trace of a two-terminal metal-InSe junction ( $L^* = 10 \text{ nm}$ ) in dark and illuminated conditions ( $P \sim 1 \mu\text{W}$  and  $\lambda = 633 \text{ nm}$ ). **Inset:** image of the device. **b)** Responsivity of planar metal-InSe devices (triangles) and empirical power law (dashed line) of the form  $R_\lambda = CP^{-n}$  where  $n \sim 0.8$  and  $C$  is a constant. **c) Left:** work function ( $\phi_{\text{InSe}}$ ) and electron affinity ( $\chi_{\text{InSe}}$ ) of InSe and work function ( $\phi_{\text{Au}}$ ) of Au with reference to the vacuum level. **Right:** band alignment for planar Au-InSe-Au heterostructure.

Both charge injection from a metal contact into InSe and the extraction of photogenerated carriers from InSe by metal electrodes is strongly dependent upon the band alignment at the interface.<sup>247</sup> The alignment between Au and InSe is represented in Figure 7.1c and, as the work function of Au ( $\phi_{\text{Au}} = -5.1 \text{ eV}$ ) is greater than InSe ( $\phi_{\text{InSe}} = -4.8 \text{ eV}$ ), a Schottky barrier (*i.e.*,  $\phi_M > \phi_{\text{SC}}$ )<sup>248</sup> is formed at the junction when the Fermi levels ( $E_F$ ) align. For the purpose of charge

extraction, the presence of a Schottky barrier may hinder the overall responsivity of the devices.

Attempts have been reported in the literature to optimise the metal contacts on InSe. In particular, the electronic properties of various different metal interfaces with exfoliated InSe nanosheets were studied as part of the optimisation of InSe-based FETs.<sup>150</sup> Feng *et al.* assumed that the electronic performance for each combination (Al, Ti, Cr or In with InSe) would be dominated by the individual Schottky barrier height.<sup>150</sup> The contact morphology was also found to play a significant role and similar conclusions were reached for vdW semiconductors in general.<sup>150,247,249</sup> In comparison to 3D metal-semiconductor (SC) contacts, the ultrahigh quality of vdW surfaces, which contain a low density of dangling bonds, do not tend to form covalent bonds with the metal contact.<sup>247,249</sup> Instead, for top surface contacts, a van der Waals gap may form which provides an additional tunnel barrier in addition to the Schottky barrier.<sup>247,249</sup> Contacts in these studies are evaluated by three criteria: Schottky barrier height, the presence of tunnel barriers (degree of physical interface separation) and the strength of orbital overlap. In the case of orbital overlap, strong adhesion between the metal and semiconductor (SC) interfaces (large overlapping of *d*-orbitals) can result in the formation of interface covalent bonds. This can result in a strong perturbation of the semiconductor band structure and a metallisation of the metal-SC interface thus leading to an Ohmic contact.<sup>247,249</sup>

Surface contaminants introduced during the processing of vdW materials can also prove detrimental to device operation. For example, polymer residues at the metal-SC interface (*i.e.*, the remnants of the polymer mask used for electron beam lithography processing) provide unwanted additional contact resistance and are well reported as being difficult to be completely removed from vdW surfaces.<sup>250–252</sup> Photo-sensitive InSe devices fabricated using shadow masks, rather than the

polymer masks used with EBL, report a higher responsivity in the range  $R_\lambda = 7 - 2.31 \times 10^4 \text{ AW}^{-1}$  at  $V_s = 5 - 10 \text{ V}$ .<sup>141,159</sup> Other enhancements to the responsivity of InSe devices can be achieved through the formation of avalanche photodiodes with plasmonic nanostructures ( $R_\lambda = 1.7 - 37 \text{ AW}^{-1}$  at  $V_s = 30 - 50 \text{ V}$ )<sup>158</sup> and back-gating of InSe FETs ( $R_\lambda = 157 - 5.68 \times 10^4 \text{ AW}^{-1}$  at  $V_s = 5 - 10 \text{ V}$  and  $V_g = 40 - 70 \text{ V}$ ).<sup>141,159</sup>

### 7.3 A planar graphene-InSe-graphene heterostructure

Figure 7.2a shows a planar graphene-InSe-graphene heterostructure, fabricated by the methods described in Section 3.2.2. The separation of the graphene electrodes defines the channel length  $l_c \sim 2 \mu\text{m}$ . The channel width ( $w_c \sim 10 \mu\text{m}$ ) and thickness ( $L \sim 30 \text{ nm}$ ) are defined by the *n*-InSe nanosheet. The *n*-Si layer of the supporting SiO<sub>2</sub>/Si wafer serves as a back-gate. Each graphene electrode ( $g_1$  and  $g_2$ ) is contacted by a separate set of Au/Ti metal pads allowing the electronic quality of the graphene to be assessed (*i.e.*,  $V_s^1$  Figure 7.2b). Both  $g_1$  and  $g_2$  exhibit a linear dependence of the source-drain current on the applied bias voltage and show a conductance minimum at a gate voltage of  $V_g \sim 60 \text{ V}$  (Figure 7.2c), indicating *p*-type doping with a hole concentration of  $p \sim 5 \times 10^{12} \text{ cm}^{-2}$ , typical of CVD-grown graphene sheets.<sup>253</sup> The source-drain current through the graphene-InSe-graphene heterostructure has a linear dependence on the applied bias voltage ( $V_s^2$  in Figure 7.2b), symmetric relative to the polarity of the applied field and also increases with increasing gate voltage ( $V_g$ ), as shown in Figure 7.3a. The linearity and symmetry of the  $I$ - $V_s$  characteristics are preserved under optical illumination by a focussed He-Ne laser ( $\lambda = 633 \text{ nm}$  and  $d_R \sim 1 \mu\text{m}$ ) at  $P = 0.5 - 10^4 \text{ nW}$  (Figure 7.3b).

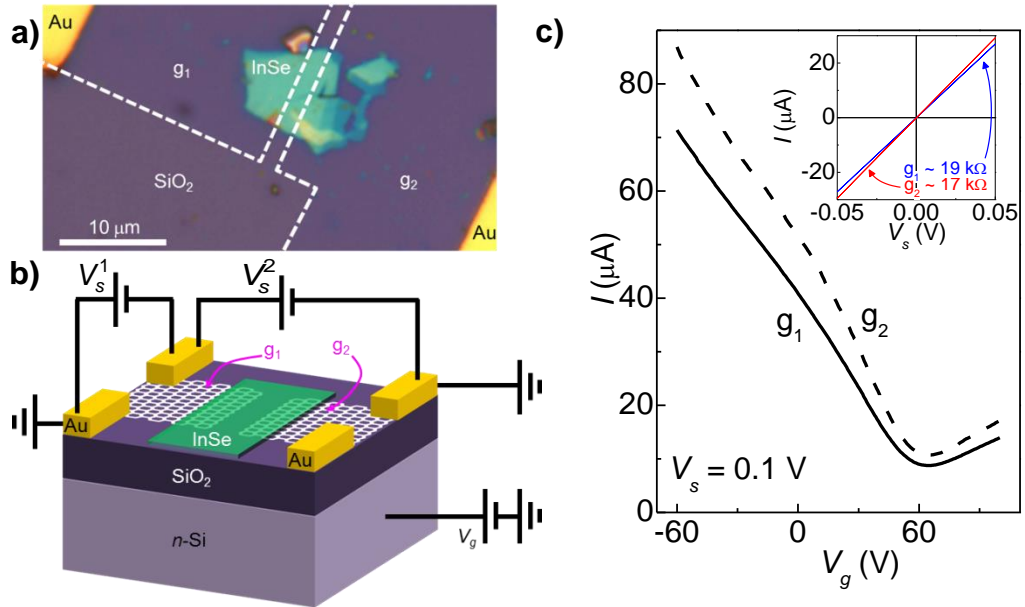


**Figure 7.2.** **a)** Optical image of a planar graphene-InSe heterostructure. **b)** Each graphene electrode has two metal contact pads (Au/Ti) which enables the individual layers to be characterised ( $V_s^1$ ), in addition to the planar heterostructure ( $V_s^2$ ). **c)** Source-drain current response in the graphene electrodes ( $V_s = 0.1$  V) to a gate voltage ( $V_g$ ) applied via an  $n$ -Si back-gate **Inset:**  $I$ - $V_s$  trace of individual graphene electrodes  $g_1$  and  $g_2$ .

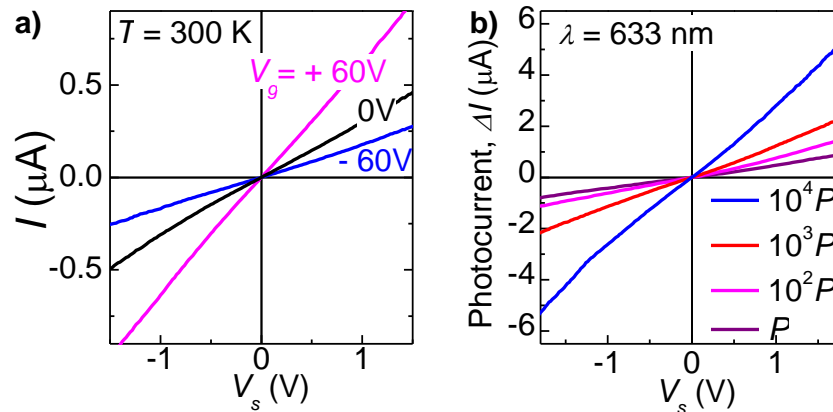


**Figure 7.3.** **a)** Current-voltage ( $I$ - $V_s$ ) characteristics of an  $n$ -Si back-gated, planar graphene-InSe-graphene heterostructure in the dark at  $T = 300$  K for gate voltages  $V_g = -60, 0$  and  $60$  V. **b)** Photocurrent,  $\Delta I$ , versus  $V_s$  at  $T = 300$  K and  $V_g = 0$  V under light illumination with a focussed laser beam ( $d_R \sim 1$   $\mu\text{m}$ ) of power  $P, 10^2P, 10^3P$  and  $10^4P$  ( $P = 0.5$  nW and  $\lambda = 633$  nm).

A spatially resolved photocurrent map was acquired by scanning a focussed laser beam across the surface of the graphene-InSe-graphene heterostructure ( $P \sim 500$  nW,  $d_R \sim 1$   $\mu\text{m}$ ,  $V_s = 0.1$  V and  $V_g = 0$  V) and shows that photocurrent generation occurs primarily at

the InSe nanosheet located between the two graphene electrodes (Figure 7.4).

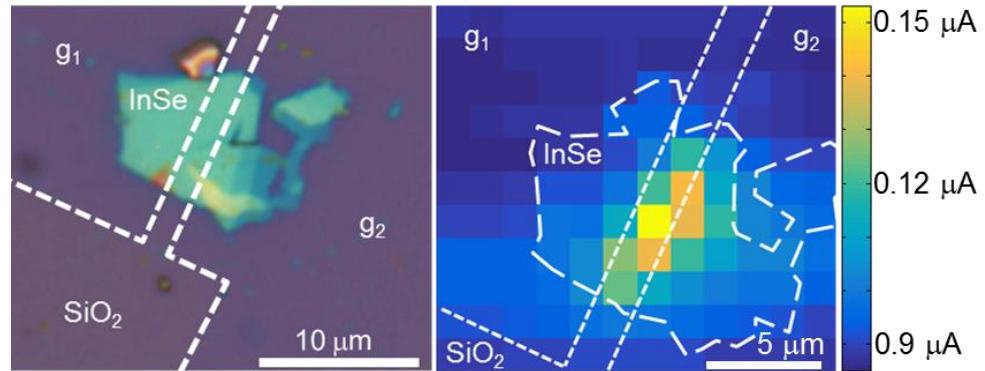


**Figure 7.4.** **Left:** optical image of a planar graphene-InSe-graphene heterostructure on an oxidised Si substrate. **Right:** photocurrent map indicating that photoresponse arises primarily from the InSe layer between the two graphene electrodes,  $g_1$  and  $g_2$  ( $P \sim 500\ \text{nW}$ ,  $\lambda = 633\ \text{nm}$ ,  $V_s = 0.1\ \text{V}$  and  $V_g = 0\ \text{V}$ ).

The transport characteristics of the heterostructure are reproducible and stable, and a relatively fast response time is observed under dark conditions with a cut-off frequency of  $f \sim 10^4\ \text{Hz}$  (Figure 7.5a). A characteristic temporal dependence of the current modulated by an AC square-wave bias  $V_s$  ( $\pm 1\ \text{V}$ ), at a frequency of  $f = 100\ \text{Hz}$ , is shown in Figure 7.5b. The temporal response of the photocurrent is slower (Figure 7.5c, generated under a DC bias  $V_b = 1\ \text{V}$  and illumination by a mechanically chopped  $\lambda = 633\ \text{nm}$  laser beam of  $P_d < 0.1\ \text{Wcm}^{-2}$ ), with a rise time of  $\tau_r \sim 1\ \text{ms}$  and decay time of  $\tau_d \sim 10\ \text{ms}$  and does not appear to be affected by  $V_g$ . A broad-band spectral response from the near-infrared-to-visible (NIR-to-VIS) wavelength range is observed under unfocussed optical illumination (Figure 7.6). The photoinduced current,  $\Delta I$ , is weakly modulated by the gate voltage  $V_g$  and the dependence on  $V_g$  is opposite to that observed for the dark current, *i.e.*,  $\Delta I$  decreases with increasing  $V_g$  from  $-60$  to  $+60\ \text{V}$ . A similar behaviour is observed under excitation from a laser source ( $P_d < 0.1\ \text{Wcm}^{-2}$  and  $\lambda = 633\ \text{nm}$ ), as shown in the colour map of  $\Delta I$  in the inset of Figure 7.6.

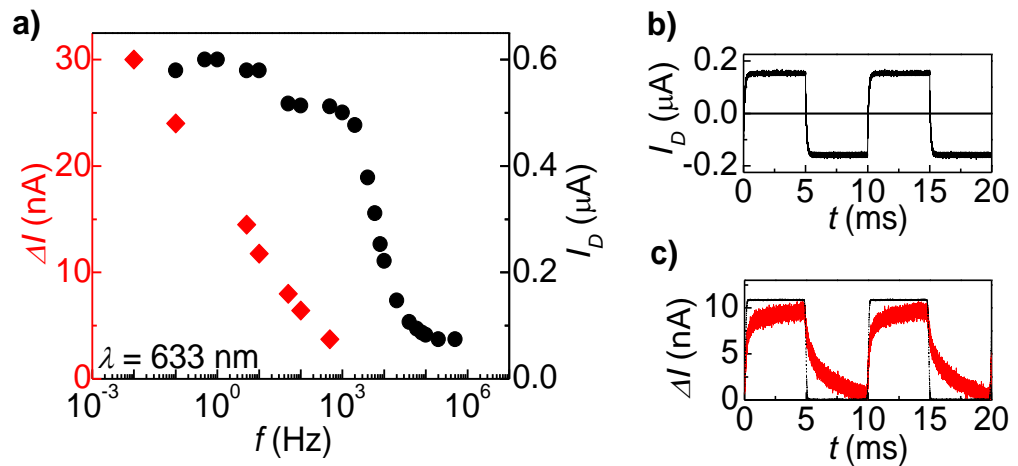


**Figure 7.5.** **a)** Temporal response of the dark current,  $I_D$ , (circles, right axis) and photocurrent,  $\Delta I$ , (diamonds, left axis) at  $P < 1$  mW and  $\lambda = 633$  nm for the planar graphene-InSe-graphene heterostructure at room temperature. **b)** Temporal dependence of the dark current,  $I_D$ , to an AC square-wave driving bias,  $V_s = \pm 1$  V, of  $f = 100$  Hz. **c)** Temporal dependence of the photogenerated current to a mechanically modulated excitation source at frequency of  $f = 100$  Hz (dashed line). Photocurrent generated by a mechanically chopped  $\lambda = 633$  nm laser beam of  $P_d < 0.1$  Wcm $^{-2}$  and DC bias of  $V_b = 1$  V.

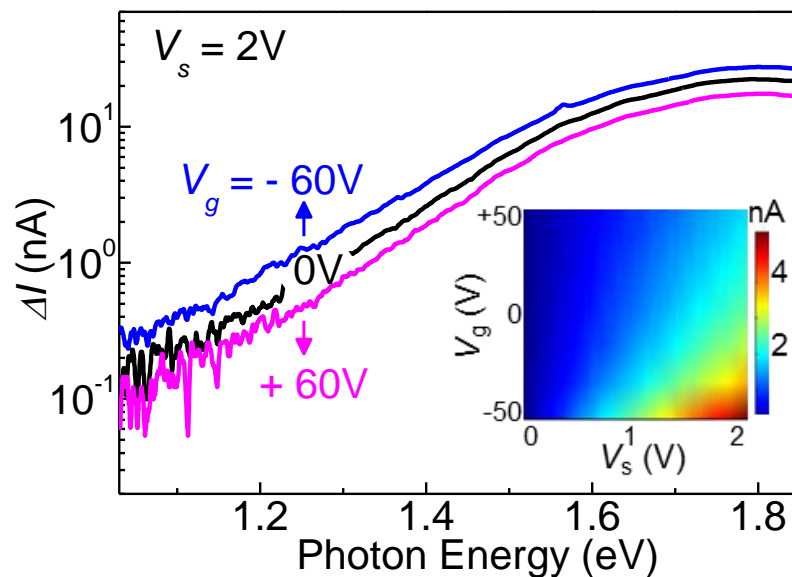


**Figure 7.6.** Photoconductivity spectra at  $T = 300$  K and  $V_s = 2$  V with unfocussed monochromated light and power  $P \sim 10$  pW. **Inset:** a colour map of  $\Delta I$  versus  $V_g$  and  $V_s$  under laser excitation at  $P_d < 0.1$  Wcm $^{-2}$  and  $\lambda = 633$  nm.

Compared to the planar Au-InSe-Au junctions, the graphene-InSe-graphene heterostructures have a greater maximum responsivity to optical illumination (by a factor of  $>10^3$ ), indicating the superiority of

graphene electrodes for extraction of photogenerated charge carriers (Figure 7.7). At limits approaching 2D, the quality of the interface can dominate the operation of nanoscale devices. Abrupt heterointerfaces between InSe and other layered compounds, such as GaSe,<sup>124</sup> have been shown to form high quality junctions,<sup>117,254</sup> due to the low density of surface states on the InSe surface.<sup>117,254</sup> In order to obtain a high quality interface between the CVD-graphene electrodes and the exfoliated *n*-InSe nanosheet, the graphene surface was annealed in an Ar:H (95:5) gas mixture at 400°C for several hours and then transferred to a nitrogen cabinet in which the mechanical exfoliation and deposition of *n*-InSe was performed, minimising the exposure of the layered surfaces to ambient conditions.

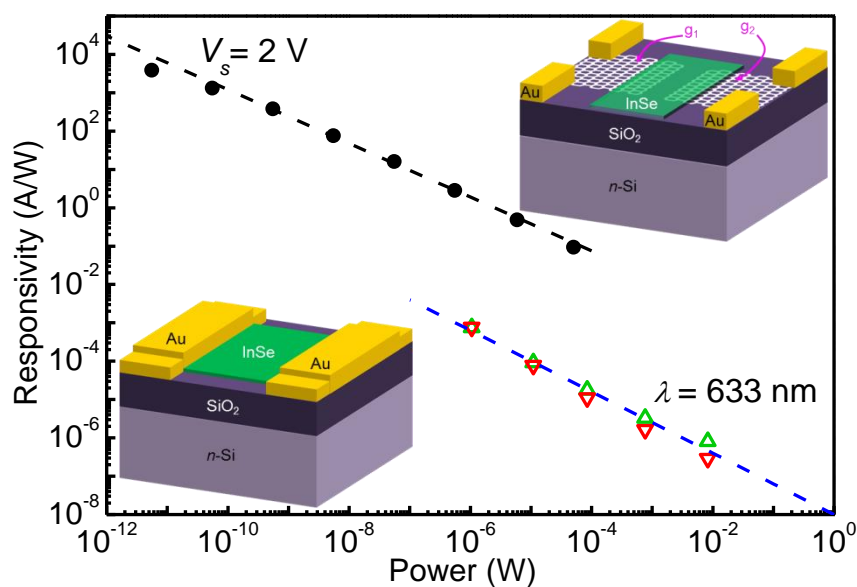


**Figure 7.7.** Comparison of the responsivity for the graphene-InSe-heterostructure (filled circles) and Au-InSe-Au junctions (empty triangles) under optical illumination ( $\lambda = 633$  nm) at  $T = 300$  K. Dashed lines represent empirical power laws of the form  $R_\lambda = CP^{-n}$  where  $n \sim 0.8$  for the Au-InSe junction and 0.7 for the graphene-InSe junction,  $C$  is a constant. Insets represent respective devices (**Left:** Au- and **Right:** graphene-InSe junctions).

The relative band alignment between graphene and InSe is shown in Figure 7.8. The possible presence of impurities and/or defects at the interface have been neglected. The electron affinity of graphene ( $\chi_g = -4.5$  eV)<sup>249</sup> lies closer to the vacuum level than that of

bulk InSe ( $\chi_{\text{InSe}} = -4.6 \text{ eV}$ )<sup>254</sup> and the work function of graphene ( $\phi_g$ ) can be tuned relative to *n*-type InSe ( $\phi_{\text{InSe}} = 4.8 \text{ eV}$ )<sup>124</sup> by applying a transverse electric field (gate voltage,  $V_g$ ).<sup>1</sup> Compared to InSe, graphene has a lower density of states when the chemical potential is near the Dirac point, which leads to stronger gating effects on the graphene work function than on InSe.<sup>1</sup> In the hole-doped CVD graphene sheets, the Fermi level lies at the Dirac point at  $V_g = 60 \text{ V}$  ( $\phi_g = -4.5 \text{ eV}$ ) and reduces by approximately  $0.3 \text{ eV}$  ( $\phi_g = -4.85 \text{ eV}$ ) at  $V_g = -60 \text{ V}$ .<sup>253</sup> Across the range  $V_g = -60$  to  $+60 \text{ V}$ , the work function of graphene is higher than, or comparable to, that of InSe. Accordingly, under equilibrium conditions, electrons may transfer from graphene into InSe and form an accumulation layer at the interface. Such a band alignment at each graphene-InSe interface facilitates the formation of an Ohmic contact, consistent with the linearity of the  $I$ - $V_s$  characteristics for the graphene-InSe-graphene device (Figure 7.3).

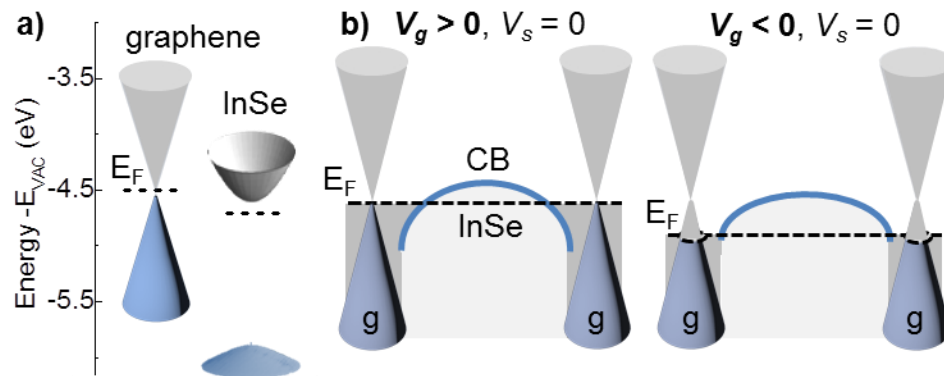


**Figure 7.8.** **a)** Energy bands for isolated graphene and InSe layers with electron affinities of  $\chi_g = -4.5$  and  $\chi_{\text{InSe}} = -4.6 \text{ eV}$  and a band gap energy for InSe of  $E_g = 1.26 \text{ eV}$  at  $300 \text{ K}$ . The Fermi level,  $E_F$ , is shown for graphene at the neutrality point and for *n*-InSe at  $\sim 0.2 \text{ eV}$  below the conduction band (CB) minimum. **b)** Band alignment at equilibrium ( $V_s = 0 \text{ V}$ ) under various applied gate voltages  $V_g$ . For  $V_g > 0$ , the Fermi level of graphene rises toward the Dirac point and electrons tend to diffuse into the InSe layer; as the concentration of holes increases, for  $V_g < 0$  the Fermi level in graphene moves closer to that of InSe and electrons retreat from InSe.

The proposed band alignment also explains the opposite dependence of the dark current (increases) and photocurrent

(decreases) on an increasing applied gate voltage. For a positive gate voltage,  $V_g > 0$  V, the Fermi level in graphene moves upwards toward the Dirac point and more electrons diffuse into InSe, acting to decrease the effective length,  $l^*$ , over which the bias voltage is dropped (Figure 7.8b). Conversely, for a negative gate voltage,  $V_g < 0$  V, the Fermi level in graphene shifts to lower energies, towards the Fermi level of InSe; electrons retreat from InSe and thus the effective length increases. A larger effective length enables a larger number of charge carriers to be photogenerated and hence a large photocurrent is exhibited; in contrast, this acts to reduce the dark current.

For the graphene-InSe-graphene heterostructures, the high responsivity is attributed to the mechanism of photoconductive gain.<sup>20</sup> Incident light of power  $P$  creates electron-hole pairs in InSe when the photon energy,  $h\nu$ , exceeds the band gap energy. Under steady state conditions, the densities of photogenerated electrons ( $\Delta n$ ) and holes ( $\Delta p$ ) are equal (to conserve charge neutrality) and can be expressed as

$$\Delta n = \Delta p = G\tau_i \quad (7.1)$$

where  $\tau_i$  is the minority carrier lifetime (holes for  $n$ -InSe)<sup>248</sup> and the rate of carrier generation by light,  $G$ , is given by

$$G = (\alpha L) \times \left( \frac{P}{h\nu} \right) \times \left( \frac{1}{w_c l_c L} \right) \quad (7.2)$$

where  $\alpha$  is the absorption coefficient of InSe at photon energy  $h\nu$ ,  $L$  is the nanosheet thickness,  $P$  is the absorbed laser power,  $w_c$  is the channel width and  $l_c$  is the channel length. For InSe, the effective carrier mass of electrons ( $m_e$ ) is lighter than for the holes ( $m_h$ ), see Table 2.1,<sup>121</sup> and results in a higher mobility,  $\mu_e$ . This is given by<sup>255</sup>

$$\mu_e = \frac{e\tau_s}{m_e} \quad (7.3)$$

where  $\tau_s$  is the electron scattering time. The photocurrent is therefore likely to be dominated by the electron current,

$$\Delta I = (\Delta ne) \times (v_d) \times (Lw_c), \quad (7.4)$$

where

$$v_d = \frac{l_c}{\tau_t} \quad (7.5)$$

is the electron drift velocity and  $\tau_t$  is the electron transit time across the InSe channel length  $l_c$ . Thus, combining equations 7.1, 7.2, 7.4 and 7.5, the photocurrent can be expressed as

$$\Delta I = e(\alpha L) \times \left( \frac{P}{h\nu} \right) \times \left( \frac{\tau_l}{\tau_t} \right) \quad (7.6)$$

from which the responsivity ( $R_\lambda$ ), external quantum efficiency ( $EQE$ ) and internal quantum efficiency ( $IQE$ ) can be defined:

$$R_\lambda = \frac{\Delta I}{P} = e(\alpha L) \times \left( \frac{1}{h\nu} \right) \times \left( \frac{\tau_l}{\tau_t} \right), \quad (7.7)$$

$$EQE = R_\lambda \left( \frac{h\nu}{e} \right) = (\alpha L) \times \left( \frac{\tau_l}{\tau_t} \right), \quad (7.8)$$

$$IQE = \frac{EQE}{(\alpha L)} = \left( \frac{\tau_l}{\tau_t} \right). \quad (7.9)$$

Equations 7.7 – 7.9 indicate that large values of  $R_\lambda$ ,  $EQE$  and  $IQE$  can be achieved if the lifetime of the minority carriers (holes) is longer than the transit time of the electrons. Here, the  $EQE$  and  $IQE$  are defined as the number of electrons collected at the graphene electrodes which contribute to the photocurrent ( $\Delta I/e$ ), divided by the number of incident or absorbed photons ( $P/h\nu$  or  $\alpha LP/h\nu$ ), respectively, and incorporate the gain of the graphene-InSe-graphene heterostructures. Furthermore, the specific detectivity  $D^*$ , a figure of merit allowing ease of comparison between different device geometries, can be defined as

$$D^* = \frac{R_\lambda (BA)^{1/2}}{I_D}, \quad (7.10)$$

where  $I_D$  is the dark current,  $B$  is the frequency bandwidth and  $A$  is the area of the channel. Assuming a dominant shot noise in the dark current  $I_D$ , the detectivity can be expressed as

$$D^* = R_\lambda \left( \frac{A}{2eI_D} \right)^{1/2}. \quad (7.11)$$

As seen for the planar graphene-InSe-graphene heterostructure in Figure 7.7, the measured responsivity is strongly dependent upon the incident optical power and reaches a maximum value of  $R_\lambda = 4 \times 10^3 \text{ AW}^{-1}$  for the lowest detectable incident power  $P = 10 \text{ pW}$  at  $V_s = 2 \text{ V}$ ,  $V_g = 0 \text{ V}$  and  $\lambda = 633 \text{ nm}$ . This corresponds to  $\tau_l/\tau_t \sim 9.8 \times 10^3$  for  $\alpha \sim 4 \times 10^5 \text{ m}^{-1}$  at  $h\nu = 1.96 \text{ eV}$  ( $\lambda = 633 \text{ nm}$ ). For  $l_c = 2 \text{ }\mu\text{m}$ , this gives  $\text{EQE} \sim 7.8 \times 10^3$ . The specific detectivity is estimated to be  $D^* \sim 4 \times 10^{10} \text{ m s}^{-1/2} \text{ W}^{-1}$  or  $\sim 4 \times 10^{12} \text{ Jones}$ , where  $A = 20 \text{ }\mu\text{m}^2$  and  $I_D = 0.6 \text{ }\mu\text{A}$  at  $V_s = 2 \text{ V}$ . As shown in Figure 7.6, the photoresponse depends on the incident photon energy.  $R_\lambda$  and  $\text{EQE}$  decrease by factors of 30 and 50, respectively, for  $h\nu$  decreasing from  $\sim 2$  to  $1.3 \text{ eV}$ .

The strong dependence of  $R_\lambda$  on  $P$  appears to be a common characteristic of many other van der Waals photodetectors with graphene electrodes.<sup>33,100,111,256–259</sup> Considering Equation 7.7, the ratio between the minority carrier lifetime ( $\tau_l$ ) and electron transit time ( $\tau_t$ ) suggests the  $R_\lambda$  may be reduced due to a decrease of  $\tau_l$  and/or increase in  $\tau_t$ . With increasing incident power, there will be a greater density of photogenerated carriers which may lead to enhanced scattering effects acting to increase the carrier transit time  $\tau_t$ . A high population of charge carriers could also induce Auger recombination processes, increasing the recombination rate and decreasing  $\tau_l$ . This

process is expected to be enhanced in 2D vdW crystals for recombination on trap states due to stronger Coulomb interactions. When approaching the 2D limit, charge impurities located at the InSe-SiO<sub>2</sub> interface will be in closer proximity to photogenerated charge carriers leading to further scattering events. Finally,  $R_{\lambda}$  decreases linearly with decreasing applied bias voltage  $V_s$ , which is expected from the increase in electron transit time  $\tau_t = l_c^2/\mu V_s$ , and is supported by Ohmic  $I$ - $V_s$  characteristics for the photocurrent (Figure 7.2b). For  $V_s = 2$  V,  $l_c = 2$   $\mu\text{m}$  and  $\mu = 0.1$   $\text{m}^2\text{V}^{-1}\text{s}^{-1}$ ,<sup>154</sup> the electron transit time is estimated as  $\tau_t = 2 \times 10^{-11}$  s and minority carrier lifetime as  $\tau_l \sim 2 \times 10^{-7}$  s.

#### 7.4 Vertical graphene-InSe-graphene heterostructures

Since graphene is optically transparent, a high photoresponsivity can also be achieved in multilayer systems where the InSe and graphene layers are stacked vertically with the top graphene layer acting as a broad-band optical window. These structures have the additional advantage that the separation of the graphene electrodes, determined by the thickness  $L$  of the InSe nanosheet, is smaller, leading to a more sensitive photodetector through a decrease of the carrier transit time ( $\tau_t$ ).

Figure 7.9 shows the two vertical graphene-InSe-graphene heterostructure device types (A and B), fabricated by the methods detailed in Section 3.2.3. In device type A, the exfoliated graphene source-drain electrodes are separated by an exfoliated InSe nanosheet with  $L = 27$  nm. The overlapping area  $A \sim 16$   $\mu\text{m}^2$  between the top and bottom graphene layers ( $g_1$  and  $g_2$ ) is outlined in the optical image in Figure 7.9. For device B, the CVD-grown and EBL processed graphene electrodes are separated by an exfoliated InSe nanosheet with  $L = 130$  nm (multiple devices were fabricated with different  $L$ ) and an isolating polymer layer of AR-N. A window in the AR-N layer above the

InSe nanosheet was developed by EBL processing and solvent etching. This enabled mechanical contact between the top graphene layer ( $g_1$ ) and InSe and resulting in an overlapping area  $A \sim 4\mu\text{m}^2$ .

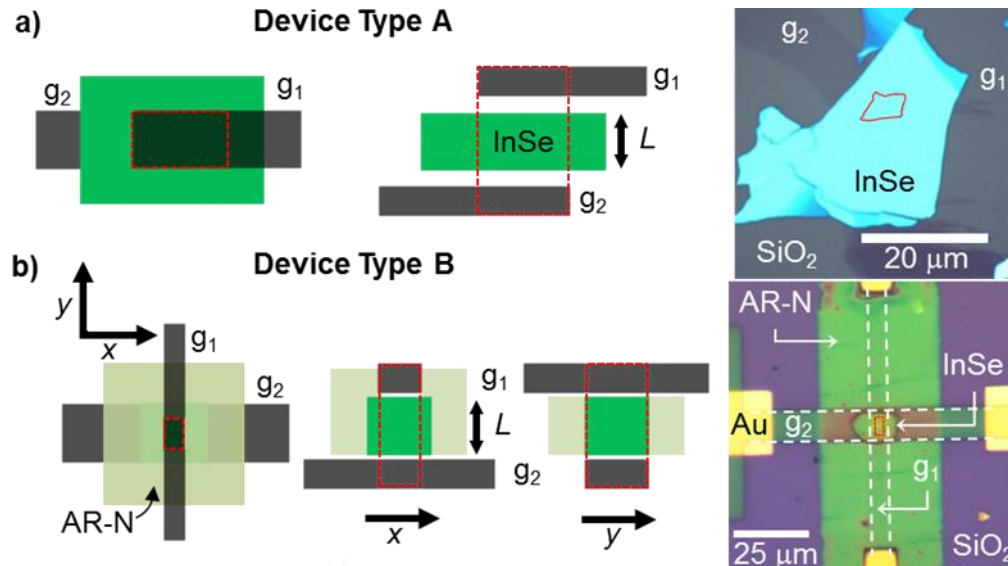


**Figure 7.9.** **a)** Top-down, cross-sectional and optical images of a vertical graphene-InSe-graphene heterostructures fabricated by method A and **b)** method B. The graphene electrodes,  $g_1$  and  $g_2$ , are separated by an InSe nanosheet of thickness  $L = 27\text{ nm}$  and  $L = 130\text{ nm}$  in device type A and B, respectively.

In the vertical heterostructures the dark current,  $I_D$ , dependence on the source-drain voltage,  $V_s$ , is non-linear and asymmetric (Figure 7.10a). This contrasts with the Ohmic behaviour observed for the planar heterostructures (Figure 7.3). In general, there are more processing steps involved in the fabrication of both types of vertical heterostructure (Section 3.2.3) where both the graphene and the InSe surfaces are exposed to polymer resists and water as part of the patterning and transfer processes, which may compromise the graphene-InSe interface. In particular, residual polymer residues at the graphene-InSe interface are likely to introduce spurious contact resistance.

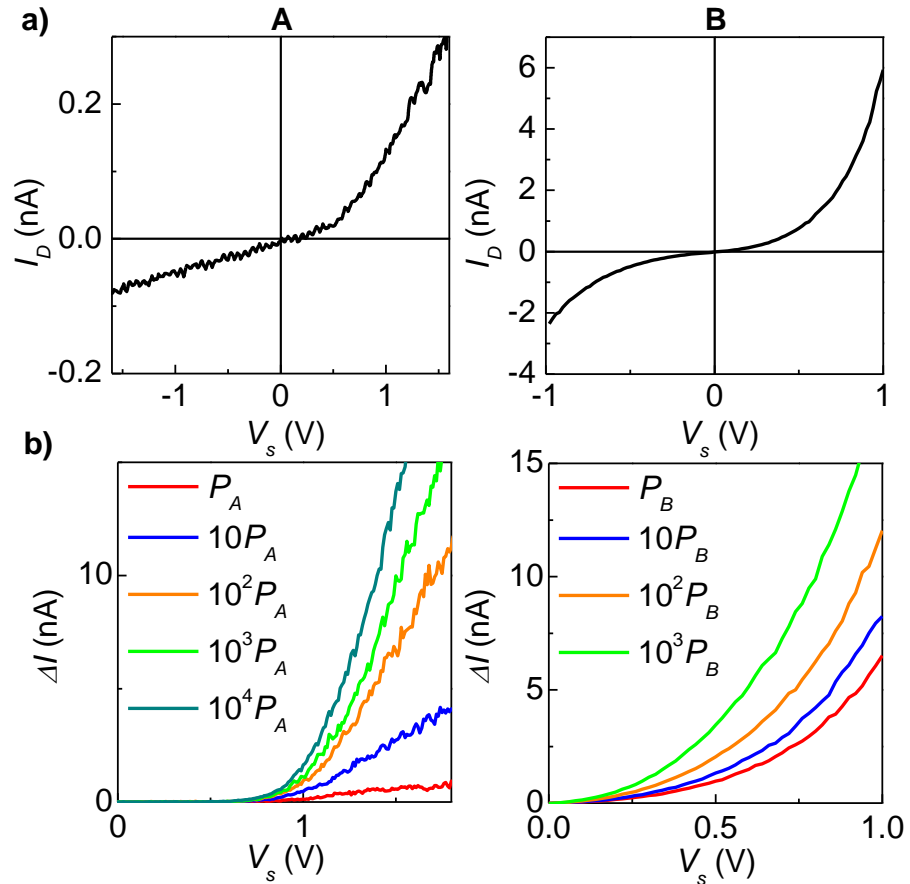


**Figure 7.10.** **a)**  $I$ - $V_s$  characteristics under dark conditions for vertical graphene-InSe-graphene heterostructure devices of type A and type B. **b)** Photocurrent,  $\Delta I$ , versus  $V_s$  at  $T = 300$  K for device architecture A and B.  $P_A = 40$  fW and  $P_B = 100$  fW at  $\lambda = 633$  nm.

Despite the likely presence of interface contaminants introduced through processing, devices of type A and B exhibit a stable and reproducible photoresponse (Figure 7.10b), localised to the area of overlapping graphene electrodes (Figures 7.11 and 7.12 for device type A and B, respectively). The temporal response of the source-drain current to an AC driving signal (dark conditions) and mechanically modulated photoexcitation is similar to that for the planar InSe-graphene heterostructure. However, the dark current cut-off frequency is estimated to be an order of magnitude higher ( $\sim 10^5$  Hz) in the vertical structure when compared to the planar device geometry (Figure 7.13).

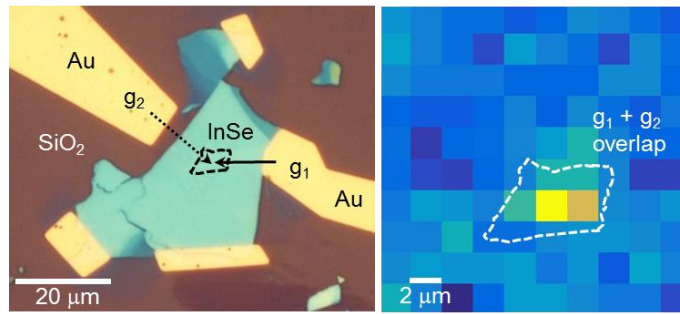


**Figure 7.11. Left:** optical image of a vertical heterostructure of device type A. Overlapping area between graphene electrodes,  $g_1$  and  $g_2$ , is  $A \sim 16 \mu\text{m}^2$  (outlined). **Right:** photocurrent map indicating that  $\Delta I$  arises primarily from the region of overlapping graphene electrodes separated by the  $L = 27 \text{ nm}$  InSe nanosheet ( $P \sim 40 \text{ fW}$ ,  $\lambda = 633 \text{ nm}$  and  $V_s = 2 \text{ V}$ ).

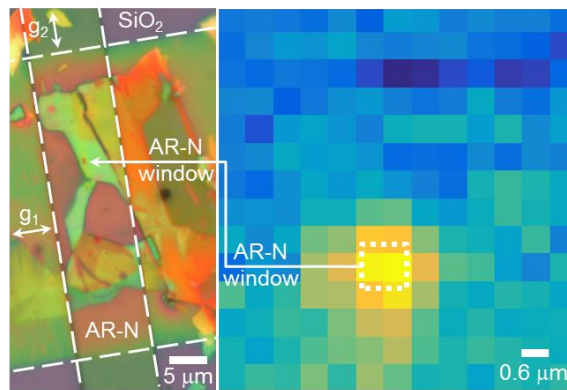


**Figure 7.12. Left:** optical image of a vertical heterostructure of device type B. **Right:** photocurrent map indicating that  $\Delta I$  arises primarily from the region of overlapping graphene electrodes separated by the  $L = 80 \text{ nm}$  InSe nanosheet ( $P \sim 100 \text{ fW}$ ,  $\lambda = 633 \text{ nm}$  and  $V_s = 2 \text{ V}$ ).

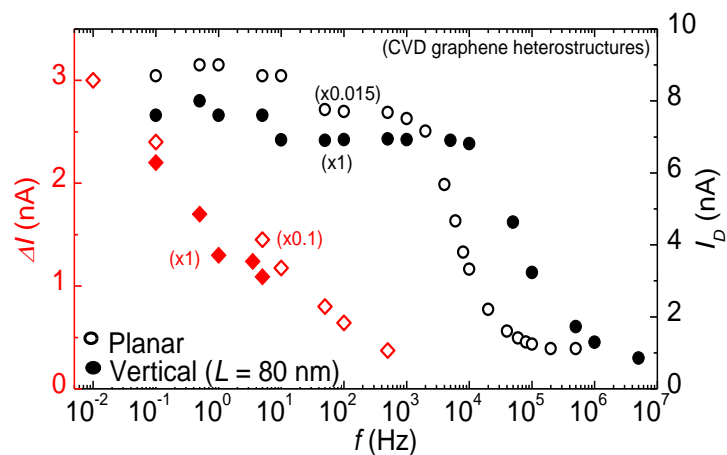


**Figure 7.13.** Temporal response of the dark current,  $I_D$ , (circles, right axis) and photocurrent,  $\Delta I$ , (diamonds, left axis) ( $P < 1 \text{ mW}$ ,  $\lambda = 633 \text{ nm}$  and  $V_s = 1 \text{ V}$ ) for the vertical (type B,  $L = 80 \text{ nm}$ , filled symbols) and planar (empty symbols) devices.  $I_D$  generated by an AC square-wave driving bias,  $V_s = \pm 1 \text{ V}$ .  $\Delta I$  generated by a mechanically chopped  $\lambda = 633 \text{ nm}$  laser beam of  $P_d < 0.1 \text{ Wcm}^{-2}$  and DC bias of  $V_b = 1 \text{ V}$ .

The vertical heterostructures are sensitive to lower incident powers than the planar structures (Figure 7.14). For device A (device B<sub>1</sub> with  $L = 80$  nm) we measure a photocurrent at  $P \sim 4 \times 10^{-14}$  W ( $1 \times 10^{-13}$  W) corresponding to a responsivity of  $R_\lambda \sim 3 \times 10^4$  AW<sup>-1</sup> ( $8 \times 10^3$  AW<sup>-1</sup>) and  $EQE \sim 5.9 \times 10^4$  ( $1.7 \times 10^4$ ) with minority carrier lifetime estimated to be  $\tau_t \sim 2 \times 10^{-8}$  s in both device types. The specific detectivity is estimated to be  $D^* \sim 1.1 \times 10^{13}$  m s<sup>-1/2</sup> W<sup>-1</sup> ( $1.1 \times 10^{15}$  Jones) for device A and  $D^* \sim 3.7 \times 10^{11}$  m s<sup>-1/2</sup> W<sup>-1</sup> ( $3.7 \times 10^{13}$  Jones) for device B<sub>1</sub>. A power law relation of the form  $R_\lambda = CP^{-n}$ , with  $n \sim 2/3$  and  $C$  is a constant, provides a good empirical fit to data of  $R$  for both types of vertical heterostructures.

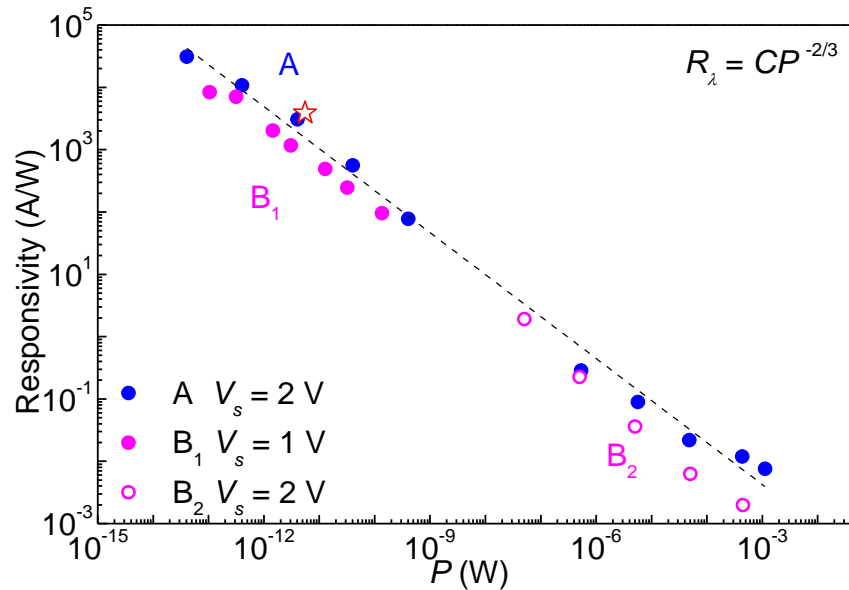


**Figure 7.14.** Comparison of the responsivity for the vertical graphene-InSe-graphene heterostructure devices of type A (blue) and type B (magenta), under optical illumination ( $\lambda = 633$  nm) at  $T = 300$  K. Devices B<sub>1</sub> and B<sub>2</sub> are based on InSe nanosheets with  $L = 130$  and  $80$  nm, respectively. The dashed line is an empirical power law of the form  $R_\lambda = CP^{-n}$  where  $n \sim 2/3$ . The maximum responsivity for the planar graphene-InSe-graphene heterostructure (red star,  $V_s = 2$  V) is included for comparison.

In terms of responsivity, our graphene-InSe devices outperform metal-semiconductor phototransistors based on the mono, di- and tri-chalcogenide layers,<sup>85</sup> in addition to bP based photodetectors.<sup>242</sup> For example, the monochalcogenides GaTe, GaS, GaSe, and elemental

bP report responsivities of  $\sim 10^4$ , 4.2 and 2.8, and 0.1  $\text{AW}^{-1}$ , respectively.<sup>90,108,109,148</sup> The highest responsivities for the di- and tri-chalcogenides are reported for  $\text{MoS}_2$  and  $\text{TiS}_3$  (both  $R_\lambda \sim 10^3 \text{AW}^{-1}$ ).<sup>260,261</sup> A large back-gate voltage ( $V_g \sim 40 \text{V}$ ) applied to  $\text{In}_2\text{Se}_3$  phototransistors can induce a larger photoresponsivity ( $R_\lambda \sim 10^5 \text{AW}^{-1}$ ) than shown for our graphene-InSe-graphene heterostructures, but at the expense of a much slower response time ( $\tau_r \sim 9\text{s}$ ).<sup>85</sup> Similar ultrahigh-gain and slow response times were demonstrated in hybrid graphene-quantum dot phototransistors with responsivities as high as  $\sim 5 \times 10^7 \text{AW}^{-1}$  and response times of the order of seconds, although they could be reduced to the millisecond scale through application of pulsed electric fields to empty charge traps.

Two reports in the literature also report on InSe-graphene heterostructures;<sup>111,257</sup> Chen *et al.* stamp anodic bonded graphene onto an exfoliated InSe nanosheet ( $L \sim 20 \text{nm}$ ) and report responsivities of  $R_\lambda = 940 \text{AW}^{-1}$  ( $\lambda = 532 \text{nm}$ ), attributing the large responsivity to the efficient extraction of photogenerated carriers by graphene.<sup>111</sup> Luo *et al.* produce a similar planar graphene-InSe-graphene heterostructure as presented in Section 7.3, but, opting to use a reversed configuration with CVD graphene being ‘micro-stamped’ onto exfoliated InSe nanosheets.<sup>257</sup> Comparatively, the responsivities in the latter devices are low ( $R_\lambda = 5.3 - 60 \text{AW}^{-1}$ ) and highlight the potential downfalls of unclean heterostructure interfaces, likely to be introduced through the transfer of CVD graphene involving polymers.

The characteristic optical response times of our graphene-InSe-graphene heterostructures ( $\tau_d, \tau_r \sim \text{ms}$ ) are around an order of magnitude faster, or at least on par, with similar metal-vdW semiconductor junctions.<sup>85</sup> In comparison, the minority carrier lifetimes are estimated from a semiclassical model (20-200 ns for the vertical and planar heterostructures, respectively) and are orders of magnitude

shorter than the optical response time of the graphene-InSe-graphene devices, which suggest the presence of trap states. As the photocurrent response is slower than the dark current response to an AC driving bias, trap states are likely to be filled during illumination and subsequently release carriers over much longer timescales than the minority carrier lifetime. The origin of the trap states is not immediately obvious, as they could be attributed to states within the InSe crystal and/or to surface/interface states introduced between InSe and graphene during the fabrication procedure. Recently, picosecond response times ( $\tau_r \sim 5.5$  ps) have been reported for ultraclean, graphene-WSe<sub>2</sub>-graphene vertical heterostructures encapsulated by hBN. However, the internal quantum efficiency quoted is comparatively low (IQE > 70%).<sup>256</sup> Assuming the photoresponsivity and optical response times in these graphene-WSe<sub>2</sub> devices are similarly described by the semiclassical model (equations 7.7-7.9), the relatively low photoresponse and fast response speed indicate ~ps lifetimes for the minority carrier lifetime, highlighting a trade-off between the potential photogain and response speed, controlled by the lifetime of the minority carriers within the semiconducting layer. For a comparison of vdW-SCs to more traditional SCs, the quoted responsivity and response times for a Si and InGaAs photodetector are  $R_{\text{Si}} \sim 2 \times 10^3$  AW<sup>-1</sup> and  $R_{\text{InGaAs}} \sim 7 \times 10^2$  AW<sup>-1</sup> with  $\tau_r \sim 8 \times 10^{-11}$  s for both device types.<sup>85</sup> The trade-off between high-gain and slow response, or vice versa (tuning is demonstrated between the two operating modes in In<sub>2</sub>Se<sub>3</sub> by back-gating),<sup>262</sup> appears to be a common characteristic for van der Waals semiconductors.<sup>85,242</sup> However, it is predicted that as fabrication processes advance, high-gain, fast response photodetectors will be realised; for example, patterning 2D materials with plasmonic nanostructures<sup>15,158,263</sup> or integrating with optical waveguides<sup>264,265</sup> and cavities<sup>266</sup> could provide routes to enhancing light absorption in fast response devices.

## 7.5 Summary

Our mechanically formed van der Waals heterostructures of InSe and graphene demonstrate a significantly large photoresponsivity, exceeding those reported for other vdW layered semiconductor crystals in both metal-SC and graphene-SC interface configurations. InSe offers a tunable and direct-gap photosensitive channel at the nanoscale, due to the retention of a direct-gap down to a thickness of a few nanometres, paralleled with a blue-shift in photon absorption and emission energies. Conversely, transition metal dichalcogenides, such as MoS<sub>2</sub> have a direct-band gap only in the monolayer form.<sup>8</sup> The enhanced detectivity of the heterojunctions is attributed to a favourable InSe/graphene band alignment, the formation of Ohmic contacts at the InSe-graphene interface, and a fast transit time of the electrons across the InSe channel.

Although a higher photoresponsivity ( $10^7$  AW<sup>-1</sup>) has been achieved in phototransistors based on graphene and colloidal nanocrystals,<sup>267</sup> the performance of such hybrid photodetectors tends to be compromised by a slow ( $\sim 1$ s) optical response due to the slow escape rate of photogenerated charges from the strongly confined nanocrystals. In contrast, for this work, the mechanism responsible for the photoresponse (photoconductive gain) does not rely on a charge trapping effect (photo-gating) as light generates free carriers in addition, the extraction of both electrons and holes at the graphene electrodes is facilitated by a low potential barrier at each InSe/graphene interface. These features enable relatively fast transit times for carriers and modulation of the dark and photocurrent at millisecond time scales. However, the additional processing steps involved in the fabrication of the vertical heterostructures are likely to introduce greater contact resistance through the presence of residual polymers, which is likely to inhibit charge transfer, slowing the device and reducing the overall responsivity. The likely presence of trap

states, as suggested by the optical temporal characteristics, may require further investigation in future experiments to determine any contribution to the overall photoresponse in these heterostructures. Nevertheless, the implementation of these fabrication processes to realise a working vdW heterostructure device represents significant progress and offers a route to device scalability using large area CVD graphene. Our innovative fabrication methods could be extended to similar material systems and more complex device architectures. Selective band alignments could be achieved by combining InSe with the other semiconducting monochalcogenides (*i.e.*, InX and GaX, where X = S, Se and Te) which cover a wide spectral range from the visible to near-infrared (0.5-1  $\mu\text{m}$ ), providing a class of 2D compounds for versatile band engineering. By demonstrating compatibility with transparent, conducting graphene, these new heterostructures and associated constituent layered components could be integrated into nanoscale electronic and optoelectronic devices with a range of materials including dielectrics, and transparent and flexible polymer substrates.

## Chapter 8

### Conclusions and future directions

The objectives of my PhD were to investigate the previously unknown properties of InSe nanosheets and to demonstrate the enhancement of graphene-based optoelectronics, through the fabrication and investigation of InSe-graphene van der Waals heterostructures. The key findings of my research are summarised as follows:

- (i) The formation of quantum well structures by InSe nanosheets results in tunable and direct radiative recombination at room temperature ( $E_g \sim 1.25 - 2.0$  eV for bulk to  $L \sim 2$  nm nanosheets).
- (ii) The quenching of luminescence intensity, observed in room and low temperature photoluminescence measurements, provides experimental evidence of a 'soft' direct-to-indirect band gap crossover in InSe as the monolayer limit is approached.
- (iii) The binding energy of photoexcited charge carriers, bound to unintentional donor and acceptor states in InSe nanosheets, are also susceptible to quantum confinement, generally increasing in energy with decreasing layer thickness and show a strong sensitivity to dopant position within the InSe nanolayer.
- (iv) Bulk-like exfoliated InSe layers can emit bright and relatively narrow ( $\sim 0.5$  meV) luminescence, alluding to spatial localisation of photoexcited carriers and 0D quantum dot emission from defect-related states.
- (v) A transfer of optical intensity from a low-to-high energy component under an applied magnetic field, advocates the

possibility of an indirect-to-direct band gap crossover, controlled by the application of an external magnetic field.

- (vi) The band alignment between InSe and graphene is highly favourable and facilitate the formation of Ohmic contacts. In combination with the relatively high electron mobility of InSe, this enables the realisation of InSe-graphene van der Waals heterostructures that are highly photosensitive to broad-band (NIR-to-VIS) electromagnetic radiation at room temperature.

## **8.1 Tuning the band gap of InSe nanosheets by quantum confinement**

Semiconductor quantum wells can be easily formed by mechanical exfoliation of layered crystals. In this study, I probed the thickness-dependent optical properties of InSe nanosheets at room temperature by micro-photoluminescence, Raman spectroscopy and atomic force microscopy. The studies revealed that the quantum confinement of charge carriers, in the axis perpendicular to the in-plane layers, results in a considerable blue-shift of the band gap energy; measured from  $h\nu \sim 1.25$  eV in bulk crystals to  $h\nu \sim 2.0$  eV in bilayer nanosheets. The energy blue-shift is accompanied by a significant decay of the luminescence intensity, as the nanosheet thickness is reduced, and provides experimental evidence of a 'soft' direct-to-indirect band gap crossover, as supported by density functional theory calculations of the band structure. The band structure calculations reveal the emergence of a 'Mexican hat' valence band energy dispersion, as the InSe nanosheet is reduced towards a single layer, accompanied by the development of a 1D-like Van Hove singularity in the 2D density of states.

InSe nanosheets thus exhibit a range of promising properties for developments in 2D optoelectronics: strong radiative recombination enables efficient device operation by allowing direct optical transitions; thickness-dependent band gap tuning offers spectral selectivity; and

the near-atomically flat surfaces, with a low density of dangling bonds, promotes the integration of InSe nanosheets into 2D van der Waals heterostructures, offering a substantial band engineering opportunities. These results are published in *Advanced Materials*, **25**, 5714 (2013).

## **8.2 Acceptor and donor states within InSe nanosheets**

Low temperature micro-photoluminescence measurements reveal photoexcited charge carriers bound at native donor and acceptors in exfoliated nanosheets of nominally undoped InSe. By comparing the temperature-dependent optical spectra to Varshni's empirical model, we were able to extract values for the binding energies of dopant-bound photoexcited carriers. The binding energies increase with decreasing nanosheet thickness, in addition to exhibiting a strong sensitivity to the position of the dopant within the InSe nanolayer, as determined by comparison of the extracted binding energies to a model of two-dimensional confinement of hydrogenic impurity states within a semiconductor quantum well.

Knowledge of how native and foreign impurity atoms can affect the overall optical and electronic properties of layered semiconductor nanosheets is of relevance to the performance of future 2D material technologies. Unintentional dopants can provide additional scattering events in 2D and quasi-2D systems: carrier localisation at strongly confined dopant states detrimentally affects device performances by reducing carrier mobility and trapping photogenerated carriers, resulting in slower device speeds and optoelectronic response times.<sup>17</sup> On the other hand, control over doping could be exploited; in particular, InSe can be hole-doped through introduction of Cd or Zn in the growth process and, assuming the doping does not significantly alter the electronic band structure, could provide a route to observing a Lifshitz transition associated with the 'Mexican hat' shaped valence band in

ultrathin InSe nanosheets. These studies are published in *Applied Physics Letters*, **105**, 221909 (2014).

### **8.3 Magneto-photoluminescence studies of exfoliated InSe**

We investigated the optical properties of exfoliated InSe layers at low temperature and under high magnetic fields in the Faraday geometry ( $T \sim 4.2$  K and  $B \leq 30$  T). Both broad ( $\sim 100$ 's meV) and narrow ( $\sim 0.5$  meV) optical emissions were observed in bulk-like multilayer InSe. The broad luminescence was attributed to donor and acceptor transitions while the narrow emission suggested in-plane spatial localisation of photogenerated carriers and defect-like quantum dot luminescence at defect-related states. The narrow emission in bulk-like exfoliated layers showed a weak response to the applied magnetic field, with small diamagnetic shifts ( $\delta E \sim 8$  meV at  $B = 30$  T) and no observable Zeeman splitting, consistent with the weak spin-orbit interaction expected in both bulk and atomically thin metal monochalcogenides.<sup>268</sup> For a thin InSe nanosheet, the external magnetic field was seen to distinctly modify the optical spectrum; with increasing magnetic field, the intensity of a low energy transition is transferred to a higher energy component, suggestive of an indirect-to-direct transition which can be controllably induced by the application of a magnetic field. Investigating controlled changes of the electronic band structure under high magnetic fields aids with the validation of theoretical models which predict novel functionality in 2D materials. Furthermore, the observation of sharp, 0D defect-like emission at low temperatures in InSe exfoliated multilayers could inspire the engineering of quantum dot-like features into the crystal structure, with a view to selectively tailor the optical properties.

## 8.4 InSe van der Waals heterostructures and devices

We investigated the optoelectronic properties of InSe-graphene van der Waals heterostructures. A novel approach to the fabrication of InSe-graphene heterojunctions was demonstrated by the incorporation of large-area graphene, grown by chemical vapour deposition, into a series of planar and vertical InSe-graphene heterostructures and characterised in comparison to the traditional mechanical stacking approach. The optoelectronic transport characteristics suggest a highly favourable band alignment between InSe and graphene (in contrast to the metal-semiconductor heterojunctions), which facilitate the efficient extraction of photogenerated charge carriers. Subsequently, the InSe-graphene heterostructures show a significantly high photoresponsivity ( $R_{\lambda} \sim 3 \times 10^4 \text{ AW}^{-1}$ ) and operate at relatively fast detection speeds ( $\sim \text{ms}$ ). These findings provide an early demonstration of the promising applications of nanoscale direct-gap III-VI compounds in 2D graphene-based optoelectronics. Additionally, by demonstrating that a favourable band alignment is formed with both exfoliated and CVD-grown graphene, it should be possible to develop this approach for the fabrication of devices which incorporate large-area growth of layered semiconductor crystals, opening a route to scalability. The results of this investigation are published in *Advanced Materials*, **27**, 3760 (2015) and *Journal of Physics: Conference Series*, **647**, 012001 (2015).

## 8.5 Future directions

### 8.5.1 Towards state-of-the-art III-VI compound devices

Prototype applications for InSe have already been demonstrated and include optoelectronic-memory large-scale image sensors<sup>269</sup> and heterostructures, such as, lateral *p-n* photovoltaic heterojunctions ( $R_{\lambda} \sim 4.2 \text{ AW}^{-1}$ )<sup>270</sup>, and III-VI crystal *p-n* light emitting diodes (LEDs).<sup>124</sup> Future devices could aim to build on these works, which have focussed on the thickness-dependent properties of electron transport in

nanoscale field-effect transistors and photogeneration of charge carriers in 2D and quasi-2D photodetector devices. Near-future improvements for such devices could be realised with the improvement of non-graphene-based contacts, such as the fabrication of edge or jagged contacts in contrast to top-contacts (*i.e.*, in-plane surface contacts). Palladium could be the material of choice for high-quality Ohmic contacts to InSe, as there may be a large overlapping of adjacent *d*-orbitals.<sup>247,271,272</sup> Future experiments on III-VI photodetectors could focus on time-resolved measurements in which the carrier lifetimes are measured. Results from such studies would provide valuable information in validating the mechanism for the high photoresponsivity observed, and could establish the maximum photogain and temporal response characteristics that may be reached in state-of-the-art-III-VI devices.

The band engineering demonstrated by early device studies often relies on the mechanical exfoliation of bulk materials and there is an immediate interest in developing synthesis techniques which enable the controllable and reproducible production of high-quality nanolayer materials. Bottom-up growth techniques offer promise for the production of large-area nanolayer crystals for application in functional devices which exploit the large surface-area-to-volume ratios of 2D materials, such as gas-sensing, solar energy harvesting, imaging arrays and transparent flexible electrodes. Several growth techniques for nanolayered III-VI compounds have been demonstrated including, physical vapour transport, chemical vapour deposition (CVD) and molecular beam epitaxy (MBE).<sup>100,104,105</sup> Recently, Balakrishnan *et al.*<sup>101</sup> have demonstrated the successful growth of nanoscale and 2D  $\beta$ -In<sub>2</sub>Se<sub>3</sub> layers by physical vapour transport, which exhibit a blue-shift in the photoluminescence emission when the thickness is reduced and show a relatively high photoresponsivity ( $R_\lambda = 2 \times 10^3 \text{ AW}^{-1}$ ). These works demonstrate that the observation and potential exploitation of

quantum mechanical effects can be realised through the growth of high quality layered semiconductor crystals.

As well as permitting control over the crystal-thickness, shape and size, large-area growth techniques offer further band engineering through the incorporation of foreign or native atoms with a view to doping and/or alloying crystals (*i.e.*,  $\text{GaTe} \rightarrow \text{GaTe}_x\text{Se}_{1-x} \rightarrow \text{GaSe}$ ).<sup>105,273</sup> Both molecular beam epitaxy and chemical vapour growth techniques have produced III-VI alloys, which exhibit a tunable band gap depending on the alloy concentration, in addition to any thickness related effects that promote further spectral selectivity.<sup>104,105</sup> Such techniques could be developed to controllably incorporate foreign dopants or intentional structural defects into layered materials, with a view to complement the 2D layers with 0D quantum dot functionality, for application in quantum information and optoelectronics through single photon detection and/or emission. The capability of layered semiconductors to display both 2D and 0D emission has been realised in exfoliated  $\text{WSe}_2$  nanosheets, by the presence of bright and narrow luminescence features with photon energies  $h\nu \sim 1.65 - 1.75$  eV at liquid-He temperatures.<sup>233-236</sup> More recently, similar features have been found in multilayer exfoliated hBN nanosheets at room temperature ( $h\nu \sim 2$  eV), suspected to arise from defect-related vacancies.<sup>274</sup>

Aside from thickness-dependent tuning, band engineering in 2D materials is enabled by an inherent mechanical robustness; compared to bulk graphite which can withstand elastic strain of around 0.1%,<sup>275</sup> single-layer graphene can accommodate more than 25%.<sup>276</sup> Similar values have been reported in layered semiconductors, which can mechanically deform by around 10% before rupturing and offer further tuning of the optical and electronic properties. A high elasticity and Young's Modulus<sup>18,19</sup> allow for the demonstration of strain-engineering in single layer  $\text{MoS}_2$ <sup>245,246</sup> and calculations predict applied strain could

induce a direct-to-indirect crossover, with excessive strain inducing a semiconductor-to-metal transition.<sup>277</sup>

### 8.5.2 Novel 2D functionalities

The intriguing electronic band structures of two-dimensional materials offer properties which provide both potential enhancements to modern technology and a range of novel functionalities. The multiple energy-degenerate valleys in the electronic band structure of TMDC monolayers earmark their applicability for the development of valleytronics;<sup>10,278–280</sup> where binary information is stored and manipulated as discrete values of crystal momentum, rather than as current flow or the spin state of the electron in electronics or spintronics, respectively. The metal monochalcogenides share common ‘Mexican hat’ shaped valence band energy dispersions, which extend across a significant proportion of the Brillouin zone and are accompanied by a 1D Van Hove singularity in the density of states.<sup>86,203,231</sup> Band structure calculations suggest that a high hole concentration could induce a Lifshitz transition in such systems and may be experimentally attainable through hole-doping of the semiconductor materials by the controlled inclusion of *p*-type impurities during crystal growth.<sup>231</sup> Alternatively, a transverse electric field could be used to control the hole concentration and devices employing ionic top-gates may be able to reach a sufficient hole density.<sup>65</sup> Works further investigating the intriguing properties of the electronic band structure in III-VI metal monochalcogenides, remark that a large density of states at or near the Fermi level can lead to further phenomena, such as 2D magnetism and superconductivity. The possibility of inducing tunable magnetism in GaSe monolayers by hole-doping (substitutional-As would provide *p*-type doping) or electrostatic-gating (ionic liquid) is discussed and the authors state the arguments extend to systems with similar band structures.<sup>202,204</sup> Observation of such phenomena experimentally, such as by the magneto-optical Kerr

effect or spin-polarised scanning tunnelling microscopy, could open the door to novel functional devices which enable fully polarised spin-transport with applications in spintronic technologies.<sup>202,204</sup> Magnetism in layered semiconductors can also be explored through the incorporation of magnetic dopants into the crystal structure, for example, stable exfoliable crystals of InSe have been successfully doped with Co, Mn and Fe impurities which may enable 2D magnetism in ultrathin layers. Further novel functionality is predicted for monolayer III-VI metal chalcogenides, which may exhibit piezoelectric effects (InSe:  $1.46 \text{ pmV}^{-1}$ ), similar to those reported for MoS<sub>2</sub> and hBN. Combined with the experimentally demonstrated ultrahigh photosensitivity, these systems yield the potential for unique electromechanical and optoelectronic functionalities on a common device platform.<sup>281</sup>

### **8.5.3 Advanced III-VI compound van der Waals heterostructures**

A host of van der Waals heterostructures, such as quasi-2D devices or superlattice-like structures are also likely to be explored as a way of realising novel functionalities.<sup>282</sup> The direct gap III-VI compound metal monochalcogenides hold promise for efficient optoelectronic devices and their compatibility with other 2D materials have been demonstrated. Future developments could parallel the works of Withers *et al.* with the fabrication of multilayer vertical van der Waals light-emitting diodes; these structures employed quantum wells of TMDCs bounded by insulating hBN into which electrons and holes were injected by ambipolar graphene, resulting in carrier recombination and the emission of photons from within the semiconducting layers.<sup>34</sup> The III-VI compounds of InSe, In<sub>2</sub>Se<sub>3</sub> and GaTe could realise multilayer LED structures with enhanced efficiencies due to the presence of a direct band gap, as well as offering greater tunable spectral selectivity.

III-VI compounds demonstrate atomically sharp interfaces with both van der Waals materials and traditional semiconductors, which alludes to their ease of integration with future technologies. As well as InSe, GaSe has demonstrated compatibility with graphene electrodes<sup>174</sup> and GaTe has been shown to form functional type-II ambipolar  $p$ - $n$  junctions with MoS<sub>2</sub> despite the marked differences between the irregular monoclinic and flat honeycomb crystal lattice geometries, respectively.<sup>283</sup> Beyond purely van der Waals crystal interfaces, MBE has been used to grow vertical heterostructures of GaSe and GaTe<sub>x</sub>Se<sub>1-x</sub> alloys on Si wafers that have an atomically sharp interface and operate as efficient photodiodes, with  $\mu$ s response times, and demonstrate the potential to integrate tunable III-VI compounds with state-of-the-art Si technologies.<sup>105,273</sup> Furthermore, the growth of large area vertical heterojunctions and superlattice-type layered semiconductor structures by MBE has been demonstrated providing a method of developing high-quality customisable vdW heterostructures for selective applications.<sup>284-286</sup>

Of novel interest in van der Waals heterostructures is the development of a range of unique band structures by the interaction of adjacent atomic planes. Despite the relatively straightforward mechanical formation of vdW heterostructures, a variety of subtle alignment parameters can lead to substantially complex heterostructure properties. Lattice mismatch at the heterointerfaces between traditional semiconductor crystals can lead to the formation of strain related defects and dislocations which can detrimentally affect the overall junction performance. In 2D artificially stacked heterostructures, a vdW gap can provide protection against such structural defects; yet, the lattice mismatch can still play a significant role in determining the final heterostructure properties. Moiré patterns are formed when two similar crystal lattices are stacked and, provided they are within suitable proximity, the electron orbitals which extend out

of the 2D plane interact with the charge carriers of the adjacent layers. The superlattice potential depends on both the lattice mismatch and rotational crystallographic alignment between the neighbouring crystals and can reconstruct the electronic energy spectrum creating a diverse hybrid system.<sup>3,26,27</sup> In particular, the crystallographic alignment can control whether the adjacent lattice stretches to adapt to a slightly different periodicity (at small angles) resulting in a commensurable state, or, undergoes limited adjustment resulting in an incommensurable state.<sup>287</sup>

The moiré patterns repeat on length scales longer than the individual lattice structures and have their own distinct properties; a new subset of Dirac cones are generated in hBN-graphene heterostructures (which have similar lattice parameters) and are observed to have their own highly degenerate Landau levels in magneto-transport measurements. Electrons traversing through the superlattice potential are further confined by magnetic fields which induce cyclotron motion; varying the magnetic field tunes the cyclotron orbits forming commensurate or incommensurate energy states, revealing the quantum fractal known as Hofstadter's butterfly.<sup>3,26,27,288,289</sup> Similar commensurable-induced effects have been predicted from first-principles calculations of MoS<sub>2</sub>-WS<sub>2</sub> monolayer heterojunctions. Individually, each TMDC layer is direct in monolayer form and indirect from bilayer onwards. However, a heterostructure bilayer of stacked monolayer MoS<sub>2</sub> and WS<sub>2</sub>, remains optically active due to the presence of a spatially misaligned direct gap in the modified electronic spectrum.<sup>290</sup> Additionally, in WSe<sub>2</sub>-MoS<sub>2</sub> heterolayers, the use of an intermediary hBN layer has experimentally demonstrated that the interlayer coupling can be readily tuned by intercalation of dielectric layers, providing yet another degree of control in the vdW heterostructure properties and a system in which to probe charge transfer between adjacent heterolayers.<sup>49</sup> For III-VI compounds, GaS-

GaSe monolayer stacked heterostructures are predicted to form a similar type-II band alignment, with enhanced charge separation characteristics, useful for applications in efficient photodetection or solar energy harvesting and could be further tuned through strain-engineering.<sup>22,282,291–293</sup>

#### 8.5.4 Phonon transport in III-VI compounds

Consideration of the phonon transport in layered semiconductor systems is also of great significance to device development. The thermal properties of crystals govern the dissipation of heat and, while high thermal conductivity (high dissipation) is advantageous in multi-layer FETs, photodetectors and LEDs, low thermal conductivity may be preferred for thin layer devices for energy efficient phase-change memory applications.<sup>129–133</sup> Recently, a thickness-dependence of the in-plane thermal conductivity was reported in suspended  $\text{In}_2\text{Se}_3$  nanolayers by micro-Raman spectroscopy and finite element analysis, showing the thermal conductivity to significantly decrease with reducing thickness, favouring the operation of nanoscale phase-change memory applications.<sup>294</sup> Other metal monochalcogenides are also being considered for their thermoelectric properties, with popular applications relating to energy (re)-harvesting.<sup>66</sup> In general, a good thermoelectric material is considered to have a high electrical conductivity ( $\sigma$ ), low thermal conductivity ( $\lambda_T$ ) and large Seebeck coefficient ( $S$ ), where the relation between these properties gives the thermoelectric efficiency  $ZT$ . The Van Hove singularity in the density of states near the band-edge in the metal monochalcogenides is expected to enhance  $ZT$ , for example sharp features in the DOS near the Fermi level are often indicative of materials with a large Seebeck coefficient.<sup>204</sup> Doping of InSe crystals with Sn is further expected to enhance the thermoelectric performance.<sup>295</sup> Beardsley *et al.* report on an approach to investigate phonon transport in III-VI semiconductor crystals by observing phonon resonances in InSe vdW crystals via picosecond acoustic pump-probe

techniques.<sup>296</sup> The mechanical vibrations of heterostructures can reveal information about the elastic bonds formed between the surface atoms at the interface between two materials, from which the phonon transport and thermal conductance properties can be inferred. Such information is critical for the development of nanoscale electroacoustic technologies operating at high (GHz-THz) frequencies.

### 8.5.5 Enabling 2D Dirac materials with III-VIs

Finally, there is an interest in the synthesis and investigation of the 2D elemental analogues of graphene.<sup>297</sup> Several 2D Dirac materials have been realised experimentally, mainly by MBE growth methods on metallic supporting substrates, such as Ag,<sup>298–301</sup> Au<sup>302</sup> and Bi<sub>2</sub>Te<sub>3</sub>.<sup>303</sup> Despite having no exfoliable bulk counterpart, 2D silicene,<sup>299–301</sup> germanene,<sup>302,304,305</sup> stanene,<sup>303</sup> and borophene<sup>298</sup> have all been synthesised.<sup>11</sup> Theoretical predictions of the properties of atomically thin arsenene, antimonene and aluminene are also gathering interest.<sup>306–309</sup> Recently, the hexagonal honeycomb lattice, common to the metal chalcogenide semiconductors, was shown to be suitable for the growth of silicene, germanene and stanene, which in free-standing form, are calculated to have Dirac cone-like electronic band structures.<sup>310–312</sup> These materials are predicted to have similar properties to graphene, for example the carrier mobility in germanene is predicted to be twice as large in comparison. On the other hand, in contrast to the flat basal plane of graphene, the lattice structures of silicene, germanene and stanene are buckled and consist of two vertically displaced sublattices of atoms. Such lattice geometries result in material properties which differ from graphene, such as the presence of significantly stronger spin-orbit coupling and electric-field induced band gaps, which have applications in electronics and spintronics. In particular, the strong spin-orbit coupling in silicene (1.55 meV),<sup>310,313</sup> germanene (23.9 meV)<sup>310,313</sup> and stanene (73.5 meV)<sup>310</sup> could enable the observation of the quantum spin Hall effect at experimentally

accessible temperatures; as originally predicted for graphene ( $8 \mu\text{eV}$ )<sup>310,314</sup> and only seen thus far in HgTe-CdTe quantum wells,<sup>315,316</sup> and could lead to the realisation of dissipation-less spintronic devices.<sup>303,310,317,318</sup> Functionalised stanene sheets, *i.e.*, stanane - the hydrogenated or iodised derivatives of stanene - are predicted to possess a spin-orbit coupling gap of 0.3 eV.<sup>319</sup> For the calculations to be verified, these elemental 2D Dirac systems need to be investigated experimentally. The first silicene transistors have been demonstrated to operate at room temperature and show promising proof-of-concept characteristics, which are expected to be improved upon and include, Dirac-like ambipolar charge transport, carrier mobility of  $\mu \sim 100 \text{ cm}^2\text{V}^{-1}\text{s}^{-1}$  and the opening of a small ( $\sim 210 \text{ meV}$ ) band gap.<sup>320</sup> Unfortunately, the free-standing electronic properties of germanene and stanene/stanane single-layer sheets have yet to be investigated due to strong interactions from the growth substrates, which act to disturb the Dirac cones and facilitate interlayer charge transfer, causing metallicity phenomena.<sup>317,318</sup> Similar effects are seen in other Dirac materials.<sup>303,317,321,322</sup> The III-VI metal monochalcogenides have been identified as promising substrates for the growth of germanene and stanene/stanane as they would have favourably weak interactions with the grown 2D layers.<sup>317,318,322</sup> In particular, InSe is predicted to form a commensurable van der Waals heterostructure with stanene, which could be able to exhibit quasi-free standing features, with comparable spin-orbit coupling gaps. Similar features are calculated to be retained in germanene-InSe heterostructures, which are predicted to exhibit a semiconducting nature with band gap over 0.1 eV,  $\mu \sim 1.5 - 2.2 \times 10^5 \text{ cm}^2\text{V}^{-1}\text{s}^{-1}$  and spin-orbit coupling of 42 meV.<sup>318</sup> Future investigations into the realisation of InSe germanene and stanane/stanene FETs could be developed to realise novel 2D electronic and spintronic devices, further

demonstrating the considerable potential of InSe and the III-VI metal monochalcogenides within the 2D material field.<sup>322</sup>

## Bibliography

1. Novoselov, K. S. *et al.* Electric field effect in atomically thin carbon films. *Science* **306**, 666–9 (2004).
2. Novoselov, K. S. *et al.* Two-dimensional atomic crystals. *Proc. Natl. Acad. Sci. U. S. A.* **102**, 10451–3 (2005).
3. Geim, A. K. & Grigorieva, I. V. Van der Waals heterostructures. *Nature* **499**, 419–25 (2013).
4. Watanabe, K., Taniguchi, T. & Kanda, H. Direct-bandgap properties and evidence for ultraviolet lasing of hexagonal boron nitride single crystal. *Nat. Mater.* **3**, 404–9 (2004).
5. Cassabois, G., Valvin, P. & Gil, B. Hexagonal boron nitride is an indirect bandgap semiconductor. *Nat. Photonics* (2016). doi:10.1038/nphoton.2015.277
6. Morozov, S. *et al.* Two-dimensional electron and hole gases at the surface of graphite. *Phys. Rev. B* **72**, 201401 (2005).
7. Splendiani, A. *et al.* Emerging photoluminescence in monolayer MoS<sub>2</sub>. *Nano Lett.* **10**, 1271–5 (2010).
8. Mak, K. F., Lee, C., Hone, J., Shan, J. & Heinz, T. F. Atomically Thin MoS<sub>2</sub>: A New Direct-Gap Semiconductor. *Phys. Rev. Lett.* **105**, 136805 (2010).
9. Radisavljevic, B., Radenovic, A., Brivio, J., Giacometti, V. & Kis, A. Single-layer MoS<sub>2</sub> transistors. *Nat. Nanotechnol.* **6**, 147–50 (2011).
10. Cao, T. *et al.* Valley-selective circular dichroism of monolayer molybdenum disulfide. *Nat. Commun.* **3**, 887 (2012).
11. Liu, H. *et al.* Phosphorene: An Unexplored 2D Semiconductor with a High Hole Mobility. *ACS Nano* **8**, 4033–4041 (2014).

12. Zhang, H. *et al.* Topological insulators in  $\text{Bi}_2\text{Se}_3$ ,  $\text{Bi}_2\text{Te}_3$  and  $\text{Sb}_2\text{Te}_3$  with a single Dirac cone on the surface. *Nat. Phys.* **5**, 438–442 (2009).
13. Staley, N. E. *et al.* Electric field effect on superconductivity in atomically thin flakes of  $\text{NbSe}_2$ . *Phys. Rev. B* **80**, 184505 (2009).
14. Cao, Y. *et al.* Quality Heterostructures from Two-Dimensional Crystals Unstable in Air by Their Assembly in Inert Atmosphere. *Nano Lett.* **15**, 4914–21 (2015).
15. Britnell, L. *et al.* Strong light-matter interactions in heterostructures of atomically thin films. *Science* **340**, 1311–4 (2013).
16. Carvalho, A., Ribeiro, R. M. & Castro Neto, A. H. Band nesting and the optical response of two-dimensional semiconducting transition metal dichalcogenides. *Phys. Rev. B* **88**, 115205 (2013).
17. Li, S.-L., Tsukagoshi, K., Orgiu, E. & Samorì, P. Charge transport and mobility engineering in two-dimensional transition metal chalcogenide semiconductors. *Chem. Soc. Rev.* **45**, 118–51 (2015).
18. Castellanos-Gomez, A. *et al.* Mechanical properties of freely suspended semiconducting graphene-like layers based on  $\text{MoS}_2$ . *Nanoscale Res. Lett.* **7**, 233 (2012).
19. Castellanos-Gomez, A. *et al.* Elastic properties of freely suspended  $\text{MoS}_2$  nanosheets. *Adv. Mater.* **24**, 772–5 (2012).
20. Ferrari, A. C. Science and technology roadmap for graphene, related two-dimensional crystals, and hybrid systems. *Nanoscale* **7**, 4598–4810 (2014).
21. Georgiou, T. *et al.* Vertical field-effect transistor based on graphene- $\text{WS}_2$  heterostructures for flexible and transparent electronics. *Nat. Nanotechnol.* **8**, 100–3 (2013).

22. Mishchenko, A. *et al.* Twist-controlled resonant tunnelling in graphene/boron nitride/graphene heterostructures. *Nat. Nanotechnol.* **9**, 808–13 (2014).
23. Ross, J. S. *et al.* Electrically tunable excitonic light-emitting diodes based on monolayer WSe<sub>2</sub> p-n junctions. *Nat. Nanotechnol.* **9**, 268–72 (2014).
24. Xue, J. *et al.* Scanning tunnelling microscopy and spectroscopy of ultra-flat graphene on hexagonal boron nitride. *Nat. Mater.* **10**, 282–5 (2011).
25. Yankowitz, M. *et al.* Emergence of superlattice Dirac points in graphene on hexagonal boron nitride. *Nat. Phys.* **8**, 382–386 (2012).
26. Ponomarenko, L. A. *et al.* Cloning of Dirac fermions in graphene superlattices. *Nature* **497**, 594–7 (2013).
27. Dean, C. R. *et al.* Hofstadter's butterfly and the fractal quantum Hall effect in moiré superlattices. *Nature* **497**, 598–602 (2013).
28. Hunt, B. *et al.* Massive Dirac fermions and Hofstadter butterfly in a van der Waals heterostructure. *Science* **340**, 1427–30 (2013).
29. Xia, F., Wang, H., Xiao, D., Dubey, M. & Ramasubramaniam, A. Two-dimensional material nanophotonics. *Nat. Photonics* **8**, 899–907 (2014).
30. Dean, C. R. *et al.* Boron nitride substrates for high-quality graphene electronics. *Nat. Nanotechnol.* **5**, 722–6 (2010).
31. Mayorov, A. S. *et al.* Micrometer-scale ballistic transport in encapsulated graphene at room temperature. *Nano Lett.* **11**, 2396–9 (2011).
32. Britnell, L. *et al.* Strong light-matter interactions in heterostructures of atomically thin films. *Science* **340**, 1311–4

- (2013).
33. Georgiou, T. *et al.* Vertical field-effect transistor based on graphene-WS<sub>2</sub> heterostructures for flexible and transparent electronics. *Nat. Nanotechnol.* **8**, 100–3 (2013).
  34. Withers, F. *et al.* Light-emitting diodes by band-structure engineering in van der Waals heterostructures. *Nat. Mater.* **14**, 301–6 (2015).
  35. Koppens, F. H. L. *et al.* Photodetectors based on graphene, other two-dimensional materials and hybrid systems. *Nat. Nanotechnol.* **9**, 780–793 (2014).
  36. Castro Neto, A. H., Peres, N. M. R., Novoselov, K. S. & Geim, A. K. The electronic properties of graphene. *Rev. Mod. Phys.* **81**, 109–162 (2009).
  37. Novoselov, K. S. *et al.* Two-dimensional gas of massless Dirac fermions in graphene. *Nature* **438**, 197 (2005).
  38. Zhang, Y., Tan, Y.-W., Stormer, H. L. & Kim, P. Experimental observation of the quantum Hall effect and Berry's phase in graphene. *Nature* **438**, 201–4 (2005).
  39. Geim, A. K. & Novoselov, K. S. The rise of graphene. *Nat. Mater.* **6**, 183–91 (2007).
  40. Baringhaus, J. *et al.* Exceptional ballistic transport in epitaxial graphene nanoribbons. *Nature* **506**, 349–54 (2014).
  41. Balandin, A. A. Thermal properties of graphene and nanostructured carbon materials. *Nat. Mater.* **10**, 569–81 (2011).
  42. Lee, C., Wei, X., Kysar, J. W. & Hone, J. Measurement of the elastic properties and intrinsic strength of monolayer graphene. *Science* **321**, 385–8 (2008).
  43. Moser, J., Barreiro, A. & Bachtold, A. Current-induced cleaning of

- graphene. *Appl. Phys. Lett.* **91**, 163513 (2007).
44. Nair, R. R., Wu, H. A., Jayaram, P. N., Grigorieva, I. V. & Geim, A. K. Unimpeded Permeation of Water Through Helium-Leak-Tight Graphene-Based Membranes. *Science (80-. )*. **335**, 442–444 (2012).
  45. Nair, R. R. *et al.* Fine structure constant defines visual transparency of graphene. *Science* **320**, 1308 (2008).
  46. Bunch, J. S. *et al.* Impermeable atomic membranes from graphene sheets. *Nano Lett.* **8**, 2458–62 (2008).
  47. Consadori, F. & Frindt, R. Crystal Size Effects on the Exciton Absorption Spectrum of WSe<sub>2</sub>. *Phys. Rev. B* **2**, 4893–4896 (1970).
  48. Zhao, W. *et al.* Evolution of Electronic Structure in Atomically Thin Sheets of WS<sub>2</sub> and WSe<sub>2</sub>. *ACS Nano* **7**, 791–797 (2013).
  49. Fang, H. *et al.* Strong interlayer coupling in van der Waals heterostructures built from single-layer chalcogenides. *Proc. Natl. Acad. Sci. U. S. A.* **111**, 6198–202 (2014).
  50. Tongay, S. *et al.* Thermally driven crossover from indirect toward direct bandgap in 2D semiconductors: MoSe<sub>2</sub> versus MoS<sub>2</sub>. *Nano Lett.* **12**, 5576–80 (2012).
  51. Larentis, S., Fallahazad, B. & Tutuc, E. Field-effect transistors and intrinsic mobility in ultra-thin MoSe<sub>2</sub> layers. *Appl. Phys. Lett.* **101**, 223104 (2012).
  52. Tonndorf, P. *et al.* Photoluminescence emission and Raman response of monolayer MoS<sub>2</sub>, MoSe<sub>2</sub>, and WSe<sub>2</sub>. *Opt. Express* **21**, 4908–16 (2013).
  53. Srivastava, A. *et al.* Valley Zeeman effect in elementary optical excitations of monolayer WSe<sub>2</sub>. *Nat. Phys.* **11**, 141–147 (2015).

54. Harper, P. G. & Hilder, J. A. Exciton spectra in thin crystals. *Phys. status solidi* **26**, 69–76 (1968).
55. Castellanos-Gomez, A. *et al.* Isolation and characterization of few-layer black phosphorus. *2D Mater.* **1**, 025001 (2014).
56. Splendiani, A. *et al.* Emerging Photoluminescence in Monolayer MoS<sub>2</sub>. *Nano Lett.* **10**, 1271–1275 (2012).
57. Qiao, J., Kong, X., Hu, Z.-X., Yang, F. & Ji, W. High-mobility transport anisotropy and linear dichroism in few-layer black phosphorus. *Nat. Commun.* **5**, 4475 (2014).
58. Tran, V., Soklaski, R., Liang, Y. & Yang, L. Layer-controlled band gap and anisotropic excitons in few-layer black phosphorus. *Phys. Rev. B* **89**, 235319 (2014).
59. Wang, X. *et al.* Highly anisotropic and robust excitons in monolayer black phosphorus. *Nat. Nanotechnol.* **10**, 517–521 (2015).
60. Yang, J. *et al.* Optical tuning of exciton and trion emissions in monolayer phosphorene. *Light Sci. Appl.* **4**, e312 (2015).
61. Rudenko, A. N. & Katsnelson, M. I. Quasiparticle band structure and tight-binding model for single- and bilayer black phosphorus. *Phys. Rev. B* **89**, 201408 (2014).
62. Mak, K. F. *et al.* Atomically Thin MoS<sub>2</sub>: A New Direct-Gap Semiconductor. *Phys. Rev. Lett.* **105**, 136805 (2010).
63. Yun, W. S., Han, S. W., Hong, S. C., Kim, I. G. & Lee, J. D. Thickness and strain effects on electronic structures of transition metal dichalcogenides: 2H-MX<sub>2</sub> semiconductors ( M = Mo, W; X = S, Se, Te). *Phys. Rev. B* **85**, 033305 (2012).
64. Li, S.-L. *et al.* Thickness-dependent interfacial Coulomb scattering in atomically thin field-effect transistors. *Nano Lett.* **13**, 3546–52 (2013).

65. Debbichi, L., Eriksson, O. & Lebègue, S. Two-Dimensional Indium Selenides Compounds: An Ab Initio Study. *J. Phys. Chem. Lett.* **6**, 3098–103 (2015).
66. Han, G., Chen, Z.-G., Drennan, J. & Zou, J. Indium Selenides: Structural Characteristics, Synthesis and Their Thermoelectric Performances. *Small* **10**, 2747–2765 (2014).
67. Lei, S. *et al.* Evolution of the electronic band structure and efficient photo-detection in atomic layers of InSe. *ACS Nano* **8**, 1263–72 (2014).
68. Bringuier, E., Bourdon, A., Piccioli, N. & Chevy, A. Optical second-harmonic generation in lossy media: Application to GaSe and InSe. *Phys. Rev. B* **49**, 16971–16982 (1994).
69. Manjo, F. J., Mun, V., Segura, A., Bouvier, J. & Andre, M. V. Strong optical nonlinearities in gallium and indium selenides related to inter-valence-band transitions induced by light pulses. **56**, (1997).
70. Sánchez-Royo, J. F., Segura, A. & Muñoz, V. Anisotropy of the refractive index and absorption coefficient in the layer plane of gallium telluride single crystals. *Phys. Status Solidi* **151**, 257–265 (1995).
71. Ferrer-Roca, C., Bouvier, J., Segura, A., Andrés, M. V. & Muñoz, V. Light-induced transmission nonlinearities in gallium selenide. *J. Appl. Phys.* **85**, 3780 (1999).
72. Kaindl, R. A., Eickemeyer, F., Woerner, M. & Elsaesser, T. Broadband phase-matched difference frequency mixing of femtosecond pulses in GaSe: Experiment and theory. *Appl. Phys. Lett.* **75**, 1060 (1999).
73. Allakhverdiev, K. R., Yetis, M. Ö., Özbek, S., Baykara, T. K. & Salaev, E. Y. Effective nonlinear GaSe crystal. Optical properties and applications. *Laser Phys.* **19**, 1092–1104 (2009).
74. Segura, A., Bouvier, J., Andrés, M. V., Manjón, F. J. & Muñoz, V. Strong optical nonlinearities in gallium and indium selenides

- related to inter-valence-band transitions induced by light pulses. *Phys. Rev. B* **56**, 4075–4084 (1997).
75. Segura, A., Guesdon, J. P., Besson, J. M. & Chevy, A. Photoconductivity and photovoltaic effect in indium selenide. *J. Appl. Phys.* **54**, 876 (1983).
  76. Martínez-Pastor, J., Segura, A., Valdés, J. L. & Chevy, A. Electrical and photovoltaic properties of indium-tin-oxide/p-InSe/Au solar cells. *J. Appl. Phys.* **62**, 1477 (1987).
  77. Segura, A., Chevy, A., Guesdon, J. P. & Besson, J. M. Photovoltaic efficiency of InSe solar cells. *Sol. Energy Mater.* **2**, 159–165 (1979).
  78. Segura, A., Guesdon, J. P., Besson, J. M. & Chevy, A. Photovoltaic effect in InSe - Application to Solar Energy Conversion. *Rev. Phys. Appliquée* **14**, 253–257 (1979).
  79. Segura, A., Besson, J. M., Chevy, A. & Martin, M. S. Photovoltaic properties of GaSe and InSe junctions. *Nuovo Cim. B Ser. 11* **38**, 345–351 (2007).
  80. Sánchez-Royo, J. F. *et al.* Optical and photovoltaic properties of indium selenide thin films prepared by van der Waals epitaxy. *J. Appl. Phys.* **90**, 2818 (2001).
  81. Sánchez-Royo, J. F. *et al.* Photovoltaic properties of indium selenide thin films prepared by van der Waals epitaxy. *Thin Solid Films* **307**, 283–287 (1997).
  82. Shi, W. & Ding, Y. J. A monochromatic and high-power terahertz source tunable in the ranges of 2.7–38.4 and 58.2–3540  $\mu\text{m}$  for variety of potential applications. *Appl. Phys. Lett.* **84**, 1635 (2004).
  83. Shi, W., Ding, Y. J., Fernelius, N. & Vodopyanov, K. Efficient, tunable, and coherent 0.18-5.27-THz source based on GaSe crystal. *Opt. Lett.* **27**, 1454–1456 (2002).

84. Kübler, C., Huber, R., Tübel, S. & Leitenstorfer, A. Ultrabroadband detection of multi-terahertz field transients with GaSe electro-optic sensors: Approaching the near infrared. *Appl. Phys. Lett.* **85**, 3360 (2004).
85. Buscema, M. *et al.* Photocurrent generation with two-dimensional van der Waals semiconductors. *Chem. Soc. Rev.* **44**, 3691–718 (2015).
86. Zólyomi, V., Drummond, N. D. & Fal'ko, V. I. Band structure and optical transitions in atomic layers of hexagonal gallium chalcogenides. *Phys. Rev. B* **87**, 195403 (2013).
87. Ho, C. H. & Lin, S. L. Optical properties of the interband transitions of layered gallium sulfide. *J. Appl. Phys.* **100**, 083508 (2006).
88. Rybkovskiy, D. V., Osadchy, A. V. & Obratsova, E. D. Transition from parabolic to ring-shaped valence band maximum in few-layer GaS, GaSe, and InSe. *Phys. Rev. B* **90**, 235302 (2014).
89. Rybkovskiy, D. V. *et al.* Size-induced effects in gallium selenide electronic structure: The influence of interlayer interactions. *Phys. Rev. B* **84**, 085314 (2011).
90. Hu, P., Wen, Z., Wang, L., Tan, P. & Xiao, K. Synthesis of few-layer GaSe nanosheets for high performance photodetectors. *ACS Nano* **6**, 5988–94 (2012).
91. Chikan, V. & Kelley, D. F. Synthesis of Highly Luminescent GaSe Nanoparticles. *Nano Lett.* **2**, 141–145 (2002).
92. Late, D. J. *et al.* Rapid Characterization of Ultrathin Layers of Chalcogenides on SiO<sub>2</sub>/Si Substrates. *Adv. Funct. Mater.* **22**, 1894–1905 (2012).
93. Zhou, Y. *et al.* Epitaxy and photoresponse of two-dimensional GaSe crystals on flexible transparent mica sheets. *ACS Nano* **8**, 1485–90 (2014).

94. Rodriguez, R. D. *et al.* Selective Raman modes and strong photoluminescence of gallium selenide flakes on  $sp^2$  carbon. *J. Vac. Sci. Technol. B Microelectron. Nanom. Struct.* **32**, 04E106 (2014).
95. Coleman, J. N. *et al.* Two-dimensional nanosheets produced by liquid exfoliation of layered materials. *Science* **331**, 568–71 (2011).
96. Nicolosi, V., Chhowalla, M., Kanatzidis, M. G., Strano, M. S. & Coleman, J. N. Liquid Exfoliation of Layered Materials. *Science* (80-. ). **340**, 1226419–1226419 (2013).
97. Lei, S. *et al.* Synthesis and photoresponse of large GaSe atomic layers. *Nano Lett.* **13**, 2777–81 (2013).
98. Li, X. *et al.* Controlled vapor phase growth of single crystalline, two-dimensional GaSe crystals with high photoresponse. *Sci. Rep.* **4**, 5497 (2014).
99. Wang, Z. *et al.* High-performance flexible photodetectors based on GaTe nanosheets. *Nanoscale* **7**, 7252–7258 (2015).
100. Huang, W., Gan, L., Li, H., Ma, Y. & Zhai, T. 2D layered group IIIA metal chalcogenides: synthesis, properties and applications in electronics and optoelectronics. *CrystEngComm* (2016). doi:10.1039/C5CE01986A
101. Balakrishnan, N. *et al.* Quantum confinement in  $\beta$ - $\text{In}_2\text{Se}_3$  layers grown by physical vapour transport for high responsivity photodetectors. (2016).
102. Bonaccorso, F. *et al.* Production and processing of graphene and 2d crystals. *Mater. Today* **15**, 564–589 (2012).
103. Najmaei, S. *et al.* Vapour phase growth and grain boundary structure of molybdenum disulphide atomic layers. *Nat. Mater.* **12**, 754–9 (2013).
104. Wu, C.-H. *et al.* Epitaxial single-crystal of GaSe epilayers grown

- on a c-sapphire substrate by molecular beam epitaxy. *Phys. status solidi* **212**, 2201–2204 (2015).
105. Yuan, X. *et al.* Arrayed van der Waals Vertical Heterostructures Based on 2D GaSe Grown by Molecular Beam Epitaxy. *Nano Lett.* **15**, 3571–7 (2015).
  106. Camassel, J., Merle, P., Mathieu, H. & Chevy, A. Excitonic absorption edge of indium selenide. *Phys. Rev. B* **17**, 4718–4725 (1978).
  107. Jacobs-Gedrim, R. B. *et al.* Extraordinary photoresponse in two-dimensional In<sub>2</sub>Se<sub>3</sub> nanosheets. *ACS Nano* **8**, 514–21 (2014).
  108. Hu, P. *et al.* Highly responsive ultrathin GaS nanosheet photodetectors on rigid and flexible substrates. *Nano Lett.* **13**, 1649–54 (2013).
  109. Liu, F. *et al.* High-Sensitivity Photodetectors Based on Multilayer GaTe Flakes. *ACS Nano* **8**, 752–60 (2014).
  110. Feng, W., Zhou, X., Tian, W. Q., Zheng, W. & Hu, P. Performance improvement of multilayer InSe transistors with optimized metal contacts. *Phys. Chem. Chem. Phys.* **17**, 3653–3658 (2015).
  111. Chen, Z., Biscaras, J. & Shukla, A. A high performance graphene/few-layer InSe photo-detector. *Nanoscale* **7**, 5981–6 (2015).
  112. Brebner, S. J. J. L. Group Theoretical Analysis of Lattice Vibrations in GaSe Polytypes. *Can. J. Phys.* **52**, 2454 – 2458 (2011).
  113. Ashokan, S. *et al.* Resonant Raman scattering in quasi-two-dimensional InSe near the Mo and M, critical points. *Phys. Rev. B* **44**, 133–142 (1991).
  114. Basinski, Z. S., Dove, D. B. & Mooser, E. Interacting Partial Dislocations in GaSe. *J. Appl. Phys.* **34**, 469 (1963).

115. Dmitriev, A. . *et al.* N-shaped volt-ampere characteristics of InSe single crystals at low temperatures. *Solid State Commun.* **75**, 465–467 (1990).
116. Bakhtinov, A. P. *et al.* Formation of nanostructure on the surface of layered InSe semiconductor caused by oxidation under heating. *Phys. Solid State* **49**, 1572–1578 (2007).
117. Dmitriev, A. I. *et al.* Neutron diffraction studies of the negative thermal expansion in a layered indium selenide crystal. *Phys. Solid State* **51**, 2342–2346 (2009).
118. Volykhov, A. A. *et al.* Study of the atomically clean InSe(0001) surface by X-ray photoelectron spectroscopy. *Russ. Microelectron.* **41**, 521–526 (2012).
119. Dmitriev, A. I. *et al.* Investigation of the morphology of the van der Waals surface of the InSe single crystal. *Phys. Solid State* **53**, 622–633 (2011).
120. Savitskii, P. I., Mintyanskii, I. V. & Kovalyuk, Z. D. Annealing effect on conductivity anisotropy in indium selenide single crystals. *Phys. Status Solidi* **155**, 451–460 (1996).
121. Millot, M., Broto, J.-M., George, S., González, J. & Segura, A. Electronic structure of indium selenide probed by magnetoabsorption spectroscopy under high pressure. *Phys. Rev. B* **81**, 205211 (2010).
122. Pomer, F. *et al.* Electrical Conductivity Anisotropy in Tin-Doped n-Type Indium Selenide. *Phys. status solidi* **145**, 261–268 (1988).
123. Katerinchuk, V. N., Kovalyuk, Z. D., Netyaga, V. V. & Betsa, T. V. Heterojunctions Produced from the Layered Semiconductors SnS<sub>1.9</sub>Se<sub>0.1</sub> and GaSe <Cd> . *Inorg. Mater.* **37**, 336–338 (2000).
124. Balakrishnan, N. *et al.* Room Temperature Electroluminescence from Mechanically Formed van der Waals III-VI Homojunctions

- and Heterojunctions. *Adv. Opt. Mater.* **2**, 1064–1069 (2014).
125. Liu, F. *et al.* High-sensitivity photodetectors based on multilayer GaTe flakes. *ACS Nano* **8**, 752–60 (2014).
  126. Zhang, X., Tan, Q.-H., Wu, J.-B., Shi, W. & Tan, P. Review on the Raman spectroscopy of different types of layered materials. *Nanoscale* (2016). doi:10.1039/C5NR07205K
  127. Hu, P. *et al.* Highly sensitive phototransistors based on two-dimensional GaTe nanosheets with direct bandgap. *Nano Res.* **7**, 694–703 (2014).
  128. Ho, C.-H. *et al.* Surface oxide effect on optical sensing and photoelectric conversion of  $\alpha$ - $\text{In}_2\text{Se}_3$  hexagonal microplates. *ACS Appl. Mater. Interfaces* **5**, 2269–77 (2013).
  129. Julien, C., Eddrief, M., Balkanski, M., Hatzikraniotis, E. & Kambas, K. Electrical transport properties of  $\text{In}_2\text{Se}_3$ . *Phys. status solidi* **88**, 687–695 (1985).
  130. De Blasi, C., Drigo, A. V., Micocci, G., Tepore, A. & Mancini, A. M. Preparation and characterization of  $\text{In}_2\text{Se}_3$  crystals. *J. Cryst. Growth* **94**, 455–458 (1989).
  131. Lu, C.-Y. *et al.* Laser and electrical current induced phase transformation of  $\text{In}_2\text{Se}_3$  semiconductor thin film on Si(111). *Appl. Phys. A* **93**, 93–98 (2008).
  132. Jasinski, J. & Swider, W. Crystal structure of  $\kappa$ - $\text{In}_2\text{Se}_3$ . *Appl. Phys. Lett.* **81**, 4356 (2002).
  133. Groot, C. De & Moodera, J. Growth and characterization of a novel  $\text{In}_2\text{Se}_3$  structure. *J. Appl Phys.* **89**, 4336 (2001).
  134. Verble, J. & Wieting, T. Lattice Mode Degeneracy in  $\text{MoS}_2$  and Other Layer Compounds. *Phys. Rev. Lett.* **25**, 362 (1970).
  135. Loudon, R. The Raman effect in crystals. *Adv. Phys.* **50**, 813–

864 (2001).

136. Smith, E. & Dent, G. *Modern Raman Spectroscopy - A Practical Approach*. (John Wiley & Sons, 2005). doi:10.1002/0470011831
137. Zhang, X. *et al.* Phonon and Raman scattering of two-dimensional transition metal dichalcogenides from monolayer, multilayer to bulk material. *Chem. Soc. Rev.* **44**, 2757–85 (2015).
138. Huang, H. *et al.* Highly sensitive phototransistor based on GaSe nanosheets. *Appl. Phys. Lett.* **107**, 143112 (2015).
139. Late, D. J. *et al.* GaS and GaSe Ultrathin Layer Transistors. *Adv. Mater.* **24**, 3549–3554 (2012).
140. Lei, S. *et al.* Evolution of the Electronic Band Structure and Efficient Photo-Detection in Atomic Layers of InSe. *ACS Nano* **8**, 1263–72 (2014).
141. Tamalampudi, S. R. *et al.* High performance and bendable few-layered InSe photodetectors with broad spectral response. *Nano Lett.* **14**, 2800–6 (2014).
142. Late, D. J. *et al.* GaS and GaSe ultrathin layer transistors. *Adv. Mater.* **24**, 3549–54 (2012).
143. Li, L. *et al.* Black phosphorus field-effect transistors. *Nat. Nanotechnol.* **9**, 372–377 (2014).
144. Koenig, S. P., Doganov, R. A., Schmidt, H., Castro Neto, A. H. & Özyilmaz, B. Electric field effect in ultrathin black phosphorus. *Appl. Phys. Lett.* **104**, 103106 (2014).
145. Buscema, M. *et al.* Fast and broadband photoresponse of few-layer black phosphorus field-effect transistors. *Nano Lett.* **14**, 3347–52 (2014).
146. Xia, F., Wang, H. & Jia, Y. Rediscovering black phosphorus as an anisotropic layered material for optoelectronics and

- electronics. *Nat. Commun.* **5**, 4458 (2014).
147. Wang, Q. H. et al. Electronics and optoelectronics of two-dimensional transition metal dichalcogenides. *Nat. Nanotechnol.* **7**, 699–712 (2012).
  148. Youngblood, N., Chen, C., Koester, S. J. & Li, M. Waveguide-integrated black phosphorus photodetector with high responsivity and low dark current. *Nat. Photonics* **9**, 247–252 (2015).
  149. Feng, W., Zheng, W., Cao, W. & Hu, P. Back Gated Multilayer InSe Transistors with Enhanced Carrier Mobilities via the Suppression of Carrier Scattering from a Dielectric Interface. *Adv. Mater.* **26**, 6587–93 (2014).
  150. Feng, W., Zhou, X., Tian, W., Zheng, W. & Hu, P. Performance improvement of multilayer InSe transistors with optimized metal contacts. *Phys. Chem. Chem. Phys.* **17**, (2015).
  151. Bao, W., Cai, X., Kim, D., Sridhara, K. & Fuhrer, M. S. High mobility ambipolar MoS<sub>2</sub> field-effect transistors: Substrate and dielectric effects. *Appl. Phys. Lett.* **102**, 042104 (2013).
  152. Gomez, L., berg, I. & Hoyt, J. L. Electron Transport in Strained-Silicon Directly on Insulator Ultrathin-Body n-MOSFETs With Body Thickness Ranging From 2 to 25 nm. *IEEE Electron Device Lett.* **28**, 285–287 (2007).
  153. Schwierz, F. Graphene transistors. *Nat. Nanotechnol.* **5**, 487–96 (2010).
  154. Sucharitakul, S. et al. Intrinsic Electron Mobility Exceeding 10<sup>3</sup> cm<sup>2</sup>/(V s) in Multilayer InSe FETs. *Nano Lett.* **15**, 3815–9 (2015).
  155. Wu, D. et al. Thickness-Dependent Dielectric Constant of Few-Layer In<sub>2</sub>Se<sub>3</sub> Nanoflakes. *Nano Lett.* **15**, 8136–40 (2015).
  156. Ma, Y., Dai, Y., Guo, M., Yu, L. & Huang, B. Tunable electronic and dielectric behavior of GaS and GaSe monolayers. *Phys. Chem. Chem. Phys.* **15**, 7098–105 (2013).

157. Madelung, O. *Semiconductor: Data Handbook*. (Springer, 2003).
158. Lei, S. *et al.* An Atomically Layered InSe Avalanche Photodetector. *Nano Lett.* **15**, 3048–3055 (2015).
159. Feng, W. *et al.* Ultrahigh photo-responsivity and detectivity in multilayer InSe nanosheets phototransistors with broadband response. *J. Mater. Chem. C* **3**, 7022–7028 (2015).
160. Tahersima, M. H. & Sorger, V. J. Strong Photon Absorption in 2-D Material-Based Spiral Photovoltaic Cells. *MRS Adv.* (2016). doi:10.1557/adv.2016.19
161. Velusamy, D. B. *et al.* Flexible transition metal dichalcogenide nanosheets for band-selective photodetection. *Nat. Commun.* **6**, 8063 (2015).
162. Dean, C. *et al.* Graphene based heterostructures. *Solid State Commun.* **152**, 1275–1282 (2012).
163. Ponomarenko, L. A. *et al.* Effect of a high- $\kappa$  environment on charge carrier mobility in graphene. *Phys. Rev. Lett.* **102**, 206603 (2009).
164. Morozov, S. V. *et al.* Giant Intrinsic Carrier Mobilities in Graphene and Its Bilayer. *Phys. Rev. Lett.* **100**, 016602 (2008).
165. Hong, X., Posadas, A., Zou, K., Ahn, C. H. & Zhu, J. High-mobility few-layer graphene field effect transistors fabricated on epitaxial ferroelectric gate oxides. *Phys. Rev. Lett.* **102**, 136808 (2009).
166. Dean, C. R. *et al.* Multicomponent fractional quantum Hall effect in graphene. *Nat. Phys.* **7**, 693–696 (2011).
167. Gorbachev, R. V. *et al.* Strong Coulomb drag and broken symmetry in double-layer graphene. *Nat. Phys.* **8**, 896–901 (2012).

168. Britnell, L. *et al.* Field-effect tunneling transistor based on vertical graphene heterostructures. *Science* **335**, 947–50 (2012).
169. Georgiou, T. *et al.* Vertical field-effect transistor based on graphene-WS<sub>2</sub> heterostructures for flexible and transparent electronics. *Nat. Nanotechnol.* **8**, 100–3 (2013).
170. Pozo-Zamudio, O. Del *et al.* Photoluminescence of two-dimensional GaTe and GaSe films. *2D Mater.* **2**, 035010 (2015).
171. Del Pozo-Zamudio, O. *et al.* Photoluminescence and Raman investigation of stability of InSe and GaSe thin films. (2015). at <<http://arxiv.org/abs/1506.05619>>
172. Lee, C.-H. *et al.* Atomically thin p–n junctions with van der Waals heterointerfaces. *Nat. Nanotechnol.* **9**, 676–681 (2014).
173. Furchi, M. M., Pospischil, A., Libisch, F., Burgdörfer, J. & Mueller, T. Photovoltaic effect in an electrically tunable van der Waals heterojunction. *Nano Lett.* **14**, 4785–91 (2014).
174. Cao, Y. *et al.* Strong enhancement of photoresponsivity with shrinking the electrodes spacing in few layer GaSe photodetectors. *Sci. Rep.* **5**, 8130 (2015).
175. Yuan, X. *et al.* Wafer-scale arrayed p-n junctions based on few-layer epitaxial GaTe. *Nano Res.* **8**, 3332–3341 (2015).
176. Wang, Y., Ding, K., Sun, B., Lee, S. & Jie, J. Two-dimensional layered material/silicon heterojunctions for energy and optoelectronic applications. *Nano Res.* **9**, 72–93 (2016).
177. Sundaram, R. S. *et al.* Electroluminescence in single layer MoS<sub>2</sub>. *Nano Lett.* **13**, 1416–21 (2013).
178. Pospischil, A., Furchi, M. M. & Mueller, T. Solar-energy conversion and light emission in an atomic monolayer p-n diode. *Nat. Nanotechnol.* **9**, 257–61 (2014).

179. Baugher, B. W. H., Churchill, H. O. H., Yang, Y. & Jarillo-Herrero, P. Optoelectronic devices based on electrically tunable p-n diodes in a monolayer dichalcogenide. *Nat. Nanotechnol.* **9**, 262–267 (2014).
180. Brotons-Gisbert, M., Sánchez-Royo, J. F. & Martínez-Pastor, J. P. Thickness identification of atomically thin InSe nanoflakes on SiO<sub>2</sub>/Si substrates by optical contrast analysis. *Appl. Surf. Sci.* **354**, 453–458 (2015).
181. Blake, P. *et al.* Making graphene visible. *Appl. Phys. Lett.* **91**, 063124 (2007).
182. Castellanos-Gomez, A. *et al.* Deterministic transfer of two-dimensional materials by all-dry viscoelastic stamping. *2D Mater.* **1**, 011002 (2014).
183. Smith, A. M. Polarization and magneto-optic properties of single-mode optical fiber. *Appl. Opt.* **17**, 52–6 (1978).
184. Kaminow, I. Polarization in optical fibers. *IEEE J. Quantum Electron.* **17**, 15–22 (1981).
185. Millot, M., Broto, J.-M., George, S., González, J. & Segura, A. Electronic structure of indium selenide probed by magnetoabsorption spectroscopy under high pressure. *Phys. Rev. B* **81**, 205211 (2010).
186. Goni, A., Cantarero, A., Schwarz, U., Syassen, K. & Chevy, A. Low-temperature exciton absorption in InSe under pressure. *Phys. Rev. B* **45**, 4221–4226 (1992).
187. Kress-Rogers, E., Nicholas, R. J., Portal, J. C. & Chevy, A. Cyclotron resonance studies on bulk and two-dimensional conduction electrons in InSe. *Solid State Commun.* **44**, 379–383 (1982).
188. Manjón, F. J. *et al.* Band structure of indium selenide investigated by intrinsic photoluminescence under high pressure.

- Phys. Rev. B* **70**, 125201 (2004).
189. Manjón, F. *et al.* Experimental and theoretical study of band structure of InSe and  $\text{In}_{1-x}\text{Ga}_x\text{Se}$  ( $x < 0.2$ ) under high pressure: Direct to indirect crossovers. *Phys. Rev. B* **63**, 125330 (2001).
  190. Dmitriev, A. I., Lashkarev, G. V., Kiselyev, V. K., Kononenko, V. K. & Kuleshov, E. M. The control of gap width in the low-dimensional systems with charge density waves instability. *Int. J. Infrared Millimeter Waves* **16**, 775–782 (1995).
  191. Gorshunov, B. *et al.* 'Intrinsic' transport properties of InSe studied by millimeter and submillimeter spectroscopy. *Solid State Commun.* **105**, 433–438 (1998).
  192. Tonndorf, P. *et al.* Photoluminescence emission and Raman response of monolayer  $\text{MoS}_2$ ,  $\text{MoSe}_2$ , and  $\text{WSe}_2$ . *Opt. Express* **21**, 4908–16 (2013).
  193. Millot, M. *et al.* High pressure and high magnetic field behaviour of free and donor-bound-exciton photoluminescence in InSe. *Phys. status solidi* **246**, 532–535 (2009).
  194. Manjón, F. *et al.* Band structure of indium selenide investigated by intrinsic photoluminescence under high pressure. *Phys. Rev. B* **70**, 125201 (2004).
  195. Singh, J., Bajaj, K. K. & Chaudhuri, S. Theory of photoluminescence line shape due to interfacial quality in quantum well structures. *Appl. Phys. Lett.* **44**, 805 (1984).
  196. Patané, A. *et al.* Linewidth analysis of the photoluminescence of  $\text{In}_x\text{Ga}_{1-x}\text{As}/\text{GaAs}$  quantum wells ( $x=0.09, 0.18, 1.0$ ). *Phys. Rev. B* **52**, 2784–2788 (1995).
  197. Shuming Yang and David F. Kelley. The Spectroscopy of InSe Nanoparticles. *J. Phys. Chem. B* **109**, 12701–12709 (2005).
  198. Shuming Yang and David F. Kelley. Transient Absorption Spectra and Dynamics of InSe Nanoparticles. *J. Phys. Chem. B*

- 110**, 13430–13435 (2006).
199. Camara, M., Mauger, A. & Devos, I. Electronic structure of the layer compounds GaSe and InSe in a tight-binding approach. *Phys. Rev. B* **65**, 125206 (2002).
  200. Zólyomi, V., Drummond, N. D. & Fal'ko, V. I. Electrons and phonons in single layers of hexagonal indium chalcogenides from ab initio calculations. *Phys. Rev. B* **89**, 205416 (2014).
  201. Sánchez-Royo, J. F. *et al.* Electronic structure, optical properties, and lattice dynamics in atomically thin indium selenide flakes. *Nano Res.* **7**, 1556–1568 (2014).
  202. Wickramaratne, D., Zahid, F. & Lake, R. K. Electronic and thermoelectric properties of van der Waals materials with ring-shaped valence bands. *J. Appl. Phys.* **118**, 075101 (2015).
  203. Zhuang, H. L. & Hennig, R. G. Single-Layer Group-III Monochalcogenide Photocatalysts for Water Splitting. *Chem. Mater.* **25**, 3232–3238 (2013).
  204. Cao, T., Li, Z. & Louie, S. G. Tunable Magnetism and Half-Metallicity in Hole-Doped Monolayer GaSe. *Phys. Rev. Lett.* **114**, 236602 (2015).
  205. Zahid, F. & Lake, R. Thermoelectric properties of Bi<sub>2</sub>Te<sub>3</sub> atomic quintuple thin films. *Appl. Phys. Lett.* **97**, 212102 (2010).
  206. Saeed, Y., Singh, N. & Schwingenschlögl, U. Thickness and strain effects on the thermoelectric transport in nanostructured Bi<sub>2</sub>Se<sub>3</sub>. *Appl. Phys. Lett.* **104**, 033105 (2014).
  207. Stauber, T., Peres, N. M. R., Guinea, F. & Castro Neto, A. H. Fermi liquid theory of a Fermi ring. *Phys. Rev. B* **75**, 115425 (2007).
  208. Varlet, A. *et al.* Anomalous sequence of quantum Hall liquids revealing a tunable Lifshitz transition in bilayer graphene. *Phys. Rev. Lett.* **113**, 116602 (2014).

209. Min, H., Sahu, B., Banerjee, S. K. & MacDonald, A. H. Ab initio theory of gate induced gaps in graphene bilayers. *Phys. Rev. B* **75**, 155115 (2007).
210. Wickramaratne, D., Zahid, F. & Lake, R. K. Electronic and thermoelectric properties of van der Waals materials with ring-shaped valence bands. *J. Appl. Phys.* **118**, 075101 (2015).
211. Kovalyuk, Z. D. *et al.* X-Ray Diffractometry and Raman Spectroscopy Investigation of Irradiated Layered III–VI Crystals. *J. Mater. Sci. Eng. A* **2**, 537–543 (2012).
212. Schwarcz, R., Kanehisa, M. A., Jouanne, M., Morhange, J. F. & Eddrief, M. Evolution of Raman spectra as a function of layer thickness in ultra-thin InSe films. *J. Phys. Condens. Matter* **14**, 967–973 (2002).
213. Gacem, K., Boukhicha, M., Chen, Z. & Shukla, A. High quality 2D crystals made by anodic bonding: a general technique for layered materials. *Nanotechnology* **23**, 505709 (2012).
214. Chen, Z., Gacem, K., Boukhicha, M., Biscaras, J. & Shukla, A. Anodic bonded 2D semiconductors: from synthesis to device fabrication. *Nanotechnology* **24**, 415708 (2013).
215. Patanè, A. & Balkan, N. in *Semicond. Res. Exp. Tech.* 125–170 (Springer, 2012).
216. Keffer, C., Hayes, T. M. & Bienenstock, A. Debye-Waller Factors and the PbTe Band-Gap Temperature Dependence. *Phys. Rev. B* **2**, 1966–1976 (1970).
217. Fan, H. Y. Temperature Dependence of the Energy Gap in Semiconductors. *Phys. Rev.* **82**, 900–905 (1951).
218. Guenzer, C. S. & Bienenstock, A. Temperature Dependence of the HgTe Band Gap. *Phys. Rev. B* **8**, 4655–4667 (1973).

219. Feng, W., Zheng, W., Chen, X., Liu, G. & Hu, P. Gate Modulation of Threshold Voltage Instability in Multilayer InSe Field Effect Transistors. *ACS Appl. Mater. Interfaces* **7**, 26691–5 (2015).
220. Varshni, Y. P. Temperature dependence of the energy gap in semiconductors. *Physica* **34**, 149–154 (1967).
221. Abay, B., Güder, H. S., Efeoglu, H. & Yogurtçu, Y. K. Excitonic absorption and Urbach-Martienssen's tails in Er-doped and undoped n-type InSe. *J. Phys. D. Appl. Phys.* **32**, 2942–2948 (1999).
222. Segura, A., Wunstel, K. & Chevy, A. Investigation of impurity levels in n-type indium selenide by means of Hall effect and deep level transient spectroscopy. *Appl. Phys. A Solids Surfaces* **31**, 139–145 (1983).
223. Kress-Rogers, E. *et al.* The electric sub-band structure of electron accumulation layers in InSe from Shubnikov-de Haas oscillations and inter-sub-band resonance. *J. Phys. C Solid State Phys.* **16**, 4285–4295 (1983).
224. Martinez-Pastor, J., Segura, A., Julien, C. & Chevy, A. Shallow-donor impurities in indium selenide investigated by means of far-infrared spectroscopy. *Phys. Rev. B* **46**, 4607–4616 (1992).
225. Homs, A. A. & Marí, B. Photoluminescence of undoped and neutron-transmutation-doped InSe. *J. Appl. Phys.* **88**, 4654 (2000).
226. Ferrer-Roca, C., Segura, A., Andrés, M. V., Pellicer, J. & Muñoz, V. Investigation of nitrogen-related acceptor centers in indium selenide by means of photoluminescence: Determination of the hole effective mass. *Phys. Rev. B* **55**, 6981–6987 (1997).
227. Bastard, G. *Wave mechanics applied to semiconductor heterostructures*. (Les Editions de Physique, 1988).
228. Bastard, G. Hydrogenic impurity states in a quantum well: A simple model. *Phys. Rev. B* **24**, 4714–4722 (1981).

229. Segura, A., Martínez-Tomas, M. C., Marí, B., Casanovas, A. & Chevy, A. Acceptor levels in indium selenide. An investigation by means of the Hall effect, deep-level-transient spectroscopy and photoluminescence. *Appl. Phys. A Solids Surfaces* **44**, 249–260 (1987).
230. Ferrer-Roca, C., Segura, A., Andrés, M. V., Pellicer, J. & Muñoz, V. Investigation of nitrogen-related acceptor centers in indium selenide by means of photoluminescence: Determination of the hole effective mass. *Phys. Rev. B* **55**, 6981–6987 (1997).
231. Zolyomi, V., Drummond, N. D. & Fal'ko, V. I. Electrons and phonons in single layers of hexagonal indium chalcogenides from ab initio calculations. *Phys. Rev. B* **89**, 9 (2014).
232. Millot, M., Broto, J.-M., George, S., González, J. & Segura, A. Electronic structure of indium selenide probed by magnetoabsorption spectroscopy under high pressure. *Phys. Rev. B* **81**, 205211 (2010).
233. Koperski, M. *et al.* Single photon emitters in exfoliated WSe<sub>2</sub> structures. *Nat. Nanotechnol.* **10**, 503–506 (2015).
234. Chakraborty, C., Kinnischtzke, L., Goodfellow, K. M., Beams, R. & Vamivakas, A. N. Voltage-controlled quantum light from an atomically thin semiconductor. *Nat. Nanotechnol.* **10**, 507–11 (2015).
235. Srivastava, A. *et al.* Optically active quantum dots in monolayer WSe<sub>2</sub>. *Nat. Nanotechnol.* **10**, 491–496 (2015).
236. He, Y.-M. *et al.* Single quantum emitters in monolayer semiconductors. *Nat. Nanotechnol.* **10**, 497–502 (2015).
237. Lonzarich, G. G. & Holtham, P. M. Anomalous Effect of Magnetic Breakdown on the Oscillatory Magnetization. *Proc. R. Soc. A Math. Phys. Eng. Sci.* **400**, 145–161 (1985).
238. Do, D. T., Mahanti, S. D. & Lai, C. W. Spin splitting in 2D monochalcogenide semiconductors. *Sci. Rep.* **5**, 17044 (2015).

239. Mueller, T., Xia, F. & Avouris, P. Graphene photodetectors for high-speed optical communications. *Nat. Photonics* **4**, 297–301 (2010).
240. Xia, F., Mueller, T., Lin, Y.-M., Valdes-Garcia, A. & Avouris, P. Ultrafast graphene photodetector. *Nat. Nanotechnol.* **4**, 839–43 (2009).
241. Zhang, B. Y. *et al.* Broadband high photoresponse from pure monolayer graphene photodetector. *Nat. Commun.* **4**, 1811 (2013).
242. Castellanos-Gomez, A. Black Phosphorus: Narrow Gap, Wide Applications. *J. Phys. Chem. Lett.* **6**, 4280–91 (2015).
243. Jin, W. *et al.* Direct measurement of the thickness-dependent electronic band structure of MoS<sub>2</sub> using angle-resolved photoemission spectroscopy. *Phys. Rev. Lett.* **111**, 106801 (2013).
244. Ruppert, C., Aslan, O. B. & Heinz, T. F. Optical properties and band gap of single- and few-layer MoTe<sub>2</sub> crystals. *Nano Lett.* **14**, 6231–6236 (2014).
245. He, K., Poole, C., Mak, K. F. & Shan, J. Experimental demonstration of continuous electronic structure tuning via strain in atomically thin MoS<sub>2</sub>. *Nano Lett.* **13**, 2931–6 (2013).
246. Castellanos-Gomez, A. *et al.* Local strain engineering in atomically thin MoS<sub>2</sub>. *Nano Lett.* **13**, 5361–6 (2013).
247. Allain, A., Kang, J., Banerjee, K. & Kis, A. Electrical contacts to two-dimensional semiconductors. *Nat. Mater.* **14**, 1195–205 (2015).
248. Sze, S. M. & Ng, K. K. *Physics of Semiconductor Devices*. (John Wiley & Sons, Inc., 2006).
249. Kang, J., Liu, W., Sarkar, D., Jena, D. & Banerjee, K. Computational Study of Metal Contacts to Monolayer Transition-

- Metal Dichalcogenide Semiconductors. *Phys. Rev. X* **4**, 031005 (2014).
250. Her, M., Beams, R. & Novotny, L. Graphene transfer with reduced residue. *Phys. Lett. A* **377**, 1455–1458 (2013).
251. Liang, X. *et al.* Toward clean and crackless transfer of graphene. *ACS Nano* **5**, 9144–53 (2011).
252. Bae, S. *et al.* Roll-to-roll production of 30-inch graphene films for transparent electrodes. *Nat. Nanotechnol.* **5**, 574–8 (2010).
253. Wilson, N. R. *et al.* Weak mismatch epitaxy and structural Feedback in graphene growth on copper foil. *Nano Res.* **6**, 99–112 (2013).
254. Hughes, H. P. & Starnberg, H. I. *Electron Spectroscopies Applied to Low-Dimensional Materials.* **24**, (Springer Netherlands, 2002).
255. Kittel, C. *Introduction to Solid State Physics.* (John Wiley & Sons, 2005).
256. Massicotte, M. *et al.* Picosecond photoresponse in van der Waals heterostructures. *Nat. Nanotechnol.* (2015).  
doi:10.1038/nnano.2015.227
257. Luo, W. *et al.* Gate Tuning of High-Performance InSe-Based Photodetectors Using Graphene Electrodes. *Adv. Opt. Mater.* **3**, 1418–1423 (2015).
258. Zhang, W. *et al.* Ultrahigh-gain photodetectors based on atomically thin graphene-MoS<sub>2</sub> heterostructures. *Sci. Rep.* **4**, 3826 (2014).
259. Lee, G.-H. *et al.* Flexible and transparent MoS<sub>2</sub> field-effect transistors on hexagonal boron nitride-graphene heterostructures. *ACS Nano* **7**, 7931–6 (2013).
260. Zhang, W. *et al.* High-gain phototransistors based on a CVD

- MoS<sub>2</sub> monolayer. *Adv. Mater.* **25**, 3456–61 (2013).
261. Island, J. O. *et al.* Ultrahigh Photoresponse of Few-Layer TiS<sub>3</sub> Nanoribbon Transistors. *Adv. Opt. Mater.* **2**, 641–645 (2014).
262. Island, J., Blanter, S. I., Buscema, M., van der Zant, H. S. J. & Castellanos-Gomez, A. Gate Controlled Photocurrent Generation Mechanisms in High-Gain In<sub>2</sub>Se<sub>3</sub> Phototransistors. *Nano Lett.* **15**, 7853 (2015).
263. Eda, G. & Maier, S. A. Two-dimensional crystals: managing light for optoelectronics. *ACS Nano* **7**, 5660–5 (2013).
264. Schall, D. *et al.* 50 GBit/s Photodetectors Based on Wafer-Scale Graphene for Integrated Silicon Photonic Communication Systems. *ACS Photonics* **1**, 781–784 (2014).
265. Furchi, M. M., Polyushkin, D. K., Pospischil, A. & Mueller, T. Mechanisms of Photoconductivity in Atomically Thin MoS<sub>2</sub>. *Nano Lett.* **14**, 6165–70 (2014).
266. Dufferwiel, S. *et al.* Strong exciton-photon coupling in open semiconductor microcavities. *Appl. Phys. Lett.* **104**, 192107 (2014).
267. Konstantatos, G. *et al.* Hybrid graphene-quantum dot phototransistors with ultrahigh gain. *Nat. Nanotechnol.* **7**, 363–8 (2012).
268. Do, D. T., Mahanti, S. D. & Lai, C. W. Spin splitting in 2D monochalcogenide semiconductors. *Sci. Rep.* **5**, (2015).
269. Lei, S. *et al.* Optoelectronic memory using two-dimensional materials. *Nano Lett.* **15**, 259–65 (2015).
270. Feng, W. *et al.* Solid-State Reaction Synthesis of a InSe/CuInSe<sub>2</sub> Lateral p–n Heterojunction and Application in High Performance Optoelectronic Devices. *Chem. Mater.* **27**, 983–989 (2015).

271. Léonard, F. & Talin, A. A. Electrical contacts to one- and two-dimensional nanomaterials. *Nat. Nanotechnol.* **6**, 773–83 (2011).
272. Xia, F., Perebeinos, V., Lin, Y., Wu, Y. & Avouris, P. The origins and limits of metal-graphene junction resistance. *Nat. Nanotechnol.* **6**, 179–84 (2011).
273. Liu, S. *et al.* Controllable Growth of Vertical Heterostructure GaTe<sub>x</sub>Se<sub>1-x</sub>/Si by Molecular Beam Epitaxy. *ACS Nano* **9**, 8592–8 (2015).
274. Tran, T. T., Bray, K., Ford, M. J., Toth, M. & Aharonovich, I. Quantum emission from hexagonal boron nitride monolayers. *Nat. Nanotechnol.* **11**, 37–41 (2015).
275. Feng, J., Qian, X., Huang, C.-W. & Li, J. Strain-engineered artificial atom as a broad-spectrum solar energy funnel. *Nat. Photonics* **6**, 866–872 (2012).
276. Lee, C., Wei, X., Kysar, J. W. & Hone, J. Measurement of the elastic properties and intrinsic strength of monolayer graphene. *Science* **321**, 385–8 (2008).
277. Yun, W. S., Han, S. W., Hong, S. C., Kim, I. G. & Lee, J. D. Thickness and strain effects on electronic structures of transition metal dichalcogenides: 2H- M X 2 semiconductors ( M = Mo, W; X = S, Se, Te). *Phys. Rev. B* **85**, 033305 (2012).
278. Zeng, H., Dai, J., Yao, W., Xiao, D. & Cui, X. Valley polarization in MoS<sub>2</sub> monolayers by optical pumping. *Nat. Nanotechnol.* **7**, 490–3 (2012).
279. Xiao, D., Liu, G.-B., Feng, W., Xu, X. & Yao, W. Coupled Spin and Valley Physics in Monolayers of MoS<sub>2</sub> and Other Group-VI Dichalcogenides. *Phys. Rev. Lett.* **108**, 196802 (2012).
280. Jariwala, D., Sangwan, V. K., Lauhon, L. J., Marks, T. J. & Hersam, M. C. Emerging device applications for semiconducting two-dimensional transition metal dichalcogenides. *ACS Nano* **8**, 1102–20 (2014).

281. Li, W. & Li, J. Piezoelectricity in Two-Dimensional Group III Monochalcogenides. *Nano Res.* **8**, 3796 (2015).
282. Qian, X., Wang, Y., Li, W., Lu, J. & Li, J. Modelling of stacked 2D materials and devices. *2D Mater.* **2**, 032003 (2015).
283. Yang, S. *et al.* Self-Driven Photodetector and Ambipolar Transistor in Atomically Thin GaTe-MoS<sub>2</sub> p-n vdW Heterostructure. *ACS Appl. Mater. Interfaces* **8**, 2533–9 (2016).
284. Tongay, S. *et al.* Tuning interlayer coupling in large-area heterostructures with CVD-grown MoS<sub>2</sub> and WS<sub>2</sub> monolayers. *Nano Lett.* **14**, 3185–90 (2014).
285. Gong, Y. *et al.* Vertical and in-plane heterostructures from WS<sub>2</sub>/MoS<sub>2</sub> monolayers. *Nat. Mater.* **13**, 1135–42 (2014).
286. Vishwanath, S. *et al.* Controllable growth of layered selenide and telluride heterostructures and superlattices using molecular beam epitaxy. *J. Mater. Res.* (2016). doi:10.1557/jmr.2015.374
287. Woods, C. R. *et al.* Commensurate–incommensurate transition in graphene on hexagonal boron nitride. *Nat. Phys.* **10**, 451–456 (2014).
288. Taychatanapat, T., Watanabe, K., Taniguchi, T. & Jarillo-Herrero, P. Electrically tunable transverse magnetic focusing in graphene. *Nat. Phys.* **9**, 225–229 (2013).
289. Hofstadter, D. R. Energy levels and wave functions of Bloch electrons in rational and irrational magnetic fields. *Phys. Rev. B* **14**, 2239–2249 (1976).
290. Kośmider, K. & Fernández-Rossier, J. Electronic properties of the MoS<sub>2</sub>-WS<sub>2</sub> heterojunction. *Phys. Rev. B* **87**, 075451 (2013).
291. Wei, W. *et al.* Electronic Properties of Two-Dimensional Van der Waals GaS/GaSe Heterostructures. *J. Mater. Chem. C* (2015). doi:10.1039/C5TC02975A

292. Huang, L., Chen, Z. & Li, J. Effects of strain on the band gap and effective mass in two-dimensional monolayer GaX (X = S, Se, Te). *RSC Adv.* **5**, 5788–5794 (2015).
293. Yu, G. L. *et al.* Hierarchy of Hofstadter states and replica quantum Hall ferromagnetism in graphene superlattices. *Nat. Phys.* **10**, 525–529 (2014).
294. Zhou, S., Tao, X. & Gu, Y. Thickness-Dependent Thermal Conductivity of Suspended Two-Dimensional Single-Crystal In<sub>2</sub>Se<sub>3</sub> Layers Grown by Chemical Vapor Deposition. *J. Phys. Chem. C* **120**, 4753–4758 (2016).
295. Hou, X., Chen, S., Du, Z., Liu, X. & Cui, J. Improvement of the thermoelectric performance of InSe-based alloys doped with Sn. *RSC Adv.* **5**, 102856–102862 (2015).
296. Beardsley, R. *et al.* Nanomechanical probing of the layer/substrate interface of an exfoliated InSe sheet on sapphire. *Sci. Rep.* (2016).
297. Balendhran, S., Walia, S., Nili, H., Sriram, S. & Bhaskaran, M. Elemental analogues of graphene: silicene, germanene, stanene, and phosphorene. *Small* **11**, 640–52 (2015).
298. Mannix, A. J. *et al.* Synthesis of borophenes: Anisotropic, two-dimensional boron polymorphs. *Science (80-. )*. **350**, 1513–1516 (2015).
299. Lalmi, B. *et al.* Epitaxial growth of a silicene sheet. *Appl. Phys. Lett.* **97**, 223109 (2010).
300. Vogt, P. *et al.* Silicene: Compelling Experimental Evidence for Graphenelike Two-Dimensional Silicon. *Phys. Rev. Lett.* **108**, 155501 (2012).
301. Liu, Z.-L. *et al.* Various atomic structures of monolayer silicene fabricated on Ag(111). *New J. Phys.* **16**, 075006 (2014).
302. Dávila, M. E., Xian, L., Cahangirov, S., Rubio, A. & Le Lay, G.

- Germanene: a novel two-dimensional germanium allotrope akin to graphene and silicene. *New J. Phys.* **16**, 095002 (2014).
303. Zhu, F. *et al.* Epitaxial growth of two-dimensional stanene. *Nat. Mater.* **14**, 1020–1025 (2015).
304. Bianco, E. *et al.* Stability and exfoliation of germanane: a germanium graphane analogue. *ACS Nano* **7**, 4414–21 (2013).
305. Jiang, S. *et al.* Improving the stability and optical properties of germanane via one-step covalent methyl-termination. *Nat. Commun.* **5**, 3389 (2014).
306. Kamal, C. & Ezawa, M. Arsenene: Two-dimensional buckled and puckered honeycomb arsenic systems. *Phys. Rev. B* **91**, 085423 (2015).
307. Zhang, S., Yan, Z., Li, Y., Chen, Z. & Zeng, H. Atomically Thin Arsenene and Antimonene: Semimetal-Semiconductor and Indirect-Direct Band-Gap Transitions. *Angew. Chemie* **127**, 3155–3158 (2015).
308. Kamal, C., Chakrabarti, A. & Ezawa, M. Aluminene as highly hole-doped graphene. *New J. Phys.* **17**, 083014 (2015).
309. Wang, C., Xia, Q., Nie, Y., Rahman, M. & Guo, G. Strain engineering band gap, effective mass and anisotropic Dirac-like cone in monolayer arsenene. *AIP Adv.* **6**, 035204 (2016).
310. Liu, C.-C., Jiang, H. & Yao, Y. Low-energy effective Hamiltonian involving spin-orbit coupling in silicene and two-dimensional germanium and tin. *Phys. Rev. B* **84**, 195430 (2011).
311. Broek, B. van den *et al.* Two-dimensional hexagonal tin: ab initio geometry, stability, electronic structure and functionalization. *2D Mater.* **1**, 021004 (2014).
312. Cai, B. *et al.* Tinene: a two-dimensional Dirac material with a 72 meV band gap. *Phys. Chem. Chem. Phys.* **17**, 12634–8 (2015).

313. Liu, C.-C., Feng, W. & Yao, Y. Quantum Spin Hall Effect in Silicene and Two-Dimensional Germanium. *Phys. Rev. Lett.* **107**, 076802 (2011).
314. Kane, C. L. & Mele, E. J. Quantum Spin Hall Effect in Graphene. *Phys. Rev. Lett.* **95**, 226801 (2005).
315. Bernevig, B. A., Hughes, T. L. & Zhang, S.-C. Quantum spin Hall effect and topological phase transition in HgTe quantum wells. *Science* **314**, 1757–61 (2006).
316. König, M. *et al.* Quantum spin hall insulator state in HgTe quantum wells. *Science* **318**, 766–70 (2007).
317. Ding, Y. & Wang, Y. Quasi-Free-Standing Features of Stanene/Stanane on InSe and GaTe Nanosheets: A Computational Study. *J. Phys. Chem. C* **119**, 27848–27854 (2015).
318. Ni, Z., Minamitani, E., Ando, Y. & Watanabe, S. The electronic structure of quasi-free-standing germanene on monolayer MX (M = Ga, In; X = S, Se, Te). *Phys. Chem. Chem. Phys.* **17**, 19039–19044 (2015).
319. Xu, Y. *et al.* Large-gap quantum spin Hall insulators in tin films. *Phys. Rev. Lett.* **111**, 136804 (2013).
320. Tao, L. *et al.* Silicene field-effect transistors operating at room temperature. *Nat. Nanotechnol.* **10**, 227–231 (2015).
321. Ding, Y. & Wang, Y. Electronic structures of silicene/GaS heterosheets. *Appl. Phys. Lett.* **103**, 043114 (2013).
322. Scalise, E. *et al.* Engineering the electronic properties of silicene by tuning the composition of MoX<sub>2</sub> and GaX (X = S, Se, Te) chalcogenide templates. *2D Mater.* **1**, 011010 (2014).